Visible Light Communication System-on-Chip Design

by

Xianbo LI

A Thesis Submitted to

The Hong Kong University of Science and Technology
in Partial Fulfillment of the Requirements for
the Degree of Doctor of Philosophy
in the Department of Electronic and Computer Engineering

July 2017, Hong Kong

Authorization

I hereby declare that I am the sole author of the thesis.

I authorize the Hong Kong University of Science and Technology to lend this thesis to other institutions or individuals for the purpose of scholarly research.

I further authorize the Hong Kong University of Science and Technology to reproduce the thesis by photocopying or by other means, in total or in part, at the request of other institutions or individuals for the purpose of scholarly research.

LZ, Xianbo

Xianbo LI

July 2017

Visible Light Communication System-on-Chip Design

by

Xianbo LI

This is to certify that I have examined the above PhD thesis and have found that it is complete and satisfactory in all respects, and that any and all revisions required by

the thesis examination committee have been made.

Prof. C. Patrick YUE, ECE Department (Thesis Supervisor)

Prof. Bertram SHI (Head of ECE Department)

Thesis Examination Committee:

- 1. Prof. C. Patrick YUE (Supervisor), Department of Electronic and Computer Engineering
- 2. **Prof. Kei May LAU**, Department of Electronic and Computer Engineering
- 3. **Prof. Wing-Hung KI**, Department of Electronic and Computer Engineering
- 4. Prof. Baoling HUANG, Department of Mechanical and Aerospace Engineering
- Prof. Che LIN (External Examiner), Department of Electrical Engineering, National Tsing Hua University

Department of Electronic and Computer Engineering,
The Hong Kong University of Science and Technology
July 2017

To my family

Acknowledgements

First of all, I would like to express my sincere gratitude to my Ph.D. supervisor, Prof. C. Patrick YUE for his encouragement, patience, valuable support, and guidance throughout my research. It has been a wonderful experience to pursue my Ph.D degree in Prof. YUE's group. Not only have I learned how to conduct research and how to broaden my horizons, I also have learned how to prepare for a successful life.

In addition, I sincerely appreciate Prof. Kei May LAU, Prof. Wing-Hung KI, Prof. Che LIN, Prof. Baoling HUANG, and Prof. Nian LIN serving as my thesis committee members and proposing valuable suggestions and comments for my research.

I would like to thank Dr. Liang WU, Dr. Zhaojun LIU, Dr. Wing Cheung CHONG, Mr. Terence CHO and Mr. Junmin JIANG for the close collaboration and support in my research.

I would like to thank the ECE lab technicians, Mr. Siu Fai LUK, Mr. Raymond WONG, and Mr. Frederick KWOK for their efficient technical support in chip-on-board bonding, design tools, and chip tape-outs.

I would like to thank my colleagues in the High Speed Silicon Laboratory (HS2L), including Mr. Babar HUAASIN, Mr. Fengyu CHE, Mr. Li WANG, Mr. Liusheng SUN, Dr. Quan PAN, Dr. Yipeng WANG, Dr. Salahuddin Raju, Mr. Guang ZHU, Mr. Duona LUO, Dr. Haikun JIA, Dr. Zhao ZHANG, Dr. Xiangyu MENG, Mr. Khawaja Qasim MAQBOOL, Mr. Milad Kalantari MAHMOUDABADI, Mr. Zhengxiong HOU, Miss Liwen JING, all of whom shared numerous valuable discussions with me.

Finally, I would like to express my sincere appreciation to my families for their love and encouragement, which gave me strength and confidence. In particular, I would like to thank my parents, and my wife, Katherine Yuan HUANG, for their unlimited support and love all the way.

Table of Contents

| Authorization Page | ii |
|---|------|
| Signature Page | iii |
| Acknowledgements | v |
| Table of Contents | vi |
| List of Figures | viii |
| List of Tables | xii |
| ABSTRACT | xiii |
| CHAPTER 1 Introduction to VLC | 1 |
| 1.1 Research Background | 1 |
| 1.2 Advantages of VLC | 2 |
| 1.3 Implementation of VLC | 4 |
| 1.3.1 Typical System Architecture | 4 |
| 1.3.2 Modulation Schemes | 4 |
| 1.3.3 Network Topologies | 6 |
| 1.3.4 VLC Systems with Different Light Sources | 7 |
| 1.4 Application of VLC | 10 |
| 1.4.1 Smart Lighting | 11 |
| 1.4.2 Smart Display | 11 |
| 1.4.3 Sensing | 14 |
| 1.4.4 Indoor Positioning | 16 |
| 1.4.5 Vehicle Communication | 18 |
| 1.4.6 Underwater Communication | 19 |
| 1.5 Scope of Research | 20 |
| CHAPTER 2 LED Micro-display Technology | 21 |
| 2.1 Introduction | 21 |
| 2.2 Passive Matrix Driving Scheme of LED Micro-display | 22 |
| 2.3 Active Matrix Driving Scheme of LED Micro-display | 23 |
| 2.4 Fabrication Process of LED Micro-display | 24 |
| CHAPTER 3 VLC Transmitter Embedded in Active Matrix LED Micro-display | 25 |
| 3.1 Introduction | 25 |
| 3.2 Proposed Control Scheme | 26 |

| 3.3 | Proposed Pixel Driver Array | 28 |
|-------|---|----|
| 3.4 | Proposed System Architecture | 33 |
| 3.5 | μLED Array and Flip-Chip Bonding | 34 |
| 3.6 | Experimental Results | 35 |
| СНАРТ | ER 4 VLC Receiver | 43 |
| 4.1 | Design Considerations | 43 |
| 4.2 | Blue filtering | 45 |
| 4.3 | Typical Receiver Architecture | 47 |
| 4.4 | Post-Equalization Techniques | 47 |
| СНАРТ | ER 5 VLC Receiver with Ambient Light Rejection and Equalization | 50 |
| 5.1 | Proposed System Architecture | 50 |
| 5.2 | Typical TIA Architecture | 51 |
| 5.3 | Proposed TIA with Ambient Light Rejection | 53 |
| 5.4 | Equalizer | 61 |
| 5.6 | Other Blocks | 65 |
| 5.7 | Simulation and Experimental results | 71 |
| СНАРТ | ER 6 Conclusion, Future Work and Publication | 83 |
| 6.1 | Conclusion | 83 |
| 6.2 | Future Work | 84 |
| 6.3 | Published Works | 84 |
| 6.4 | Works Accepted, Submitted or Under Preparation | 85 |
| DEFED | ENCES | 06 |

List of Figures

| Fig. 1.1 Visible light spectrum ranging from 380 nm to 780 nm |
|--|
| Fig. 1.2 A typical VLC transceiver system |
| Fig. 1.3 Dimming implementation using (a) OOK, and (b) VPPM [20]5 |
| Fig. 1.4 Typical network topologies of VLC systems [1]7 |
| Fig. 1.5 Indoor illumination system integrated with VLC techniques to enable a smart house |
| [45]11 |
| Fig. 1.6 (a) An extra communication layer on top of the content layer, (b) the resulting |
| composite image after modifying the pixel translucency of the communication layer, and (c) |
| demonstration of the system, where the image on the transmitter was encoded with data, and |
| the receiver camera captured the picture to extract the transmitted data, which was displayed |
| on the camera screen [48, 50]. |
| Fig. 1.7 Potential architecture for smart display: (a) transmitter for a smart display, and (b) |
| receiver for a smart display |
| Fig. 1.8 Human sensing VLC system: (a) posture shadow of a manikin under a ceiling LED, |
| and (b) a test bed consisting of five LED lights and 324 PDs [52] |
| Fig. 1.9 Landing and take-off assistance network architecture [53] |
| Fig. 1.10 A typical VLC-based indoor positioning system [56] |
| Fig. 1.11 A mobile robot used to easily collect the fingerprint distribution information of LED |
| beacons [57] |
| Fig. 1.12 Vehicle-to-vehicle VLC (V2V-VLC) using LED headlights or LED brake lights and |
| vehicle-to-infrastructure VLC (V2I-VLC) using LED traffic lights [59]19 |
| Fig. 1.13 Operation of an untethered remotely operated vehicle (UTROV) with hybrid |
| VLC/acoustic communications: (a) with low-speed acoustic communication, (b) with high- |
| speed VLC through a small ship-based relay, and (c) with high-speed VLC through fixed |
| infrastructure on the seafloor [65] |
| Fig. 2.1 Google Glass explorer edition [71]. |
| Fig. 2.2 Passive matrix driving scheme of an LED micro-display [73] |
| Fig. 2.3 Active matrix driving scheme of an LED micro-display [73]23 |
| Fig. 3.1 (a) 4-bit binary-weighted PWM frame structure and predefined VLC data packet, and |
| (b) illustration of grayscale control |
| Fig. 3.2 (a) Basic 2T1C nivel driver cell for display only (b) the 3T1C nivel driver cell with a |

| novel VLC function, (c) operation timing of the 3T1C pixel driver cell, and (d) the 3T1C pixel |
|---|
| driver cell connected to an input buffer for C _{DATA} |
| Fig. 3.3 Schematic of the AMLED driver and the timing diagram to achieve specific grayscales |
| on four µLED pixels using progressive scanning |
| Fig. 3.4 System architecture and implementation of the proposed AMLED micro-display driver |
| SoC33 |
| Fig. 3.5 (a) Structure of the 400×240 GaN μLED array, and (b) an SEM image of indium bumps |
| generated after the reflow process for flip-chip bonding |
| Fig. 3.6 Photographs of the CMOS AMLED driver SoC, the 400×240 GaN μLED array and |
| the entire micro-display module with a sample image |
| Fig. 3.7 (a) Measured I-V characteristics of 40 randomly selected µLED pixels with an inset |
| photo showing the direct probing of one µLED pixel for I-V measurements, and (b) optical |
| emission spectrum of the µLED pixels |
| Fig. 3.8 Measured optical frequency response of the micro-display module, including the |
| AMLED driver SoC and the µLED array |
| Fig. 3.9 Measured illuminated power and current consumption of the µLED array under 16 |
| different grayscale settings with all pixels active |
| Fig. 3.10 (a) Diagram of the VLC experimental setup for the micro-display module, (b) the |
| VLC link measurement setup without a lens, and (c) diagram of the illuminated power |
| measurement setup with a photo showing the employed photo-detector and power meter39 |
| Fig. 3.11 (a) Measured waveforms of the VLC enabling signal (EN _{PWM}), the VLC modulation |
| signal (D _{VLC}), and the received VLC signal from the RX front-end at 20-cm distance without |
| a lens, (b) eye diagram of the received VLC signal at 20-cm distance without a lens, and (c) |
| eye diagram of the received VLC signal at 500-cm distance with TX and RX lenses41 |
| Fig. 3.12 Measured received power and BER with an effective data rate of 1.25 Mb/s versus |
| distance for image#1 and image#2, respectively |
| Fig. 4.1 (a) Normalized frequency response of a commercial phosphorescent white LED [87], |
| which is measured using a commercial photoreceiver shown in the inset, and (b) received eye |
| diagrams from the white LED using the commercial photoreceiver with PRBS-11 inputs43 |
| Fig. 4.2 Normalized spectral response of the phosphorescent white LED (which is cool white) |

| from the LED data sheet. | 45 |
|---|---------|
| Fig. 4.3 Block diagram of a typical VLC receiver. | 47 |
| Fig. 4.4 VLC system with 1st order passive equalizer [89] | 48 |
| Fig. 4.5 Hybrid passive and active equalizers employed in a VLC receiver [94] | 48 |
| Fig. 5.1 Proposed VLC receiver with ambient light rejection and equalization | 50 |
| Fig. 5.2 General configuration of a TIA. | 51 |
| Fig. 5.3 Typical implementation of a two-stage TIA. | 53 |
| Fig. 5.4 A TIA structure introduced in [91]. | 53 |
| Fig. 5.5 Proposed inverter-based TIA with variable gain. | 54 |
| Fig. 5.6 The small-signal model of the core amplifier. | 54 |
| Fig. 5.7 The schematic of an inverter-based TIA | 57 |
| Fig. 5.8 A typical optical preamplifier with ambient light rejection [91]. | 59 |
| Fig. 5.9 Proposed solution for ambient light rejection with (a) single-ended TIA, a | nd (b) |
| differential TIA. | 60 |
| Fig. 5.10 Simulated TIA gain with different DC photocurrents generated by ambient | light, |
| where I_{DC} ranges from 10 μA to 90 μA | 61 |
| Fig. 5.11 CTLE with a 3-bit digitally tunable capacitor C_{EQ} . | 62 |
| Fig. 5.12 Configuration of a conventional single-ended Cherry-Hooper amplifier [101]. | 63 |
| Fig. 5.13 Schematic of the differential-to-single amplifier (D2S) based on the Cherry-Fig. 5.13 Schematic of the differential-to-single amplifier (D2S) based on the Cherry-Fig. 5.13 Schematic of the differential-to-single amplifier (D2S) based on the Cherry-Fig. 5.13 Schematic of the differential-to-single amplifier (D2S) based on the Cherry-Fig. 5.13 Schematic of the differential-to-single amplifier (D2S) based on the Cherry-Fig. 5.13 Schematic of the differential-to-single amplifier (D2S) based on the Cherry-Fig. 5.13 Schematic of the differential-to-single amplifier (D2S) based on the Cherry-Fig. 5.13 Schematic of the differential-to-single amplifier (D2S) based on the Cherry-Fig. 5.13 Schematic of the differential-to-single amplifier (D2S) based on the Cherry-Fig. 5.13 Schematic of the differential-to-single amplifier (D2S) based on the Cherry-Fig. 5.13 Schematic of the differential-to-single amplifier (D2S) based on the Cherry-Fig. 5.13 Schematic of the differential-to-single amplifier (D2S) based on the data data data data data data data dat | Iooper |
| amplifier structure. | 64 |
| Fig. 5.14 Schematic of the error amplifier (EA). | 66 |
| Fig. 5.15 Schematic of the single-to-differential amplifier (S2D) | 67 |
| Fig. 5.16 Illustration of a current cancellation technique: (a) cross-coupling pair, (b) | diode- |
| connected pair, and (c) combination of the cross-coupling pair and the diode-connecte | d pair. |
| | 68 |
| Fig. 5.17 Schematic of the DC offset cancellation (DOC) amplifier (a) using two capa | citors, |
| and (b) using only one capacitor. | 69 |
| Fig. 5.18 Schematic of the LDO. | 70 |
| Fig. 5.19 Microphotograph of the proposed receiver SoC | 71 |
| Fig. 5.20 An IEEE 802.15.7 PHY-II VLC system that consists of the proposed received | r SoC |
| and a custom transmitter SoC [20] without employing a blue filter: (a) block diagram | of the |
| system, (b) photograph of the system, and (c) component specification | 73 |
| Fig. 5.21 (a) Simulated trans-impedance gain of the proposed receiver SoC when the C | ΓLE is |

| turned off, and the received eye diagrams using a high-speed laser diode as the transmitter |
|--|
| front-end to replace the low-speed phosphorescent white LEDs, and (b) simulated trans- |
| impedance gain of the proposed receiver SoC when the CTLE is turned on74 |
| Fig. 5.22 Simulated input referred noise current density of the proposed TIA and receiver SoC. |
| 75 |
| Fig. 5.23 Measured received transient waveforms using the proposed receiver SoC and the |
| commercial photoreceiver (New Focus 1801-FC). The VLC data rate is 10 Mb/s with OOK |
| PRBS-11 optical inputs emitted by the phosphorescent white LEDs76 |
| Fig. 5.24 Received eye diagrams under different conditions when using phosphorescent white |
| LEDs as the transmitter front-end, where (A) and (B) are captured under different ambient light, |
| while (C), (D), (E) and (F) are captured under different modulation schemes with different |
| CTLE status. The measurements are performed at a distance of 0.25 m using optical PRBS-11 |
| inputs without any lens |
| Fig. 5.25 Measured bit error rate and corresponding illumination level at different |
| communication distances for a fixed VLC data rate of 20 Mb/s when employing OOK |
| modulation and optical PRBS-11 inputs without any lens |
| Fig. 5.26 Measured bit error rate versus VLC data rates at a distance of 0.25 m without any |
| lens, and at a distance of 1.6 m with an RX lens. The measurements are performed using optical |
| PRBS-11 inputs and OOK modulation |

List of Tables

| Table 1.1 Comparison of VLC systems using different light sources | 10 |
|---|----|
| Table 3.1 PERFORMANCE SUMMARY AND COMPARISON | 42 |
| Table 4.1 RECOMMENDED ILLUMINATION LEVELS FOR VARIOUS VENUES [92] | 45 |
| Table 5.1 Performance Summary and Comparison | 80 |

ABSTRACT

Visible light communication (VLC) has attracted a great deal of research interest for light fidelity (LiFi) applications to ease the ever-increasing radio spectrum congestion problem faced by the mobile communication industry. Furthermore, emerging Internet of Things (IoT) applications utilizing LED lights, signage, and displays as distributed digital content broadcasters have driven the integration level of VLC systems to lower manufacturing cost and higher energy efficiency. In this thesis, two System-on-Chip (SoC) have been proposed and implemented, including a transmitter SoC and a receiver SoC.

- (1) The proposed transmitter SoC is the first active matrix light-emitting diode (AMLED) micro-display driver with an embedded VLC transmitter. The driver integrates four identical macro-cells, each containing a pixel driver array, a row driver, a column driver and a first-in first-out (FIFO) memory, to drive a wide quarter-VGA (WQVGA) display featuring 400×240 blue micro-LED (μLED) pixels fabricated on a single gallium nitride (GaN) substrate. The size of each μLED pixel is 30×30 μm². At the system level, pulse-width modulation (PWM) superimposed with on-off keying (OOK) modulation is proposed to accomplish grayscale control for display and simultaneously transmit VLC signals by modulating the μLED array. At the circuit level, a pixel driver cell consisting of three transistors and one capacitor (3T1C) with a novel VLC function is employed to implement the control scheme. Flip-chip bonding is adopted to establish connections between the WQVGA micro-display and the AMLED driver SoC. Implemented in a 0.5-μm CMOS process, the transmitter SoC enables a high-resolution micro-display module to achieve 4-bit grayscale at a 100-Hz frame rate, while supporting 1.25-Mb/s VLC for a bit error rate (BER) <10-5 up to 25 cm distance without a lens. When using optical lenses, the VLC distance is extended to >500 cm.
- (2) The proposed receiver SoC is an energy-efficient VLC receiver that employs ambient light rejection and post-equalization techniques for emerging LiFi applications based on ordinary phosphorescent white LEDs. The SoC integrates a variable-gain trans-impedance amplifier (TIA), an ambient light rejection (ALR) unit, a two-stage continuous time linear equalizer (CTLE) and a DC offset cancellation (DOC) amplifier. On-chip LDOs are utilized to suppress supply noise effects on the sensitive input stages. Implemented in a standard commercial 0.18-µm CMOS process, the SoC can deliver a bit efficiency of 92 pJ/bit at a peak data rate of 24

Mb/s, which is over 6 times better than prior art. A complete IEEE 802.15.7 PHY-II standard-complaint LiFi link is demonstrated using the proposed receiver SoC and a custom transmitter SoC over 1.6 m distance with a BER of 1×10^{-9} .

CHAPTER 1 Introduction to VLC

1.1 Research Background

The electromagnetic spectrum is a limited and valuable natural resource. Fig. 1.1 depicts the available electromagnetic spectrum covering radio waves through to gamma rays. With the ever-increasing demand in data traffic due to various multimedia consumer applications, the popular radio spectrum occupying the lowest 300 GHz frequency bandwidth is getting crowded. As a supplementary solution for radio frequency (RF) wireless technologies, optical communication utilizing the unregulated optical spectrum beyond 300 GHz has become the key solution for more extensive and high-speed data transmission in the future. In addition, as an energy-efficient and reliable illumination technology, LEDs are being deployed ubiquitously to replace incandescent and fluorescent lights for energy saving and environmental protection purposes. Another advantage of LEDs over conventional light sources is the fast switching response, which makes it suitable to be modulated at high frequencies for information delivery without interfering with the illumination function. Therefore, the technology of using LEDs for communication is attractive and promising for futuristic applications, and is called visible light communication (VLC).

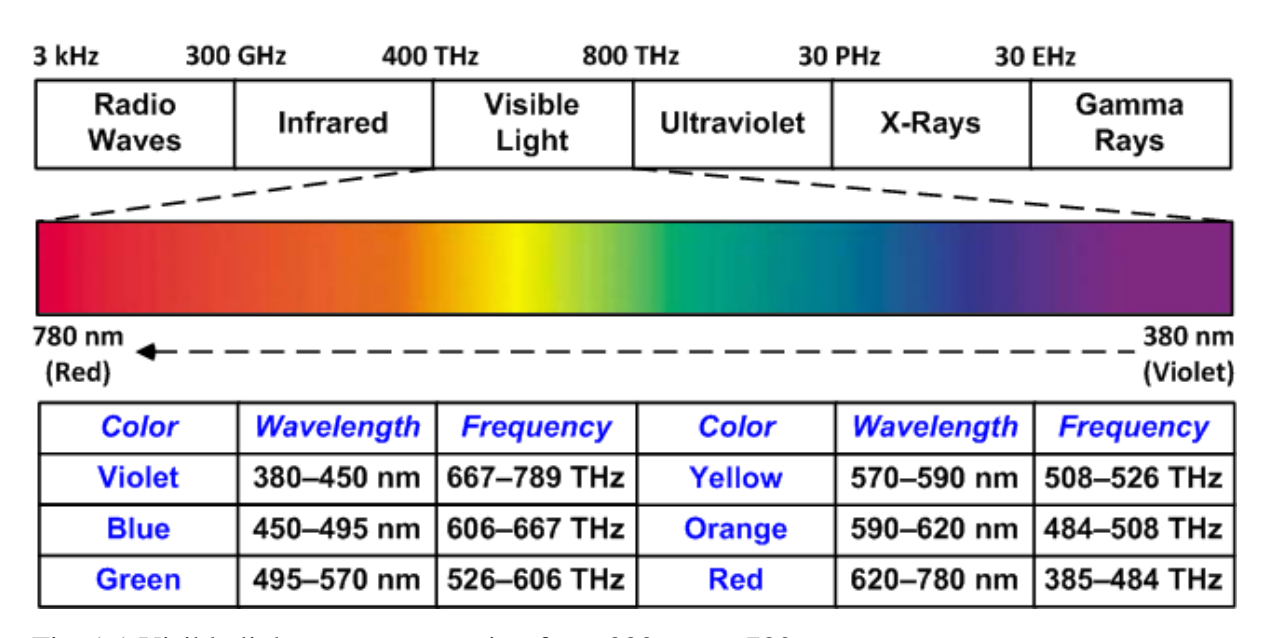


Fig. 1.1 Visible light spectrum ranging from 380 nm to 780 nm.

In general, VLC is a subset of optical wireless communication techniques that utilizes visible light as the communication medium with a wavelength ranging from 380 nm to 780 nm [1] and

frequency ranging from 400 THz to 800 THz (as shown in Fig. 1.1). In VLC systems, data is transmitted by performing optical intensity modulation (IM) on the transmitter side and direct detection (DD) on the receiver side, where the modulation speed is far beyond the flicker fusion threshold of the human eyes to avoid any vision effect. The most distinguished feature of VLC compared to conventional optical wireless technologies such as infrared (IR) and Ultra Violet (UV) communications, is that it supports illumination and communication simultaneously, which enables tremendous futuristic applications. In particular, when various VLC transceivers are networked as a complete wireless system to support bi-directional multiuser communication with point-to-point, point-to-multipoint and multipoint-to-point communication techniques, a LiFi system is formed [2]. In other words, LiFi is a VLC networking system.

The first well-known VLC electronic system dates back to 1880, when Alexander Graham Bell developed a photo-phone to transmit modulated voice data over several hundred meters using sunlight [3]. With the rapid development of high-performance LED lighting systems, the idea to take advantage of the fast switching capability of LEDs for VLC communication was proposed in 1999, when Pang *et al.* at Hong Kong University designed a VLC system with LED traffic lights to provide wireless broadcasting of audio messages [4]. The pioneering work of utilizing universal white LEDs for both lighting and communication was presented by Tanaka *et al.* from Keio University in 2000, where a 100 Mb/s data link based on numerical analyses and computer simulations was reported using an indoor optical channel [5]. A real VLC system with a 100 Mb/s data rate was demonstrated by Oxford University in 2009 [6]. Over the past few years, research groups worldwide have been able to achieve data rates more than one gigabit per second using multiple-input multiple-out (MIMO) transmission, spectral-efficient modulation schemes, and bandwidth enhancement techniques, in conjunction with high-bandwidth light sources [7-10].

1.2 Advantages of VLC

VLC utilizes the light from illumination LEDs as the communication medium to concurrently delivery information through the line-of-sight (LOS) channel, and it has many advantages over conventional RF communications.

(1) License-free operation. The RF spectrum has been assigned by administrative licensing

since the 1930s to ensure the efficient utilization and high communication quality. However, with the demanding data traffic in multimedia communication, cloud computation and other emerging applications, the RF spectrum is becoming congested. Compared to the regulated RF spectrum, the visible light spectrum is available without licensing regulation (mainly due to the LOS characteristics), making it attractive in low-cost applications.

- (2) High bandwidth. In contrast to conventional RF wireless systems with a bandwidth of only 300 GHz, the available visible light spectrum is 1000 times wider (which is about 400 THz) with a much higher capacity for high-speed and short-range wireless communication. In addition, visible light can be easily confined to propagate in a specified direction with optics, providing the potential to be spatially reused in close proximity for higher data density, such as MIMO.
- (3) High security. Since visible light has a wavelength (which typically ranges from 380 nm to 780 nm) that is comparable to the structural elements (such as cracks and porous space) within solid materials, it is scattered after interacting with those materials. In addition, visible light will be absorbed when hitting the paint pigment molecules at the surface of a wall [11]. As a result, visible light cannot penetrate a wall, which provides enhanced security in a well-defined space to avoid being intercepted.
- (4) No electromagnetic interference and hazardous radiation. Due to the much higher frequency of the visible light spectrum than that of the radio spectrum, VLC does not cause electromagnetic interference to existing RF communication systems and other sensitive systems, making it suitable to be deployed in various places where radio wireless is not feasible, such as hospitals and airplanes. In particular, hybrid systems that employ VLC and RF can achieve better performance by taking advantage of the merits of each technology [12-15]. For example, VLC can supplement conventional RF systems to have higher throughput and a larger coverage area, while RF can provide the uplink transmission capability for VLC systems to implement two-way communication. Moreover, visible light generates no health hazards in normal illumination conditions.
- (5) Compatible with existing infrastructure. VLC can be implemented using existing illumination infrastructure, making it attractive for large-scale deployment with relatively low cost. More importantly, infrastructure-based VLC systems can easily integrate with other

functional blocks to enable various Internet of Things (IoT) applications [16-19].

1.3 Implementation of VLC

1.3.1 Typical System Architecture

A typical VLC transceiver system is illustrated in Fig. 1.2. On the transmitter side, the data to be transmitted is encoded and modulated in order to maintain a reliable communication link in different situations and also to keep a constant DC level for illumination. Then the processed signal is applied to the LED driver to modulate the LED current and thus the illuminated light intensity. On the receiver side, the modulated light propagated through the free-space channel is detected by the photodiode (PD), which converts the light into current. The following transimpedance amplifier (TIA) implements current-to-voltage conversion and is connected to the main amplifier to further amplify the signal. The clock and data recovery (CDR) module then extracts the clock from the output of the preceding amplifier and retimes the data for subsequent demodulation and decoding. Optical components such as a lens and a blue filter can be utilized in the transceiver system to improve the link performance.

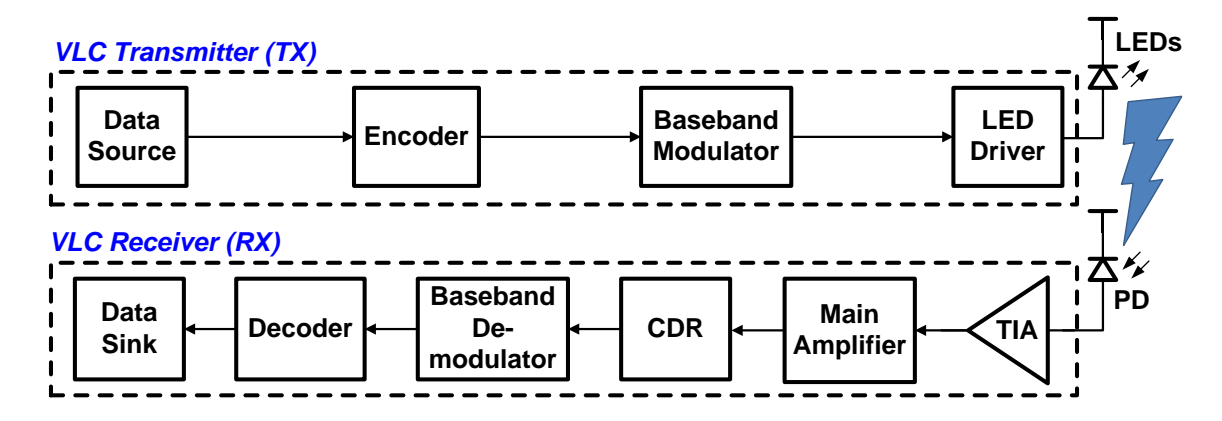


Fig. 1.2 A typical VLC transceiver system.

1.3.2 Modulation Schemes

Different modulation schemes can be applied to VLC systems by making a trade-off between system performance and complexity. Moreover, dimming is usually supported for simultaneous illumination.

On-off keying (OOK) is prevalent in low-complexity applications, where the on-state of LEDs

represents data "1", while the off-state represents data "0". OOK dimming can be implemented by directly adjusting the turn-on current of LEDs or by inserting compensation symbols. The first approach results in varying communication distance according to different dimming levels, while the second approach makes a compromise between data rates and dimming levels. As shown in Fig. 1.3 (a) [20], for 50% brightness, no compensation symbol is needed (because of Manchester encoding in the transmitted data), resulting in the highest data rate, while for the other dimming levels, such as 30% and 70%, compensation symbols with specific duty ratios are required, which reduce the effective communication time and the overall data rates.

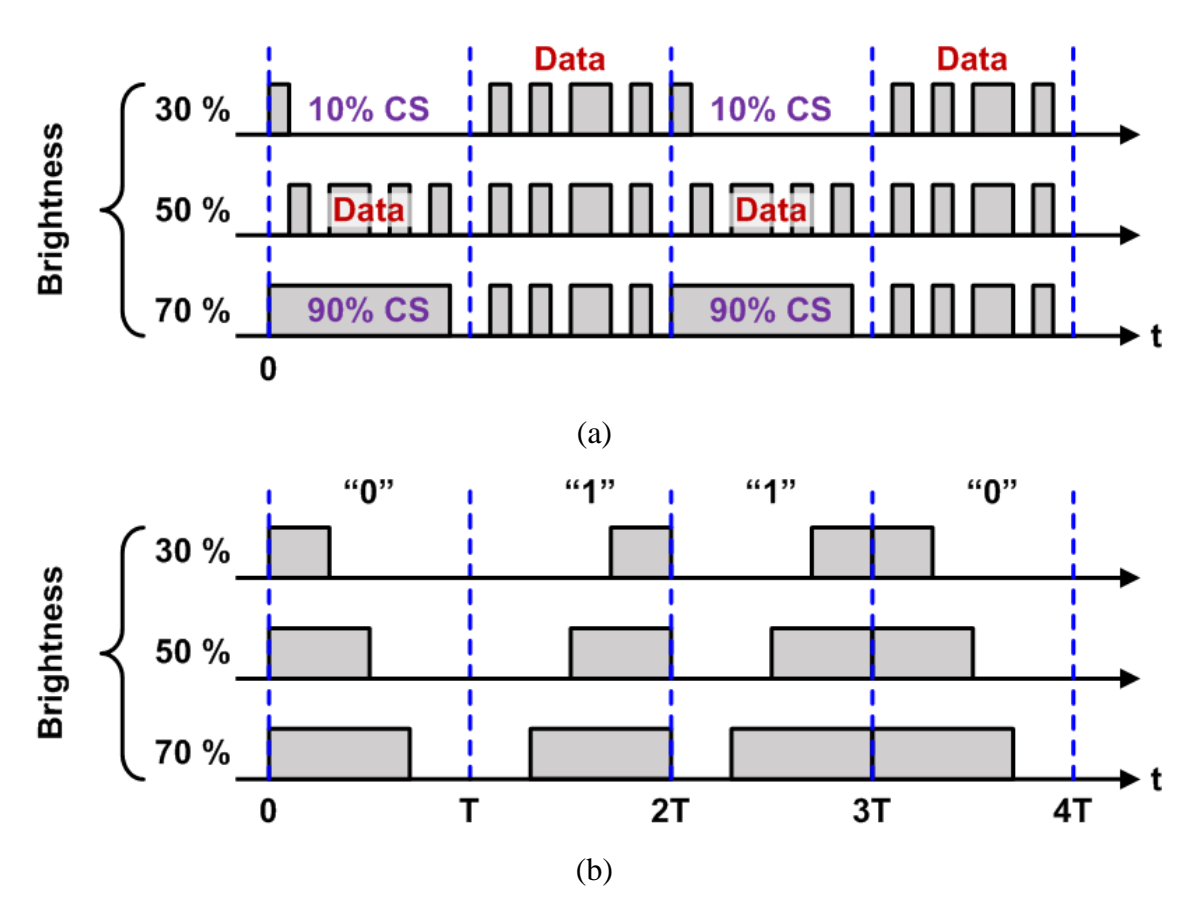


Fig. 1.3 Dimming implementation using (a) OOK, and (b) VPPM [20].

Pulse position modulation (PPM) is another basic modulation scheme for VLC with different positions of the pulse to represent different data. As shown in Fig. 1.3(b), a pulse at the beginning and at the end of one symbol period represent data "0" and data "1", respectively. Dimming levels can be adjusted by changing the pulse width, which is also called variable pulse position modulation (VPPM) [1].

Although OOK and PPM are suitable for low-complexity VLC applications, they suffer from low spectrum efficiency. Therefore, more advanced modulation schemes have been proposed for high-speed VLC systems. Among these schemes, orthogonal frequency division multiplexing (OFDM) is a popular solution to improve VLC data rates as well as mitigate intersymbol interference (ISI) caused by the dispersive optical wireless channel [2, 21]. OFDM exploits a collection of closely spaced orthogonal sub-carriers to transmit parallel data streams simultaneously, which is also known as discrete multitone (DMT). Since each sub-carrier in OFDM is modulated at low speed within a narrow band, channel equalization is simplified compared to wideband modulation. Low-speed subcarriers also facilitate the use of a guard interval between symbols to eliminate ISI. In conventional OFDM systems, the generated signal is complex and bipolar. In OFDM-VLC systems, a real output signal is required, which can be generated by forcing Hermitian symmetry on the subcarriers in the frequency domain [2]. In order to ensure the unipolarity of the OFDM signal for VLC applications, many variants of OFDM have been proposed. In [22], a DC bias is employed for unipolar signal generation, which is called DC biased optical OFDM (DCO-OFDM). In asymmetrically clipped optical OFDM (ACO-OFDM) [23], only the odd subcarriers are utilized to transmit the signal, which has better power efficiency with worse spectral efficiency compared to DCO-OFDM [21]. Other OFDM-based modulation schemes, such as asymmetrically clipped direct current biased OFDM (ADO-OFDM) [24] and pulse-amplitude-modulated DMT (PAM-DMT) [25], have also been proposed to further improve VLC system performance.

An OFDM modulator can be implemented on the VLC transmitter side by using the inverse fast Fourier transform (IFFT) algorithm in a digital signal processor (DSP), followed by a digital-to-analog converter (DAC). On the receiver side, the fast Fourier transform (FFT) and an analog-to-digital converter (ADC) for OFDM demodulation are required. Although OFDM excels in high spectral efficiency, it has several limitations for practical applications. In addition to the complicated algorithm and frequency synchronization, which consume a lot of computing resources, the high requirement on transmitter linearity is also challenging for low-cost commercial LEDs and LED drivers.

1.3.3 Network Topologies

According to IEEE 802.15.7, VLC systems basically operate in three different topologies, including peer-to-peer, star and broadcast, as illustrated in Fig. 1.4. Among these topologies,

there are three different types of devices involved: infrastructure, mobile and vehicle. In particular, the coordinator is a special device that manages the communication.

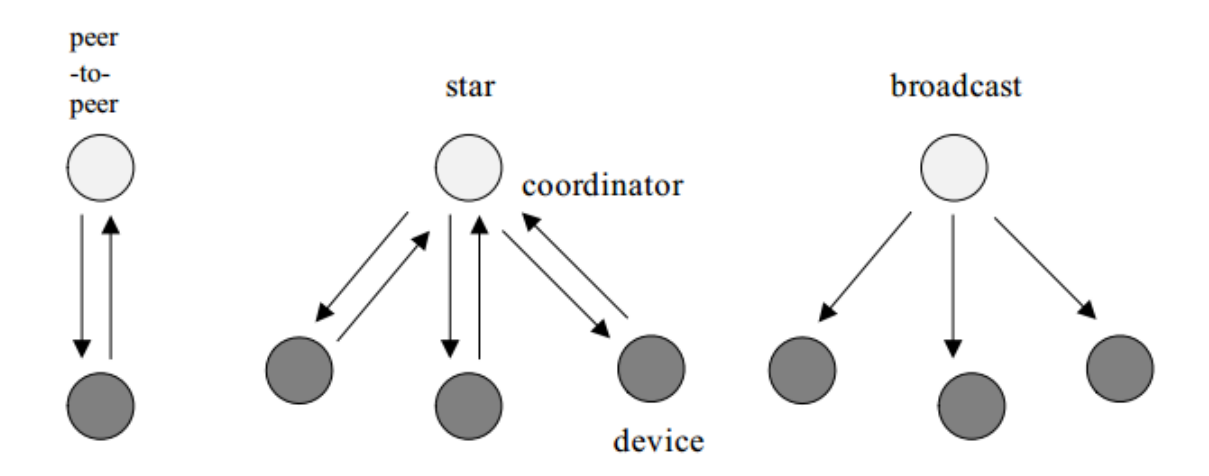


Fig. 1.4 Typical network topologies of VLC systems [1].

Peer-to-peer topology: In this topology, two devices communicate with each other, where one of them acts as the communication coordinator and the other one acts as the client device. This is two-way communication, which requires a downlink and an uplink. The peer-to-peer topology is suitable for high-speed VLC applications.

Star topology: In this topology, communication is supported between the central coordinator and many client devices. This is also two-way communication that requires both downlink and uplink. Compared to the peer-to-peer topology, the challenge of the star topology is how to handle the coexistence of multiple channels and avoid interference with each other. A typical application of this topology is the VLC wireless access network.

Broadcast topology: In this topology, the device in the broadcast mode can only transmit message to other devices. Since this is one-way communication that simply requires a downlink, the system is the least complex among all the three topologies, which makes it attractive for massive deployment with low cost in IoT applications such as indoor localization and indoor information broadcasting.

1.3.4 VLC Systems with Different Light Sources

In VLC systems, the light source is significantly important to emit modulated visible light at

data rates ranging from megabit per second to gigabit per second. Up to now, various VLC system prototypes have been developed and verified, where micro-LEDs (µLED) and laser diodes (LDs) are utilized as light sources in addition to ordinary commercial LEDs, as described below.

VLC using commercial LEDs. OOK is extensively adopted in VLC due to the low complexity as mentioned before. In 2008, multiple-resonant pre-equalization was employed to extend the -3dB bandwidth of a white LED to 45 MHz and OOK modulation was applied to achieve a data rate of 80 Mb/s with a short distance of only 10 cm [26]. In 2014, a VLC link containing a phosphorescent white LED with a post-equalized -3dB bandwidth of 151 MHz was demonstrated to support data rates up to 340 Mb/s using OOK modulation at a distance of 43 cm [27]. Later in the same year, an OOK VLC system based on a similar LED in conjunction with both pre-equalization and post-equalization circuits was reported to further increase the -3dB modulation bandwidth to 233 MHz and the achieved data rate was 550 Mbit/s over a 60 cm distance [28]. Spectral-efficient modulation schemes have also been exploited for VLC applications. In 2010, a DMT based VLC link operating at 100 Mbit/s over a distance of 1.4 m using a white LED was presented [29]. In 2012, rate-adaptive DMT modulation for VLC was proposed to achieve data rates up to 1 Gb/s over 15 cm using a phosphorescent white LED [30]. In 2013, MIMO-OFDM was employed to enable 4-channel VLC transmission at a 1 Gb/s data rate using 4 phosphorescent white LEDs over a distance of 1 m [7]. In 2014, a VLC link involving 12 LEDs with 4 different colors (red, green, blue and amber) and WDM-OFDM modulation could support communication data rates as high as 5.6 Gb/s at a distance of 1.5 m [31]. In these systems, blue filters were utilized for bandwidth extension when employing phosphorescent white LEDs, and lenses were also adopted to strengthen the received signal.

Although a lot of progress has been made in VLC development, most of the demonstrated VLC prototypes are constructed with discrete components, resulting in high power consumption, large form factor, and high cost. Therefore, it is necessary to integrate VLC systems on chip for practical applications. Relevant advances have been reported. In 2014, a VLC transceiver System-on-Chip (SoC) was implemented, enabling the transmission of a 12 MHz input data stream using a pre-equalization technique and OOK modulation via a single-color blue LED [32]. However, critical system performance information such as BER and communication distance was not presented. In 2015, a VLC transmitter chip and a VLC receiver chip were

reported [2, 33, 34]. The transmitter is an open-drain 8-bit current steering DAC-based LED driver capable of achieving 250 MS/s for OFDM or PAM modulation, while the receiver is composed of 49 avalanche photodiode (APD) detectors (which is a 7×7 detector array), each with a size of 200×200 μm² placed on a grid with 240 μm spacing. In 2016, a fully integrated IEEE 802.15.7 standard-compliant VLC transmitter with on-chip LED driver was designed with data rates up to 266 kb/s using ordinary phosphorescent white LEDs [20]. The measured communication distance was 2 m using no optical lens with high energy efficiency of 5 nJ/bit. Both OOK and VPPM were supported according to the standard specification.

2. VLC using μ LEDs. A μ LED usually has a small size with the diameter of only tens of micrometers [35], which makes the parasitic capacitance significantly reduced compared to ordinary LEDs, of which the size is 100 times or even 1000 times larger. In addition, a μ LED has much higher current density for the same bias current. Therefore, μ LEDs have a wide modulation bandwidth that is promising for high-speed VLC applications [36], although the efficiency drops due to the increase of current density [37]. In 2014, a VLC system was implemented using white light generated by a blue GaN μ LED and a custom fluorescent conjugated polymer [38]. Since the μ LED has a bandwidth of 60 MHz with a diameter of 50 μ m and the conjugated polymer has short fluorescence lifetime, a high data rate of 1.68 Gb/s can be achieved using DCO-OFDM at a distance of 3 cm. By employing pre- equalization and post-equalization techniques as well as adaptive bit and energy loading with M-QAM DCO-OFDM modulation on a similar blue GaN μ LED, a VLC link with data rates exceeding 3 Gb/s was demonstrated within a 5 cm distance [36]. In 2016, a 3-tap feed-forward pre-equalization technique and a PAM-4 modulation scheme were proposed to achieve 2 Gb/s VLC transmission over 0.6 m using a μ LED with a size of 20×20 μ m² and a bandwidth of 150 MHz [39].

In the scenarios where μ LEDs are grouped in an array for display or illumination, VLC can also be applied. In 2012, a 16×16 μ LED array was flip-chip bonded to a matched CMOS driver for either dynamic image display or high-speed VLC at data rates up to 250 Mb/s using OOK modulation, where the μ LED is 72 μ m in diameter with a bandwidth of 100 MHz [40]. In 2015, a 6×6 μ LED array in MIMO operation achieved data rates beyond 1 Gb/s at a distance > 1m with OOK modulation and a decision feedback equalizer (DFE), where the diameter and the bandwidth of the μ LED are 39 μ m and 125 MHz, respectively [34]. However, display and VLC are not supported simultaneously in these systems.

3. VLC using LDs. As mentioned before, there exists a trade-off between the optical efficiency and the modulation bandwidth of LEDs due to the "efficiency droop" problem [37]. In contrast, LDs can maintain high efficiency at high current density, enabling a larger intrinsic bandwidth than LEDs for high-speed optical communication. In 2015, a VLC system using a GaN 450-nm LD with 2.6 GHz bandwidth and OOK modulation was reported to achieve 4 Gb/s at a distance of 15 cm [41]. In the same year, a VLC link consisting of RGB LDs was reported to enable 3.4 Gb/s high-speed communication at a distance beyond 2.8 m, and the bandwidth was 230 MHz for the red LD, 780 MHz for the green LD and 1 GHz for the blue LD [42]. Another GaN 450-nm LD with a 1.5 GHz bandwidth was employed to achieve 9 Gb/s communication over a 5-m free-space link using 64-QAM OFDM in [43]. In 2016, 2.5 Gb/s OOK modulation was implemented over a 12 m distance via a 680-nm 5-GHz bandwidth LD with an integrated receiver [44]. Optical components were involved in these systems to focus the transmitted light onto the receiver front-end.

Table 1.1 Comparison of VLC systems using different light sources

| VLC Lighting Source | Commercial LED | μLED | LD |
|-------------------------------|----------------|--------|-------|
| Lighting Source Cost | Low | Medium | High |
| Optical Power Density | Low | Medium | High |
| Modulation Bandwidth | Low | Medium | High |
| Directivity | Low | Low | High |
| Coverage Area | Large | Large | Small |
| Communication Distance | Short | Short | Long |

However, the high directivity of LDs makes them more suitable to act as an auxiliary component in a general illumination system and serve for communication purpose [44].

VLC systems using different light sources are compared and summarized in Table 1.1.

1.4 Application of VLC

VLC supports simultaneous illumination and communication functions, and can integrate with

various sensors and mobile computing capabilities to enable different indoor and outdoor applications.

1.4.1 Smart Lighting



Fig. 1.5 Indoor illumination system integrated with VLC techniques to enable a smart house [45].

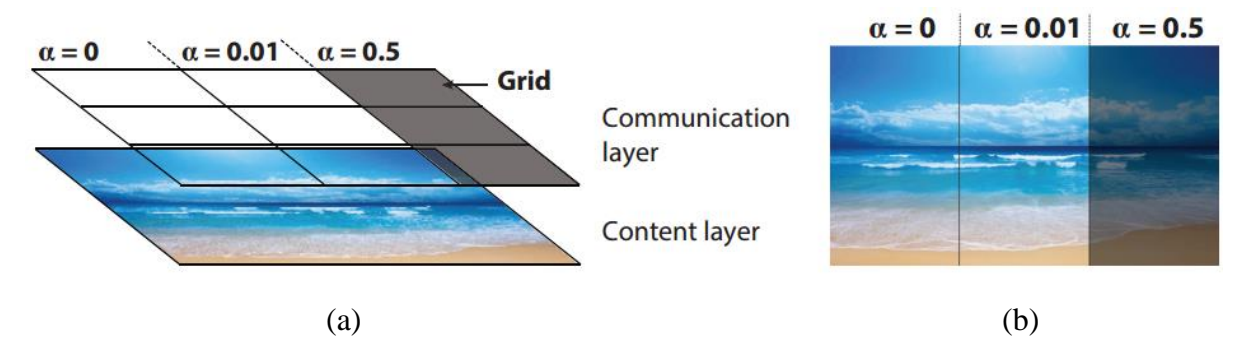
VLC can enable various attractive indoor applications by connecting household devices using a VLC-based wireless sensor network (WSN) and performing communication, monitoring and control, as illustrated in Fig. 1.5 [45]. In particular, indoor luminaires integrated with VLC techniques can act as wireless data access points (APs), through which laptops, desktops and televisions etc. can be connected to the Internet with as few cables as possible. Moreover, the light intensity and color temperature of the indoor luminaires can be monitored by embedded sensors, and relevant information will be delivered to the control center by the VLC network for intelligent control, such as low light for watching video, blue color for better resting and auto lighting control for saving energy [46]. In [46], each light is equipped with an occupancy sensor in addition to a light sensor to detect the local occupancy. Therefore, the illumination level in different zones is automatically adjusted according to the occupancy conditions.

1.4.2 Smart Display

Display screens of televisions, desktops, laptops, smartphones, digital signage etc. utilize LEDs

as the backlighting module. In some display technologies, the screen is even made up of LEDs directly, such as organic LED (OLED) displays. Therefore, VLC can also be combined with displays to enable various potential applications. Since both imaging receiver (such as a smartphone camera) and non-imaging receiver (such as a PD) can be employed in VLC systems, there are two typical smart display techniques, as described below.

(1) Smart display with camera (screen-camera communication). In [47], a link consisting of an LCD and a camera was proposed to implement VLC communication. An OFDM transmission algorithm was employed to overcome issues existing in this unique application, including perspective distortion (due to the presence of viewing angle), blur (due to handshaking, movement or lack of focus) and sensitivity to ambient light. A prototype using off-the-shelf LCDs and cameras was built and experimental results showed that the LCDcamera link was cable of achieving VLC data rates of up to 12 Mb/s at a distance of 10 m and a view angle of 120°. In [48], VLC data was encoded into pixel translucency change on top of screen content by leveraging the properties of the orthogonal transparency (alpha) channel, enabling various applications such as augmented reality. As illustrated in Fig. 1.6 (a), a separate communication layer was added on top of the content image layer on the screen. Data transmission was achieved without significantly affecting the viewing experiences of the display by dividing the communication layer into grids and encoding data into the change of corresponding alpha value in each grid. Fig. 1.6 (b) is the resulting composite image after modifying the alpha value of the communication layer, while (c) shows the demonstration of the system, where the image on the transmitter was encoded with VLC data, and the receiver camera captured the picture to extract the transmitted data, which was displayed on the camera screen. The limitation of screen-camera communication is that the high operation frequency of the camera consumes a lot of power and shortens the battery runtime of the mobile device [49]. Therefore, it is more suitable for low-speed VLC applications.



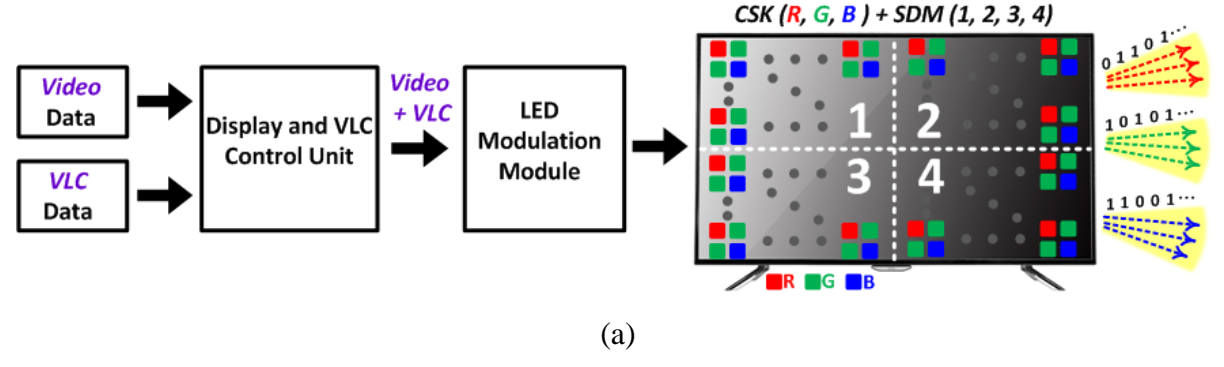


(c)

Fig. 1.6 (a) An extra communication layer on top of the content layer, (b) the resulting composite image after modifying the pixel translucency of the communication layer, and (c) demonstration of the system, where the image on the transmitter was encoded with data, and the receiver camera captured the picture to extract the transmitted data, which was displayed on the camera screen [48, 50].

(2) Smart display with PD. To achieve higher communication data rates, a PD-based receiver can be employed, as depicted in Fig. 1.7. This is a potential architecture that simultaneously supports video display and high-speed VLC. On the transmitter side, video data and VLC data are synchronized by the display and VLC control unit, which is indispensable to avoid data loss when the display patterns or time slots are not available for data transmission. In addition, run-length limited encoding (such as Manchester encoding, 4B6B) is utilized to maintain constant DC current for display. Since display screens consist of a large-scale LED pixel array with 3 different colors (namely red (R), green (G) and blue (B)), color shift keying (CSK) and space division multiplexing (SDM) can be utilized to implement parallel data transmission for high throughput. Fig. 1.7(a) is the case where both CSK and SDM are adopted by dividing the screen into four quarters (namely 1, 2, 3 and 4), meaning that there are 3 parallel channels in each of the four quarters, and 12 parallel data transmissions in total can be supported simultaneously. Correspondingly, there exist three PDs on the receiver side to detect the modulated VLC signals, with optical filters located in the front to select one of the RGB channels, as shown in Fig. 1.7 (b). A trans-impedance amplifier (TIA) with automatic gain control (AGC) function is needed in each channel to accommodate different link conditions. Finally, the large dynamic input range due to various display patterns requires advanced algorithms (such as an adaptive decision algorithm) on the receiver side to extract the transmitted data correctly by automatically adjusting the decision threshold value.

Transmitter for Smart Display



Receiver for Smart Display

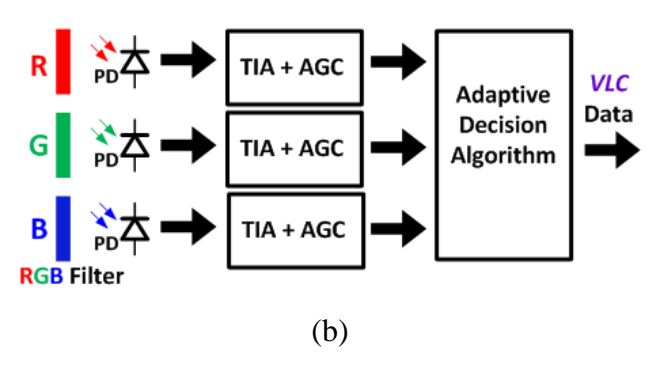


Fig. 1.7 Potential architecture for smart display: (a) transmitter for a smart display, and (b) receiver for a smart display.

Although this system has the potential to support high-speed VLC, there are some difficulties in the implementation. The first one is adjacent channel interference in SDM, which is increased with respect to the number of parallel channels. Another one is how to optimize the system performance by choosing a proper number of CSK and SDM channels based on the dynamic display patterns. Finally, different viewing angles also affect the system performance, which should be overcome to extend the application.

1.4.3 Sensing

There is a growing interest in utilizing VLC combined with custom algorithms to implement sensing and detection [51-54]. The operation principle is that the light emitted by LEDs will be affected (such as being blocked or being reflected) by objects in the proximity, which will result in varying signal amplitude on the receiver side and can be used to sense motion, gesture, etc. In [51], a finger localization system consisting of one LED and two light sensors (PDs) was proposed to enable virtual keyboard and trackpad applications for devices with small form

factors. A light propagation/reflection model with 3-point calibration was adopted to guarantee one-centimeter detection precision. In [52], a real-time human skeleton reconstruction using VLC was demonstrated. As illustrated in Fig. 1.8 (a), there is an LED on the ceiling, and a human body blocks the light beam to produce a shadow on the floor, which is a twodimensional projection of the body and will change when the body has different postures. By continuously recording the shadow on the floor, the postures and thus the behavior of the human can be tracked. In Fig. 1.8 (b), a test bed was built with five LEDs on the ceiling and a PD array on the floor. Light beams generated by the five LEDs were modulated at different frequencies, which can be identified in the frequency domain using FFT. In [53], a landing and a take-off assistance network architecture combining VLC and free space optics (FSO) was proposed, where LED sensors were used to detect the runway state and information was relayed to two gateways to be further processed and sent to the approaching aircraft. As depicted in Fig. 1.9, LED lamps on both sides of the runway are equipped with sensors to detect the runway conditions such as the level of water, snow and the presence of obstacles, which will be relayed between adjacent LEDs using VLC techniques until it reaches the aircraft embedded with PDs in both wings. Wavelength division multiplexing (WDM) was adopted to avoid the interference between different VLC links.

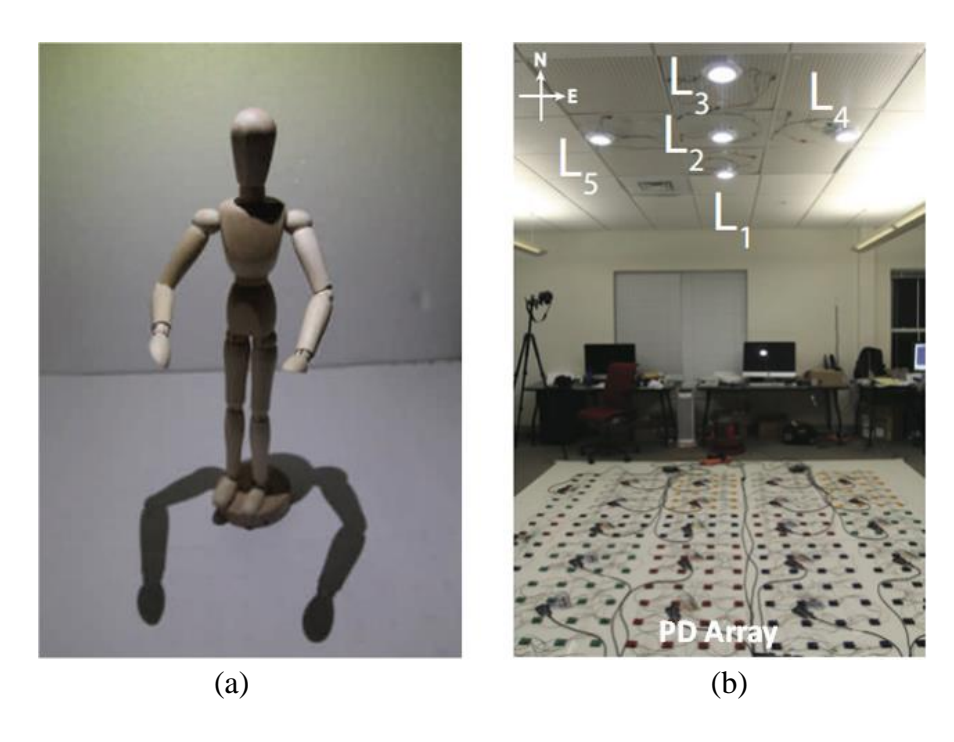


Fig. 1.8 Human sensing VLC system: (a) posture shadow of a manikin under a ceiling LED, and (b) a test bed consisting of five LED lights and 324 PDs [52].

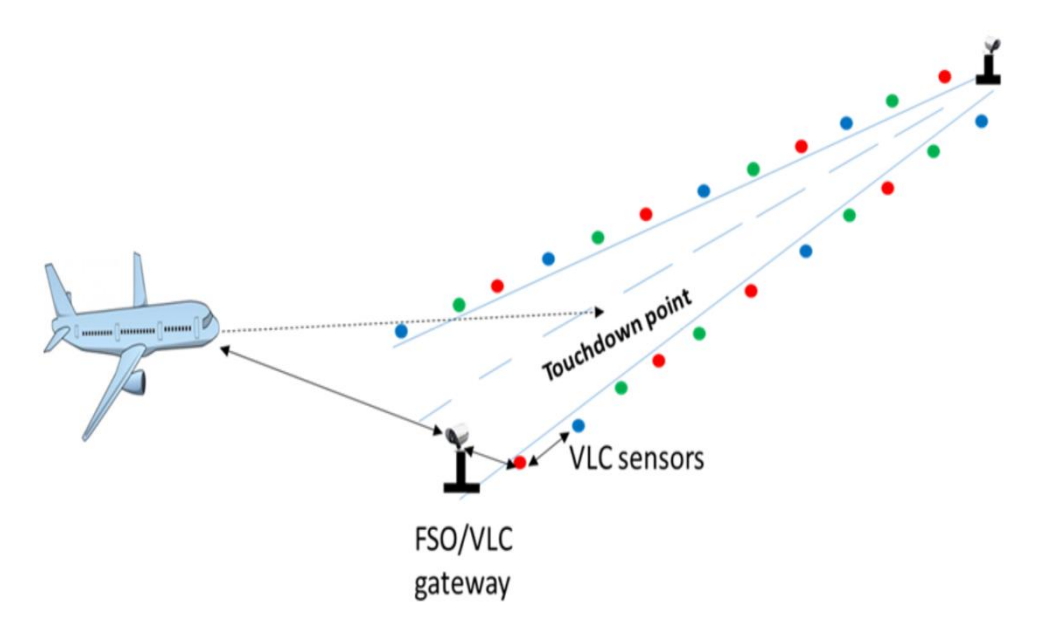


Fig. 1.9 Landing and take-off assistance network architecture [53].

1.4.4 Indoor Positioning

Indoor positioning (or localization) makes use of various technologies to locate and track objects or people inside a building. It is expected that the market for mobile indoor localization in the retail sector will reach 5 billion by 2018 [55]. Although there exist several positioning systems such as the global positioning system (GPS), the global navigation satellite system (GLONASS) and Galileo, their accuracy (which is typically larger than 2 m) is not high enough for indoor applications. In addition, since the RF signal from satellites suffers a lot of attenuation caused by construction materials and multipath effects, the indoor positioning accuracy of the above systems is further limited. In contrast, WiFi-based indoor positioning provides wide coverage in indoor spaces by avoiding signal blockage; however, its accuracy is still not sufficient (about 1 m) for futuristic applications such as robot navigation in a limited indoor space.

Since VLC can enable indoor luminaires as accessible location identities to broadcast the information of their respective locations, it is also an alternative solution for indoor positioning. As the density of indoor luminaires is usually much higher than that of WiFi APs, the accuracy of indoor positioning systems can be further improved by using VLC. A typical VLC-based indoor positioning system is depicted in Fig. 1.10 [56]. The system consists of visible light beacons, a visible light sensor and a cloud/cloudlet server. The beacons are custom luminaires embedded with a programmable oscillator or microcontroller that can broadcast their identity

information with modulated visible light. Each beacon has a unique modulation frequency. The visible light sensor actually is a smartphone camera used to receive these transmissions by taking pictures periodically and processing the pictures using local and cloud resources. If the frequencies of beacons are detected, then the captured pictures will be further processed to determine the precise location and orientation of the smart phone in the beacons' coordinate system using an angle-of-arrival (AoA) localization algorithm. This system can achieve indoor positioning accuracy of about 10 cm with an orientation error of about 3° using at least four beacons. If the number of visible beacons is fewer than four, the position errors drop substantially, meaning that a high density of overhead light as positioning beacons is required. In addition, the beacon position should also be known in advance for the proper operation of the system. In [57], a mobile robot was built to easily collect the fingerprint distribution information of LED beacons for accurate indoor positioning, as shown in Fig. 1.11. The robot provides training data with locations through four visible light detectors to perform current-tovoltage conversion and signal amplification. Since indoor VLC systems are expected to complement the existing RF systems for high throughput and larger coverage area, hybrid positioning systems combining VLC and RF technologies have been proposed to achieve better system performance, such as improved positioning accuracy and expanded service area [58].

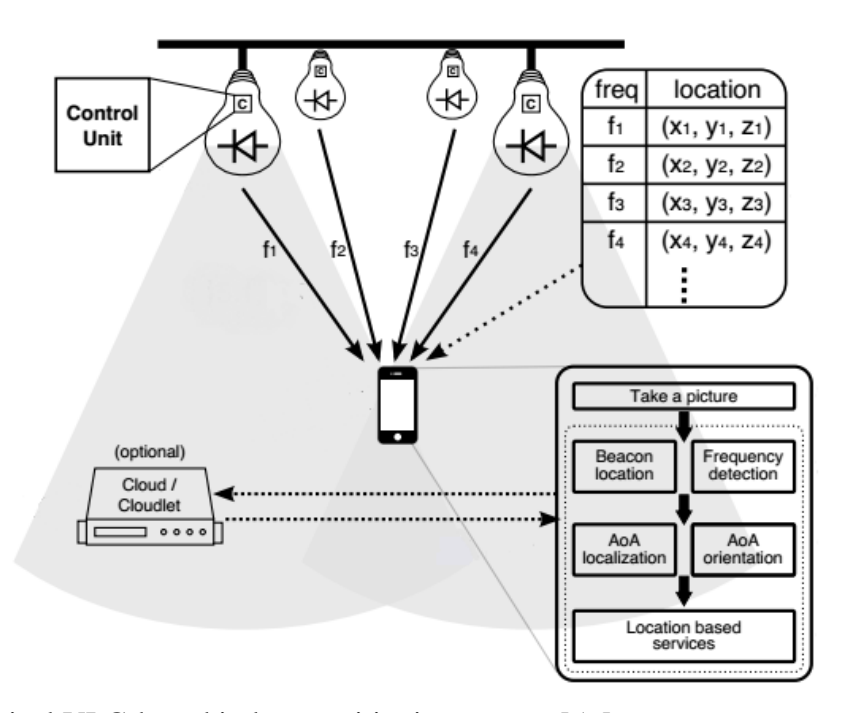


Fig. 1.10 A typical VLC-based indoor positioning system [56].

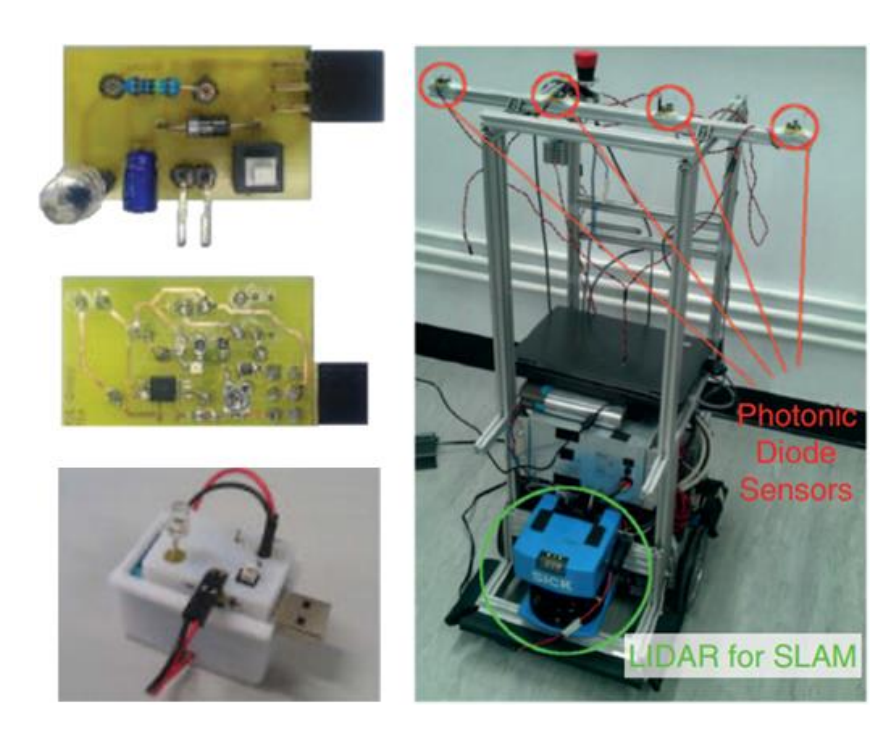


Fig. 1.11 A mobile robot used to easily collect the fingerprint distribution information of LED beacons [57].

1.4.5 Vehicle Communication

VLC can be employed in traffic systems to enable intelligent and safe transportation, which is called vehicle communication. There are two kinds of vehicle communication, including vehicle to vehicle (V2V) and vehicle to infrastructure (V2I) communication. Fig. 1.12 depicts typical V2V and V2I application scenarios [59, 60]. In particular, V2V exploits the VLC signal from headlights and taillights to transmit information such as emergency brake warnings, forward collision warnings and control loss warnings. In V2I applications, the high-speed connection between vehicles and roadside traffic infrastructure, such as traffic lights, street lights, is able to provide Internet access as well as useful traffic information including lane change warnings, traffic signal violation warnings and so on to perform intelligent traffic control and avoid accidents. On the receiver side, not only cameras (as shown in Fig. 1.12) but also PDs can be used to detect the modulated VLC signal and improve traffic safety and efficiency [59-62].

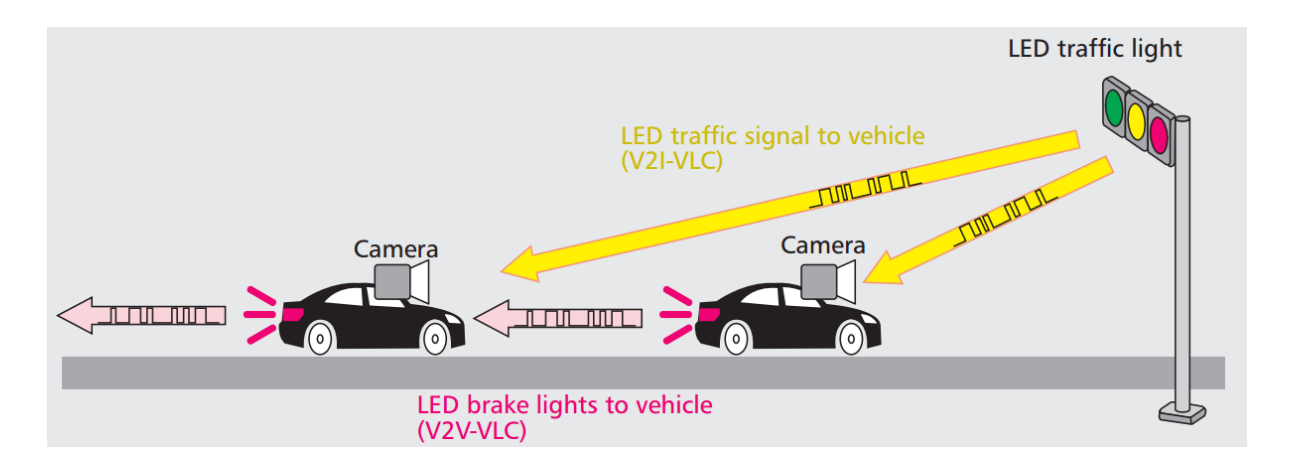


Fig. 1.12 Vehicle-to-vehicle VLC (V2V-VLC) using LED headlights or LED brake lights and vehicle-to-infrastructure VLC (V2I-VLC) using LED traffic lights [59].

1.4.6 Underwater Communication

The growing needs of various underwater activities (such as unmanned underwater vehicle control, offshore facility maintenance, inspection, diving, etc.) have motivated a lot of research on VLC-based underwater communication techniques for high-speed applications [63-66]. Although conventional acoustic communication can support data transmission over long distances, the data rates are limited to be only tens of kb/s (even for short distances within a few meters) [64]. With the application of RF technologies, the data rates of underwater communication can be further improved. However, RF signals suffer a lot of attenuation in sea water, limiting the communication distance. In contrast, the underwater attenuation of bluegreen optical signals is relatively low, which makes it suitable for high-speed applications over a relatively long distance (depending on the operation environment, such as the impurity of water) with much higher energy efficiency than that of acoustic communication [64-65]. In [65], a VLC system was developed to complement existing acoustic systems for underwater communications, which was able to support high data rates with low latency for real-time applications. The VLC system covered a communication distance of over 100 meters with data rates up to 10 Mb/s using a few tens of Watts of battery power. One typical application of this hybrid VLC/acoustic system is illustrated in Fig. 1.13, where (a) shows low-speed communication between an untethered remotely operated vehicle (UTROV) and a surface vessel using low-bandwidth acoustics, while (b) and (c) are the high-speed VLC through either a small ship-based relay or fixed infrastructure on the seafloor, respectively [65].

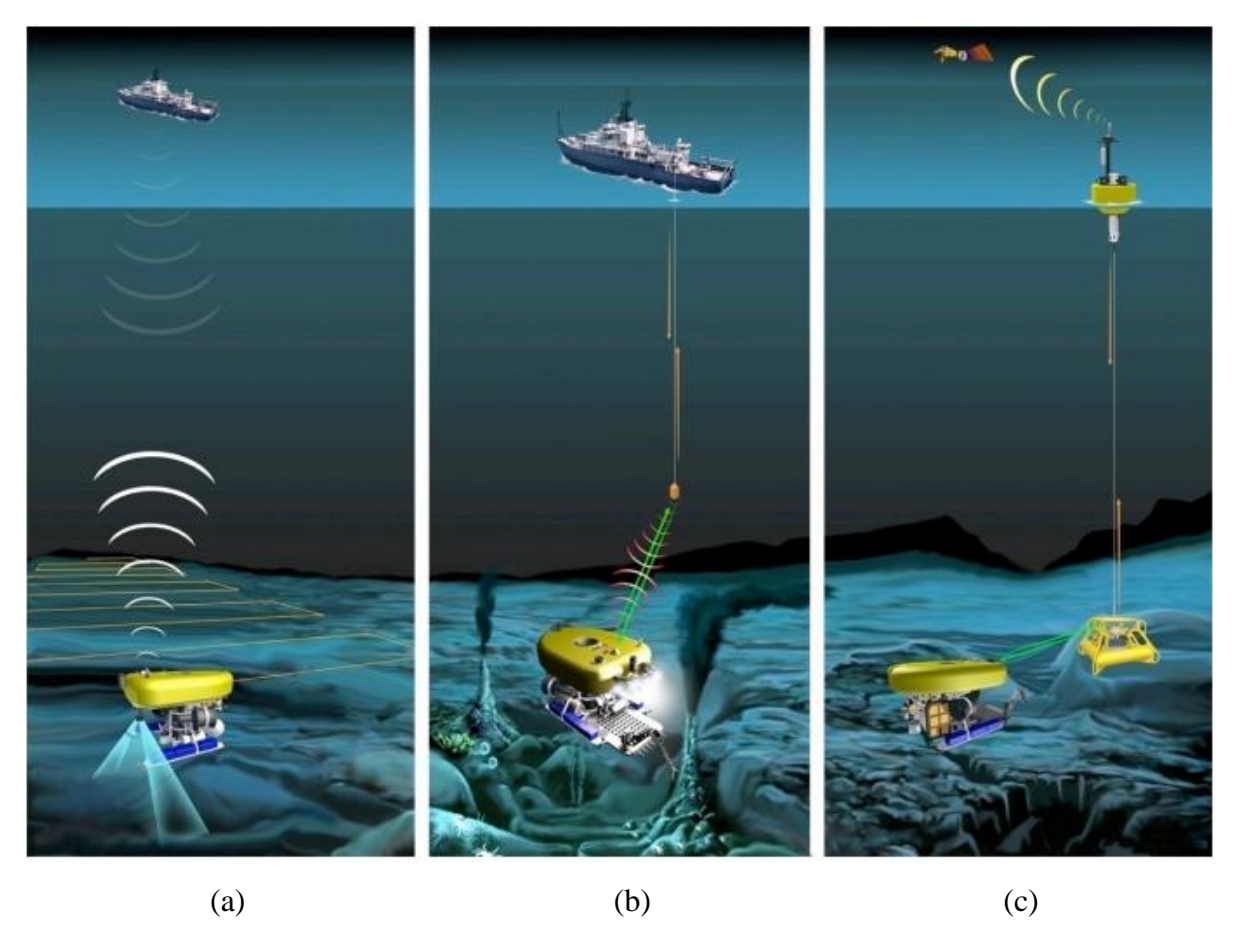


Fig. 1.13 Operation of an untethered remotely operated vehicle (UTROV) with hybrid VLC/acoustic communications: (a) with low-speed acoustic communication, (b) with high-speed VLC through a small ship-based relay, and (c) with high-speed VLC through fixed infrastructure on the seafloor [65].

1.5 Scope of Research

In this thesis, two SoCs are implemented using standard CMOS processes to meet the needs of futuristic IoT applications, which achieve a higher integration level with better efficiency, smaller form size and lower cost. In particular, a novel system architecture to support simultaneous display and communication using LEDs is proposed and is fully integrated as a transmitter SoC. In addition, an energy-efficient VLC receiver SoC is proposed and verified, which integrates an on-chip post-equalization technique to extend the bandwidth of a common VLC system employing commercial phosphorescent white LEDs for high-speed IEEE 802.15.7 PHY-II applications without using a blue filter.

CHAPTER 2 LED Micro-display Technology

2.1 Introduction

Micro-display is an emerging flat panel display technology that employs an array of microscopic LEDs as individual pixel elements [67-70]. Various micro-display technologies are expected to provide consumers with portable and high-quality display systems for emerging applications such as smart glasses (including virtual reality (VR), augmented reality (AR)) and smart watches.

In general, there are two different micro-display technologies, including non-emissive and emissive micro-display. Non-emissive systems utilize optical effects to convert light from a separate backlighting source into graphics patterns, such as a liquid crystal on silicon (LCoS) micro-display. In contrast, emissive systems consist of self-emitting devices as individual pixel elements and graphic patterns are displayed by directly configuring the pixels, such as OLED and LED micro-displays.



Fig. 2.1 Google Glass explorer edition [71].

Among these display technologies, LCoS is the most mature one, and has been engaged in massive production, such as Google Glass and Kopin Solos [70]. As shown in Fig. 2.1, Google Glass is an eye-worn smart LCoS micro-display embedded with custom optics to display information into the user's eye and with a touchpad located on one side to enable user control [71]. However, LCoS requires a separate backlighting source that is always turned on during display regardless of whether the display pixels are on or off, resulting in relatively low energy efficiency. Different from that, emissive micro-displays are more energy-efficient. One of popular emissive micro-displays is color-filtered OLED technology. However, the electrooptical performance, energy efficiency and device lifetime of OLEDs are still inferior to inorganic LEDs, especially when operating in high brightness conditions. Moreover, full-color OLED micro-displays are currently based on filtering broadband white emitters to obtain the required RGB primary colors, which requires much higher driving current and shortens the lifetime of OLEDs [72]. As another candidate of emissive micro-display technologies, inorganic LED micro-displays intrinsically have high efficiency, long lifetime and high reliability in extreme conditions, making them suitable for commercial and military applications.

2.2 Passive Matrix Driving Scheme of LED Micro-display

Passive matrix driving is utilized for low-resolution and small-scale micro-displays due to low complexity and low cost. As show in Fig. 2.2, each LED pixel has a shared anode on the same column data line (such as V_DATA1) connected to display data interface, and a shared cathode on the same row selection line (such as V_SEL2) connected to display control interface. When a specific row is activated, the corresponding row selection line is set to be logic low, and the status of each pixel on that row is dependent on the column data lines. Since data can not be retained locally on each pixel, the passive matrix has to maintain a relatively high row scanning frequency to achieve quality display. When the number of rows and columns increase, more power will be lost due to higher refreshing rate, limiting its application in large-scale display.

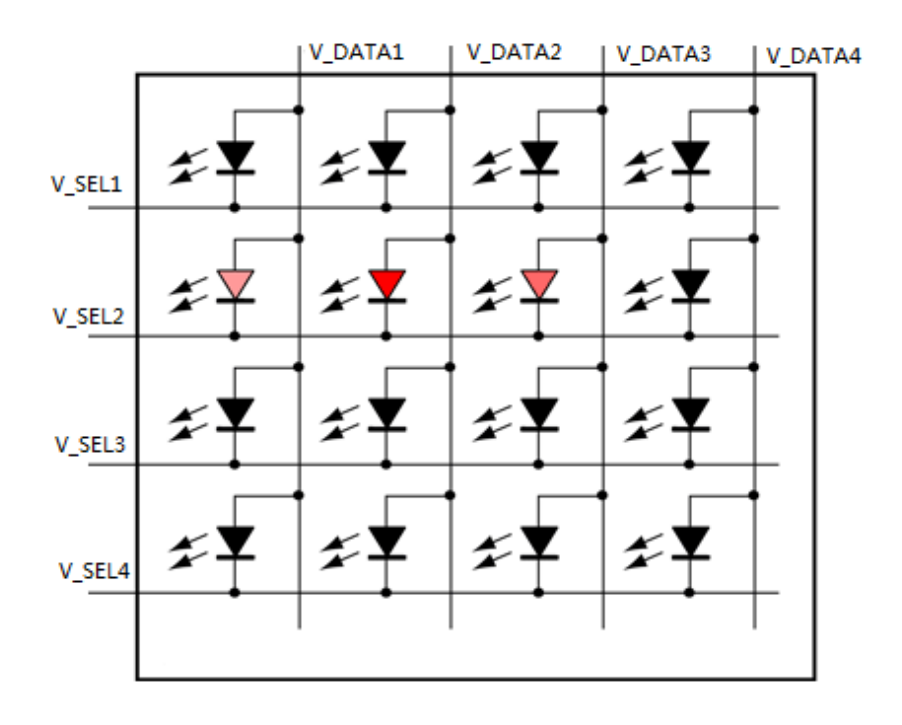


Fig. 2.2 Passive matrix driving scheme of an LED micro-display [73].

2.3 Active Matrix Driving Scheme of LED Micro-display

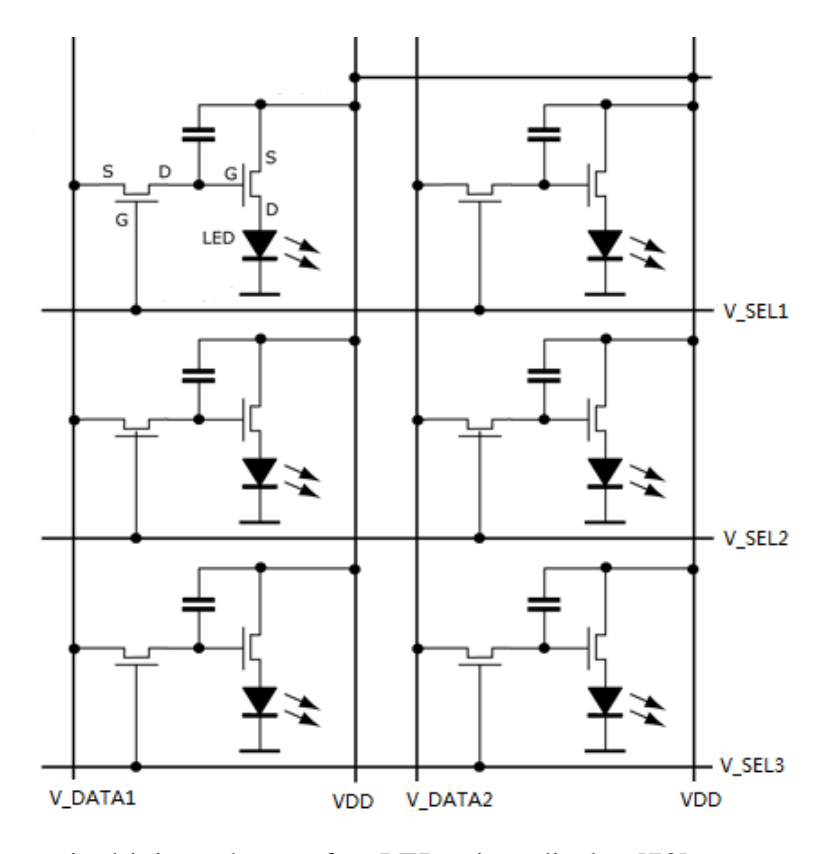


Fig. 2.3 Active matrix driving scheme of an LED micro-display [73].

In high-resolution and large-scale micro-displays, active driving is preferred to avoid high refreshing rate and thus reduce the related power consumption by adding one driver circuit to each pixel locally, which integrates memory function on chip. As depicted in Fig. 2.3, this is an active matrix driver array for LED micro-display. Each driver unit consists of two transistors and one capacitor. Different from a passive matrix driving scheme, the micro-LED pixels in an active matrix have independent anodes connected to corresponding driver units, which are usually fabricated on silicon substrate using CMOS technology. Therefore, hybrid integration with flip-chip bonding is necessarily to connect the GaN-based micro-display and the silicon-based driver array.

2.4 Fabrication Process of LED Micro-display

The fabrication process of an LED micro-display is described as follows [72].

- (1) Mesa etching: GaN micro-LEDs are grown on sapphire substrate using metal-organic chemical vapor deposition (MOCVD). To reduce light scattering, wafers need to be treated at high temperature using rapid thermal annealing (RTA) before fabrication.
- (2) Current spreading layer deposition: Ni/Au and ITO (1150 Å) are utilized as current spreading layer to distribute the LED current over the whole p-GaN uniformly, such that current crowding effect can be avoided. In this process, two-step annealing is employed to improve the conductivity of the ITO layer while maintaining the contact resistance and transparency.
- (3) Electrode deposition: The sample surface needs to be processed first with O₂ plasma to completely remove residual photoresist from the exposed areas. Then metal layer is deposited by E-beam evaporation.
- (4) Surface passivation: A silicon dioxide passivation layer with a thickness of 1 μm is deposited at the surface of the micro-LED array first by PECVD. Then opening windows on p- and n-electrodes are defined through photolithography and buffer oxide etchant (BOE) wet etching.

CHAPTER 3 VLC Transmitter Embedded in Active Matrix LED Micro-display

3.1 Introduction

Owing to their superior energy efficiency and reliability over traditional light sources, LEDs have been widely deployed for illumination, signaling and display applications [74, 75]. In particular, micro-LED (μ LED) displays [76-78] have received a great deal of research interest due to their unique advantages. First, the diameter of a μ LED is within tens of micrometers, and thus high-resolution display panels can be implemented by integrating a large-size LED array on a single substrate. Second, the compact size of μ LED display facilitates the system integration with a CMOS driver, enabling a miniaturized and reliable portable micro-display. Third, each μ LED pixel in the array is individually addressable such that display in a small area is feasible for other potential applications, such as multisite excitation [79], cell manipulation [80], and lithography.

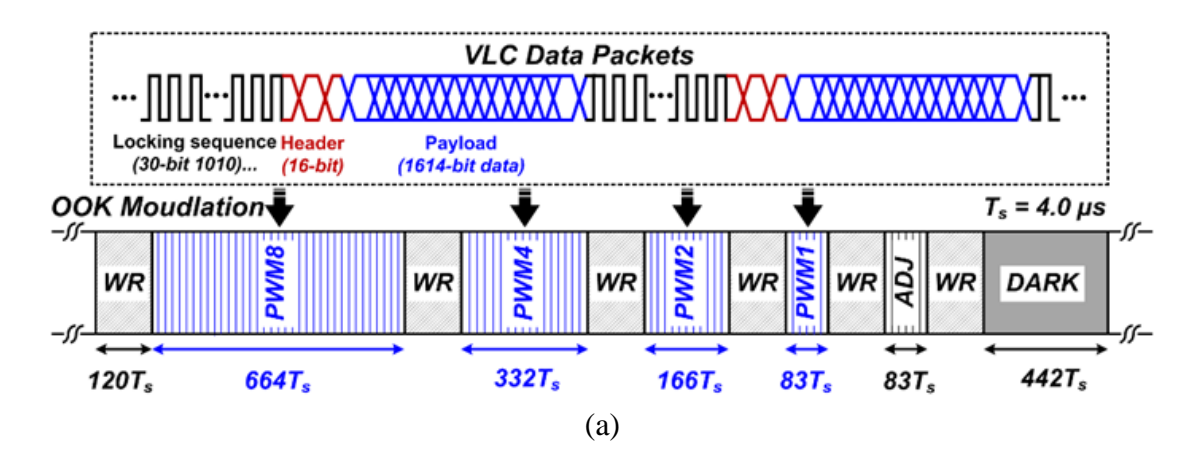
Depending on the materials used, there are two types of LEDs: OLEDs and inorganic LEDs. In general, the OLED drivers composed of thin-film transistors (TFTs) on polysilicon or amorphous silicon substrates suffer relatively large spatial/temporal variations of device threshold voltage [81]-[84]. Considering the feasibility of integrating them with more reliable CMOS drivers to overcome this issue, inorganic μLEDs can potentially be used for future advanced micro-displays. Although the monolithic integration of LEDs and driver circuits is highly desirable for reducing cost and improving reliability [85], the ability to grow inorganic μLEDs on a silicon substrate with pre-fabricated driver circuits is still an immature technology and requires further research and development. In particular, the circuits fabricated on silicon substrate cannot endure any high temperature processes near 1000 °C, which is typically used during MOCVD. Thus, the integration of inorganic μLEDs with CMOS silicon drivers using flip-chip bonding is currently more feasible.

As the infrastructure of the information society, IoT is enabling a more intelligent world. It consists of devices, buildings and other physical items integrated with electronics, sensors and software to collect and exchange data. With the potential to be embedded in portable devices, LED micro-displays can also be merged into the futuristic IoT as a smart device using VLC technology, as we propose for the first time. The advantage of this solution is that portable

devices with smart micro-displays, such as a smart watch, can directly transmit data to another device equipped with a VLC receiver, which can the built-in camera on a mobile phone. Due to the light-of-sight characteristic of VLC, the communication security can be enhanced. The solution is also applicable to large-scale LED display, such as OLED TV, to provide extra information for audiences (e.g., the background introduction of a video) and real-time download services. However, there exist difficulties for implementing simultaneous display and VLC on varying images with different brightness. In the case that the images are in very low brightness, the transmitted VLC signal will be too weak to be received. To deal with this problem, a possible way is to deactivate VLC transmission when a specific image is estimated to be unsuitable for communication purposes. Since the typical frame rate for display is smaller than 100 frames per second (fps), real-time estimation of each image is feasible, which can be done by software.

This chapter elaborates the design and characterization of the first active matrix LED (AMLED) micro-display with an embedded VLC transmitter [86]. To achieve simultaneous display and VLC functions, a control scheme, namely PWM superimposed with OOK modulation is proposed. At the circuit level, a pixel driver cell consisting of three transistors and one capacitor (3T1C) with a novel VLC function is employed to implement the control scheme. Implemented in a 0.5- µm 2P3M CMOS process, the driver SoC drives a wide quarter-VGA (WQVGA) display featuring 400×240 pixels of 30×30 µm² blue gallium nitride (GaN) µLEDs, and simultaneously supports VLC at a data rate of 1.25 Mb/s, enabling LED digital signage for location-based applications such as information broadcasters and indoor positioning beacons. Moreover, flip-chip technology is adopted to bond the driver SoC with the µLED array.

3.2 Proposed Control Scheme



| PWM8 | PWM4 | PWM2 | PWM1 | Grayscale | |
|------|------|------|------|-----------|--|
| | | | | 15 | |
| | | | | 8 | |
| | | | | 4 | |
| | | | | 2 | |
| | | | | 1 | |
| | | | | 0 | |
| (b) | | | | | |

Fig. 3.1 (a) 4-bit binary-weighted PWM frame structure and predefined VLC data packet, and (b) illustration of grayscale control.

A 4-bit binary-weighted PWM frame structure is employed to control the grayscale of each pixel for display. PWM is employed because it can be implemented using digital clock and digital counter, which is more robust compared to the other modulation schemes. In addition, OOK modulation is superimposed on the PWM control to accomplish the VLC function without interfering with the display.

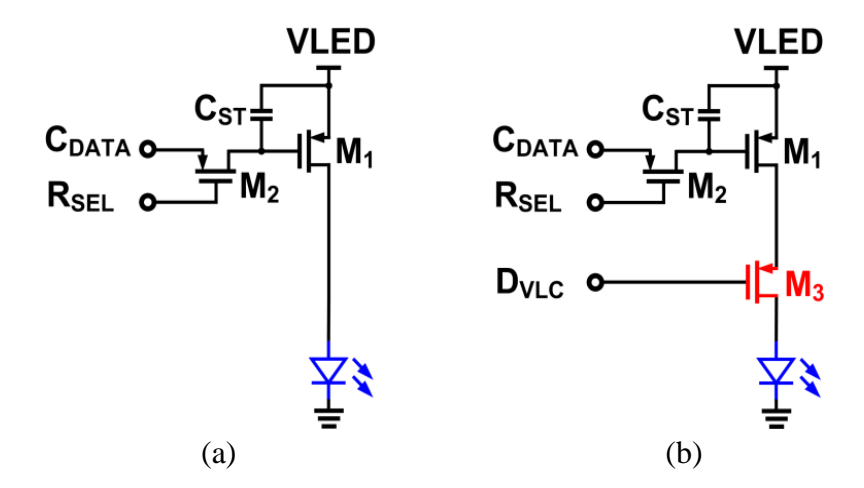
As illustrated in Fig. 3.1 (a), each 4-bit PWM frame is divided into four binary-weighted display sub-frames (PWM8/4/2/I). In other words, the length of the consecutive display sub-frames is scaled by a factor of 2. Fig. 3.1 (b) shows how specific grayscales are generated by different combinations of these four display sub-frames. For example, a μ LED pixel is only turned on in PWM8, and turned off during the other display sub-frames to generate a grayscale of 8. The interval between two adjacent display sub-frames, WR, is set by the required time to input the display data into the AMLED driver. Assuming the programming time of each row in the driver is T_S , then $WR = 120 \ T_S$ is needed to update 120 rows with new display data. To compensate for the brightness difference among μ LED pixels due to process variations, an adjustable sub-frame, ADJ, is configured to implement calibration with standard pattern images at a resolution of $1/83 \times PWM1$. Since the ADJ sub-frame length is equivalent to 1/15 of the

total length of all the display sub-frames PWM8/4/2/1 (same as PWM1), it can correct for up to $\pm 7\%$ (± 1 LSB) of non-uniformity in the μ LED pixel output brightness. Moreover, a dark sub-frame, DARK, is appended at the end of each PWM frame to improve the display contrast ratio. The overall frame length, including 5 WRs, PWM8/4/2/1, ADJ and DARK, is 10 ms, achieving a 100-Hz frame rate.

In the display-only scenario, the illuminated pixels are fully turned on during each display subframe. In contrast, when simultaneous VLC is enabled, the illuminated pixels are OOK modulated at a sufficiently high frequency to avoid any flickering observable by the human eye. In our system, the modulated VLC bit rate is set to be 5 Mb/s. To establish a reliable communication link, the transmitted VLC data is predefined in a packet format of a 30-bit locking sequence of '1010...', and a 16-bit data header, followed by the payload data with a length of 1614 bits (Fig. 3.1 (a)). There are 8, 4, 2 and 1 VLC data packets in *PWM8/4/2/1*, respectively. Due to the employment of Manchester encoding, where logic transitions instead of logic levels are utilized to deliver information, the only effect of OOK VLC modulation on each PWM frame is that the average illumination is degraded by 50%.

3.3 Proposed Pixel Driver Array

Fig. 3.2 (a) shows the structure of a basic two transistors and one capacitor (2T1C) pixel driver cell for display [81], consisting of a driving transistor M_1 to drive the μ LED pixel, a switching transistor M_2 to control the programming of the driver via R_{SEL} , and a capacitor C_{ST} to store the display information from C_{DATA} .



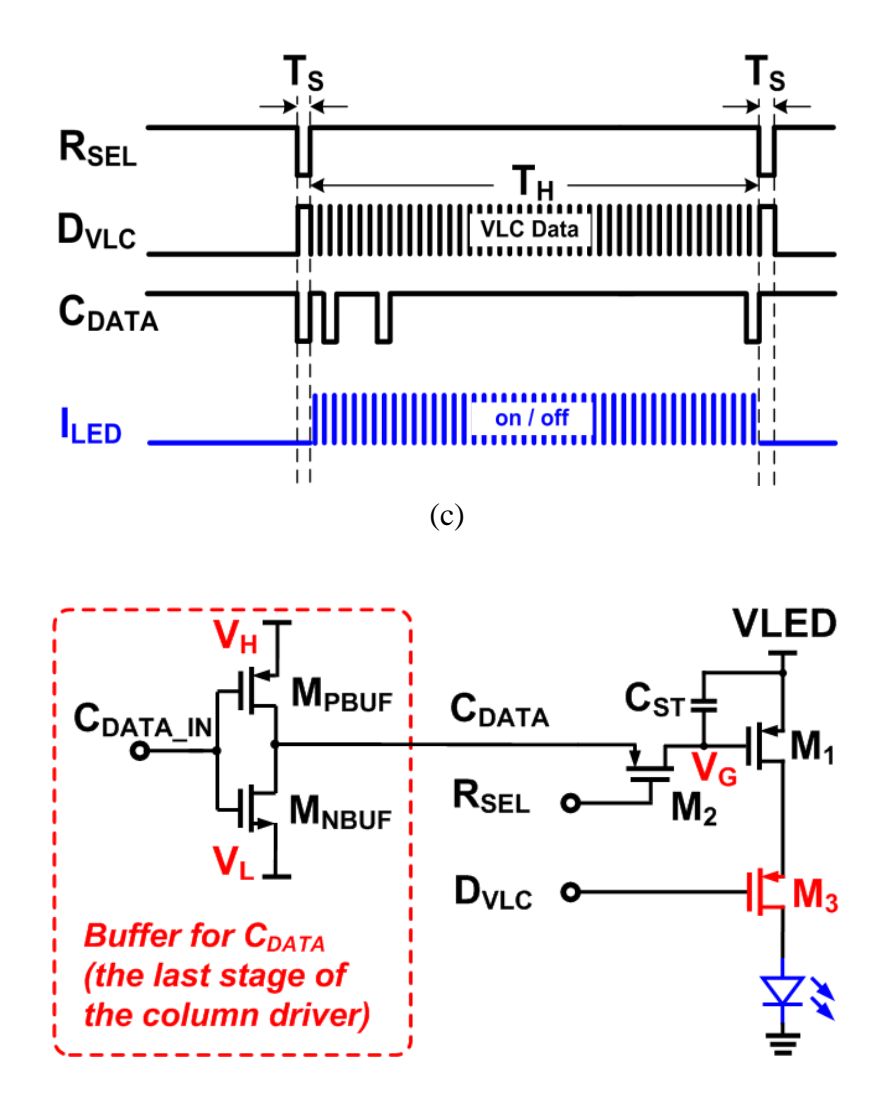


Fig. 3.2 (a) Basic 2T1C pixel driver cell for display only, (b) the 3T1C pixel driver cell with a novel VLC function, (c) operation timing of the 3T1C pixel driver cell, and (d) the 3T1C pixel driver cell connected to an input buffer for C_{DATA} .

(d)

Different from the traditional pixel driver cells for display-only purpose, a 3T1C pixel driver cell with a novel VLC function is employed to support display and VLC simultaneously, as shown in Fig. 3.2 (b). Developed from the basic 2T1C structure, an additional transistor, M_3 , acting as a switch, is inserted between M_1 and the μ LED pixel to provide VLC control. The 3T1C driver cell alternately operates in sampling (T_8) and holding (T_8) periods, as illustrated in Fig. 3.2 (c). During the sampling period, T_8 is applied with logic 0 to turn on T_8 and the display data is written into T_8 from T_8 while T_8 while T_8 holds logic 1 and thus there is no current flowing into the T_8 pixel through T_8 . In the holding period, T_8 is applied with logic 1 to turn off T_8 , and T_8 is modulated by a high-speed VLC signal, T_8 by T_8 to switch on

and off the µLED pixel. Since the GaN µLED array has a shared cathode, only PMOS transistors are adopted in the pixel driver cell, which also eliminates the need for ground routing.

Fig. 3.2 (d) depicts a 3T1C pixel driver cell connected to an input buffer consisting of transistor M_{NBUF} and M_{PBUF} for C_{DATA} , where V_H and V_L are the power-supply rails of the buffer used to define the voltage swing at the gate of M_2 . Usually V_H is the same as VLED, while V_L is set based on the required current of the μ LED. Several design considerations need to be taken care of on this circuit, as explained below.

(1) Constant-current driving scheme for the μ LED. In the constant-current driving scheme, M_1 is biased in saturation region as a voltage controlled current source, the turn-on current of the μ LED is expressed as follows for long-channel MOS transistors by ignoring channel-length modulation effect.

$$I_{\mu \text{LED}} = \frac{1}{2} \mu_p C_{ox} \frac{W_1}{L_1} (VLED - V_G - |V_{THP}|)^2 = \frac{1}{2} \mu_p C_{ox} \frac{W_1}{L_1} (VLED - V_L - |V_{THP}|)^2$$
 (3.1)

where μ_p , C_{ox} and V_{THP} are the mobility of holes, the transistor gate oxide capacitance per unit area and the PMOS threshold voltage, respectively. While W_I , L_I and V_G are the width, the channel length and the gate voltage of M_I , respectively. Since V_{SDI} , which is the source-drain voltage drop of M_I , should be larger than $(VLED - V_G - |V_{THP}|)$ to guarantee M_I to be in the saturation region, one strategy in the design is to enlarge the ratio of $\frac{W_I}{L_I}$ so that $(VLED - V_G - |V_{THP}|)$ and thus V_{SDI} can be minimized to reduce the power consumption of M_I . However, in the case that the leakage current at the gate of M_I is too large to affect the voltage kept by capacitor C_{ST} , then the ratio of $\frac{W_I}{L_I}$ should be reasonable to ensure a large enough source-gate voltage of M_I to maintain the current of the μ LED, while the trade-off is that V_{SDI} and thus the power consumption of M_I will increase.

(2) Constant-voltage driving scheme for the μ LED. In the constant-voltage driving scheme, M_1 is biased in the linear region as a voltage controlled resistor (or switch), which can be achieved by simply connecting V_L to ground, then the power consumption of M_1 when the μ LED is turned on can be minimized by increasing the ratio of $\frac{W_1}{L_1}$. Since the voltage swing of V_G is maximized, the circuit is also robust to leakage current at the gate of M_1 . Another advantage of this driving scheme is the low complexity for implementation. The only drawback is that the μ LED current is controlled by VLED instead of being defined by a constant current source.

(3) In the implementation of a large-scale active matrix driver consisting of the 3T1C pixel driver units, R_{SEL} is connected to a row scanning signal with a frequency of f_{RSEL} , then the following timing constraints have to be fulfilled:

$$\frac{1}{f_{RSEL}} > \frac{c_{ST}(V_H - V_L)}{I_{charge}} = \frac{c_{ST}(V_H - V_L)}{\frac{V_H - V_L}{r_{on\ MNBUF} + r_{on\ M2}}} = C_{ST}(r_{on\ MNBUF} + r_{on\ M2})$$
(3.2a)

$$\frac{1}{f_{RSEL}} > \frac{c_{ST}(V_H - V_L)}{I_{discharge}} = \frac{c_{ST}(V_H - V_L)}{\frac{V_H - V_L}{r_{on_MPBUF} + r_{on_M2}}} = C_{ST}(r_{on_MPBUF} + r_{on_M2})$$
(3.2b)

where I_{charge} and $I_{discharge}$ are the charging and discharging current of C_{ST} to change the stored voltage V_G between V_H and V_L , respectively, while r_{on_MNBUF} , r_{on_MPBUF} and r_{on_M2} are the equivalent turn-on resistance of M_{NBUF} , M_{PBUF} and M_2 , respectively. In (3.2a) and (3.2b), all the equivalent turn-on resistances are assumed to be constant to simplify the analysis. In reality, they will change according to terminal voltages. Both (3.2a) and (3.2b) can be re-written as follows to provide guidance when sizing M_{NBUF} , M_{PBUF} and M_2 .

$$r_{on_MNBUF} + r_{on_M2} < \frac{1}{f_{RSEL}c_{ST}}$$
(3.3a)

$$r_{on_MPBUF} + r_{on_M2} < \frac{1}{f_{RSEL}c_{ST}}$$
 (3.3b)

Based on the 3T1C pixel driver cell, an AMLED driver is constructed. Fig. 3.3 illustrates the schematic and operation timing of the driver. To reduce the required driving capability of row/column lines, the pixel driver array is divided into four identical macro-cells (A-D), each with an array size of 200×120 . Inside every macro-cell, C_{DATA} is the common data line for each column, while R_{SEL} is the shared selection line for each row. To modulate the entire macro-cell with the input VLC data, a global signal, D_{VLC} , is employed to concurrently control the gates of all M_3 . The updating of the display data into the macro-cells is achieved via row-by-row progressive scanning.

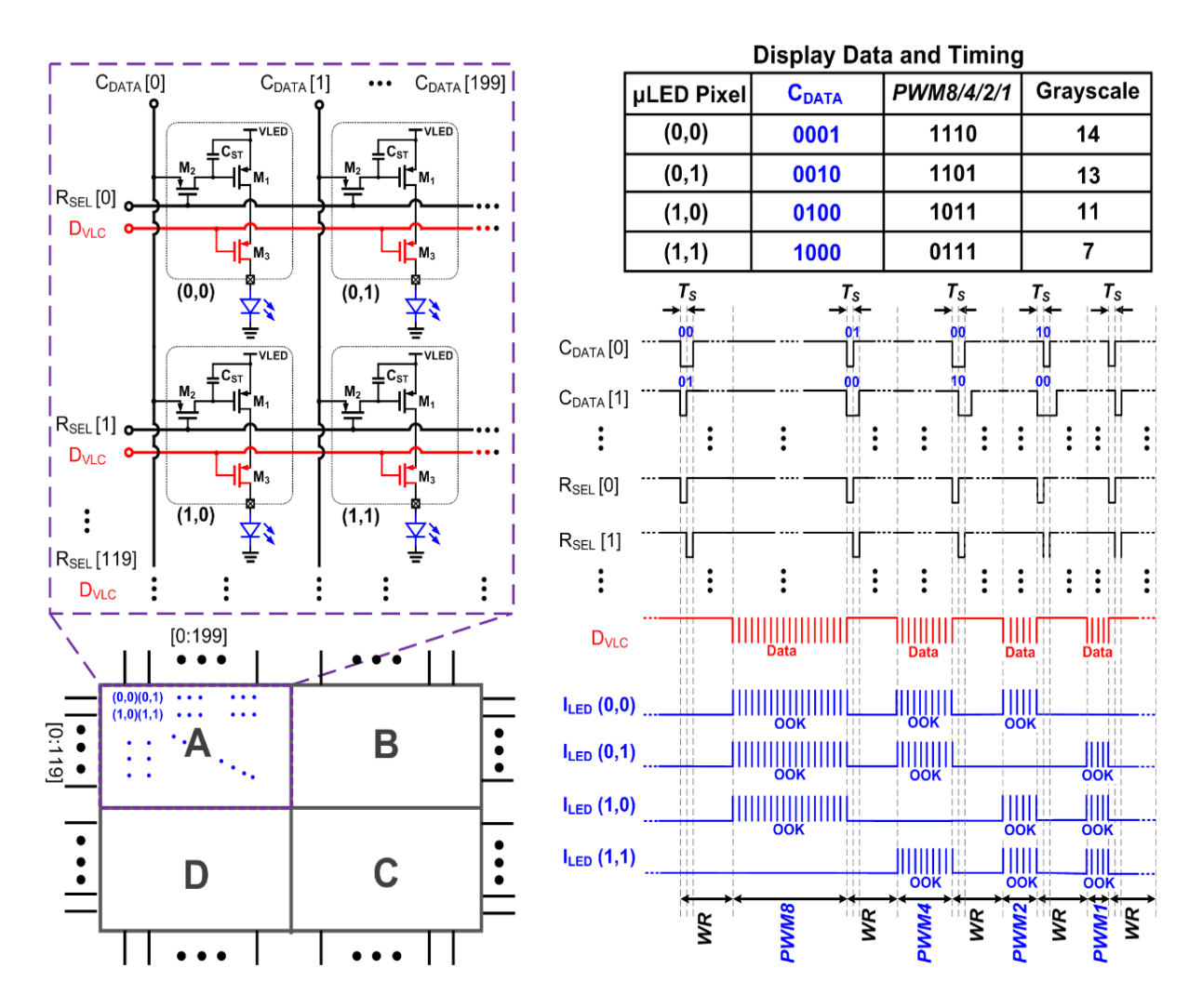


Fig. 3.3 Schematic of the AMLED driver and the timing diagram to achieve specific grayscales on four μLED pixels using progressive scanning.

The operation timing of the pixel driver array is elaborated with a case to achieve specific grayscales on four individual μ LED pixels, as shown in the table in Fig. 3.3. For example, to have a grayscale of 13 on μ LED pixel (0,1), which is the first pixel in the second column, the C_{DATA} to be sent to this pixel for PWM8/4/2/1 should be 0, 0, 1 and 0, respectively. During each WR interval of the 4-bit PWM frame, the selection line of the first row $R_{SEL}[0]$ is activated to turn on all M_2 in that row when the first 200-bit display data coming from the column driver $(C_{DATA}[0], C_{DATA}[1], ..., C_{DATA}[199])$ is ready, and the display data is written and stored in the capacitor C_{ST} until the sampling period for the next display sub-frame. In this case, both $C_{DATA}[0]$ and $C_{DATA}[1]$ are 0 for WR of PWM8. $R_{SEL}[0]$ is then de-activated, and another set of 200-bit display data is available for the next row with a time interval of $T_S = 4$ μ s. Here $C_{DATA}[0] = 0$ and $C_{DATA}[1] = 1$ for the second row. After the entire WR period of 480 μ s (4 μ s/row ×

120 rows) for *PWM8*, the corresponding data stored in the capacitor C_{ST} of the four μLED pixels (0,0), (0,1), (1,0) and (1,1) are 0, 0, 0 and 1, respectively, and the VLC mode is then enabled to implement OOK modulation through D_{VLC} . A similar process is repeated for PWM4/2/1 and the desired grayscales are eventually achieved on the four μLED pixels.

Since VLC is only allowed during display sub-frames *PWM8/4/2/1*, a memory block is needed to store VLC data for the rest of the frame, i.e., the *WR*, *ADJ* and *DARK* sub-frames.

3.4 Proposed System Architecture

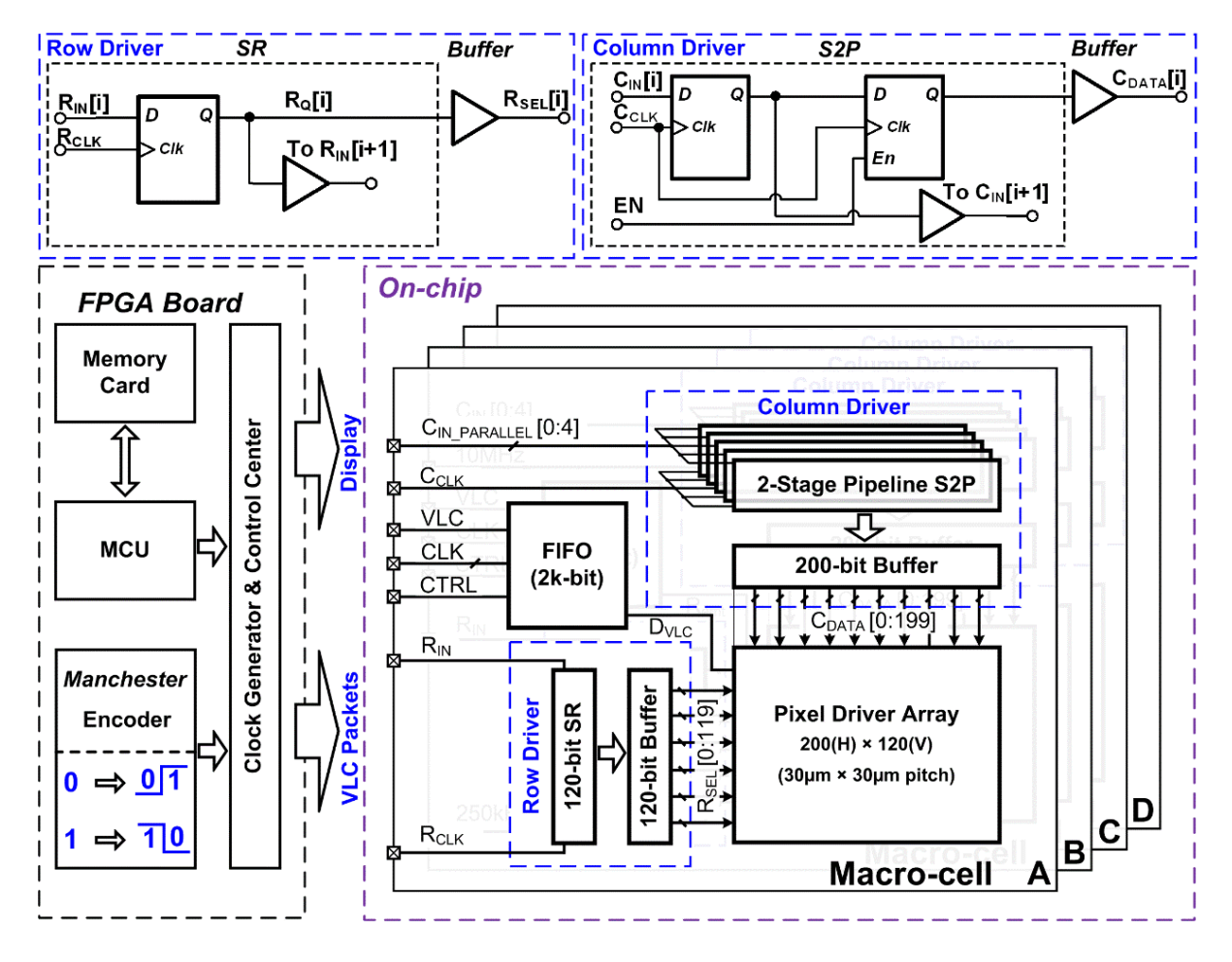
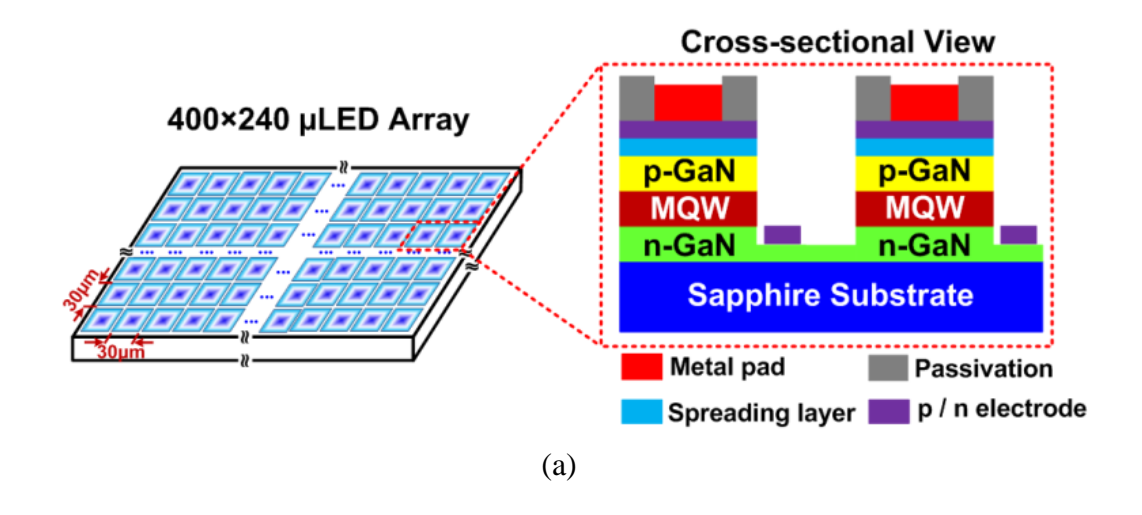


Fig. 3.4 System architecture and implementation of the proposed AMLED micro-display driver SoC.

Fig. 3.4 depicts the system architecture and implementation of the proposed AMLED micro-display driver SoC for a $400\times240~\mu$ LED array. There are four identical macro-cells (A-D) implemented on chip, each containing a pixel driver array with a size of 200×120 , a row driver,

a column driver and a first-in first-out (FIFO) memory. The 120-bit shift register (SR) clocked at 250 kHz (= $1/T_S$) in the row driver is used to generate row selection signals (R_{SEL}[0:119]) for progressive scanning by forwarding the output of the stage i (R₀[i]) to the input of the stage i+1 (R_{IN}[i+1]). A 120-bit buffer is cascaded with the row SR to improve the driving capability. The column driver involves five parallel 40-bit blocks to perform serial-to-parallel (S2P) conversion, and a 200-bit buffer. The frequency of the column driver clock C_{CLK} is 10 MHz in order to maintain the required frame rate, while the write-enabling signal EN is triggered every 4 µs during WR period to parallelly load display data into the pixel driver cells in the same row. As mentioned above, a 2k-bit asynchronous FIFO is implemented to store VLC data. An FPGA board integrating a memory card reader and a micro-controller unit (MCU) is designed to control display and to process VLC data. The basic operation of the driver SoC is as follows. First of all, the image to be displayed needs to be converted to have a resolution of 400×240 with 4-bit grayscale and stored in the memory card. The MCU then reads out the display data, and writes it into the column driver. Under the aforementioned progressive scanning control (Fig. 3.3), the display data held in the driver array is refreshed row by row. After a complete WR period, the entire driver array is updated with the desired data and the image is displayed on the µLED array accordingly. At the same time, the data to be transmitted through VLC is encoded by the Manchester encoder, and then forwarded to the input of the FIFO, of which the output is connected to D_{VLC} to modulate the µLED array. In the Manchester encoder, a transition from 0 to 1 represents data 0 and a transition from 1 to 0 represents data 1, such that constant DC level of the µLED array is attained.

3.5 µLED Array and Flip-Chip Bonding



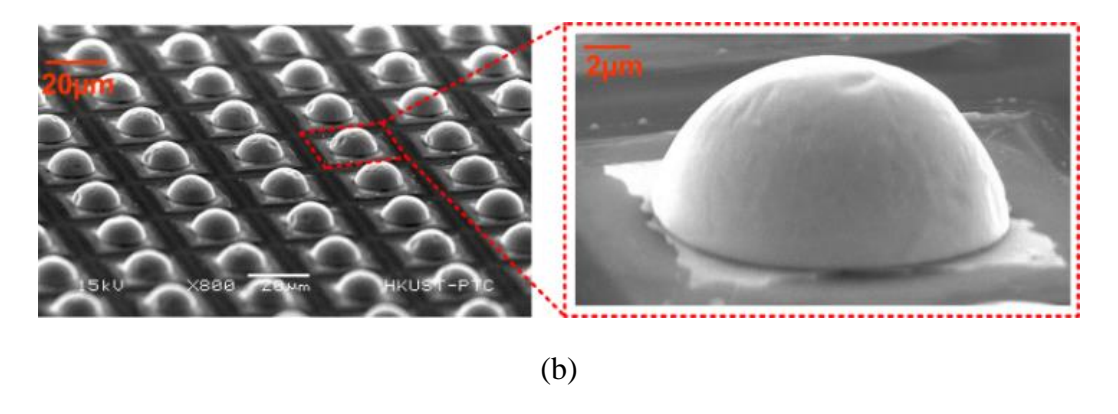


Fig. 3.5 (a) Structure of the 400×240 GaN µLED array, and (b) an SEM image of indium bumps generated after the reflow process for flip-chip bonding.

The blue GaN μ LED array featuring 400×240 pixels with a pixel size of 30×30 μ m² was implemented on a single sapphire substrate using LED fabrication process mentioned in [77], where the μ LED array pattern was defined using plasma enhanced chemical vapor deposited (PECVD) oxide and was transferred to GaN epi-layers through inductively coupled plasma (ICP). By employing a bottom-emission structure with a flip-chip configuration, light is generated from the μ LED array and is emitted through the transparent sapphire substrate. Fig. 3.5 (a) shows the structure of the μ LED array, including n-type GaN (n-GaN), multiple quantum well (MQW), p-type GaN (p-GaN), current spreading layer and SiO₂ passivation. The interface between the μ LED array and the AMLED driver is the flip-chip bonding pads on top of the individually controllable p-electrodes. The whole μ LED array shares common n-electrodes connected to ground.

The flip-chip bonding was conducted with the following steps. First of all, indium plates were formed on the metal pads of the μ LED array. Then the μ LED array was treated at 240 °C to reflow all indium plates to become indium balls. Finally the μ LED array was flip-chip bonded to the CMOS driver SoC via thermal compression bonding at 180 °C with a pressure of 20 Newtons. A scanned electron microscope (SEM) image of the indium bumps generated after the reflow process for flip-chip bonding is presented in Fig. 3.5 (b). It can be observed that the indium bumps with a diameter of 14 μ m are in good uniformity in dimensions, which is essential to establish physically and electrically reliable connections between the GaN μ LED array and the CMOS AMLED driver SoC.

3.6 Experimental Results

The AMLED micro-display driver SoC was implemented in a 0.5-µm 2P3M CMOS process, while the GaN µLED array fabricated at the Nanoelectronics Fabrication Facility of HKUST.

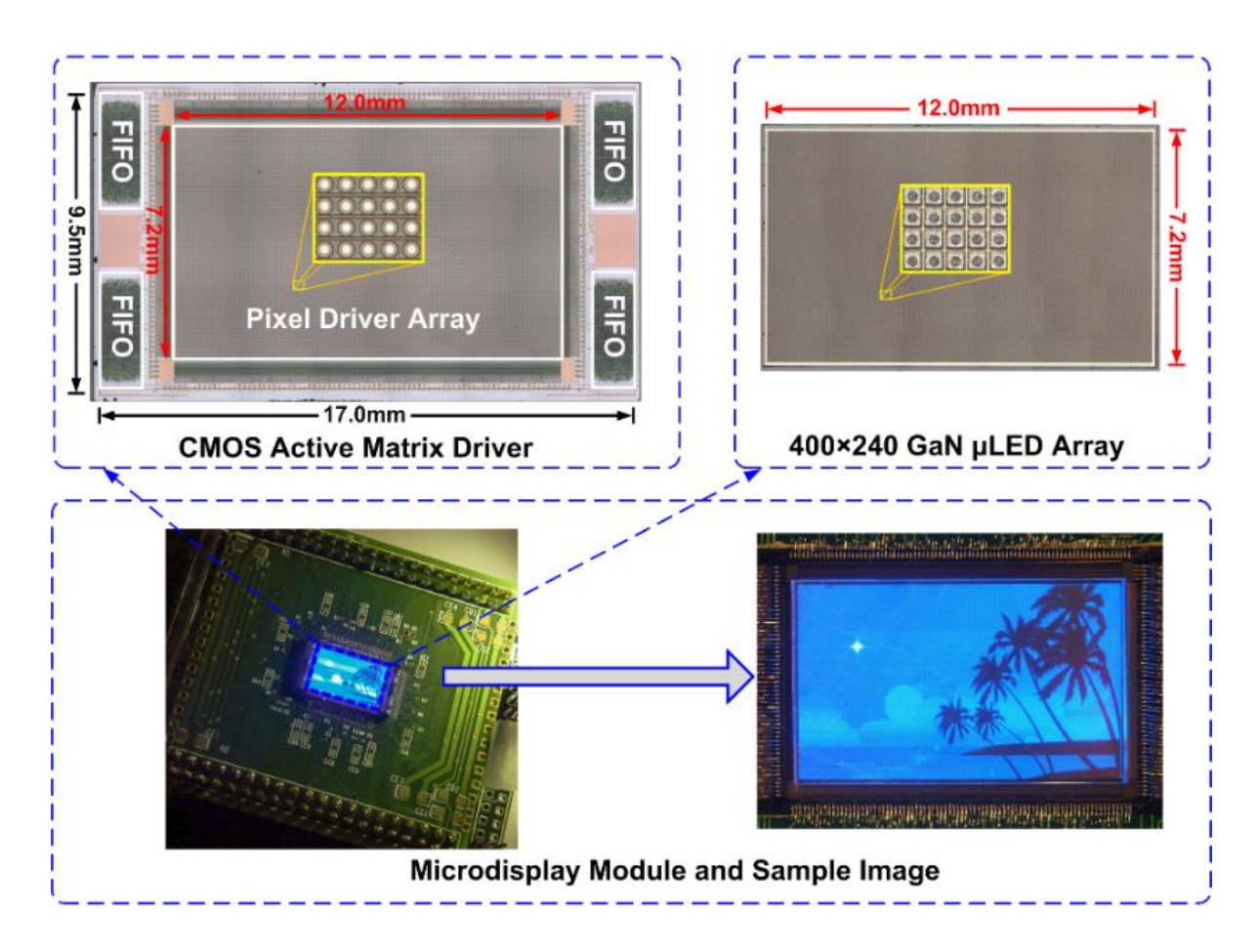


Fig. 3.6 Photographs of the CMOS AMLED driver SoC, the 400×240 GaN μLED array and the entire micro-display module with a sample image.

The photographs of the CMOS driver SoC, the 400×240 GaN μ LED array and the entire microdisplay module with a sample image are shown in Fig. 3.6. The total area of the SoC is 17.0×9.5 mm², with 12.0×7.2 mm² for the active matrix driver. Powered by a 5-V supply, the microdisplay module consumes 1.17W.

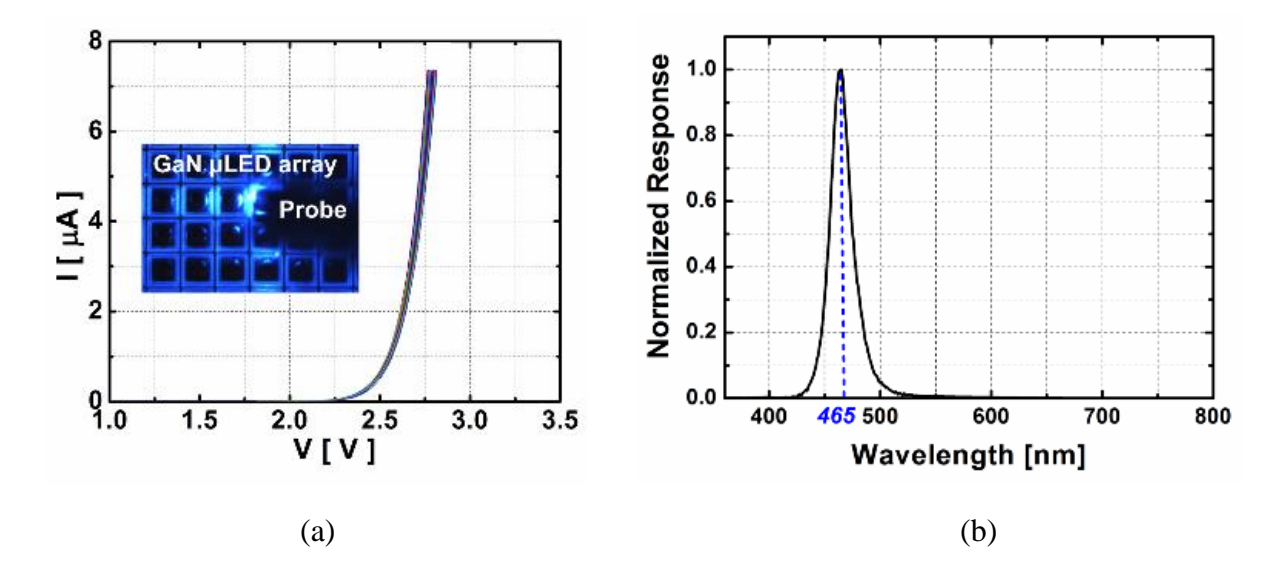


Fig. 3.7 (a) Measured I-V characteristics of 40 randomly selected μLED pixels with an inset photo showing the direct probing of one μLED pixel for I-V measurements, and (b) optical emission spectrum of the μLED pixels.

40 μ LED pixels were selected in random and the I-V characteristics were measured and plotted in Fig. 3.7 (a), which indicate an on-voltage variation of $\pm 0.2\%$ at a bias current of 5μ A, demonstrating the good uniformity. The inset is a μ LED array under testing with a DC probe. Fig. 3.7 (b) shows the optical emission spectrum of the μ LED pixels with a peak emission wavelength of ~465 nm.

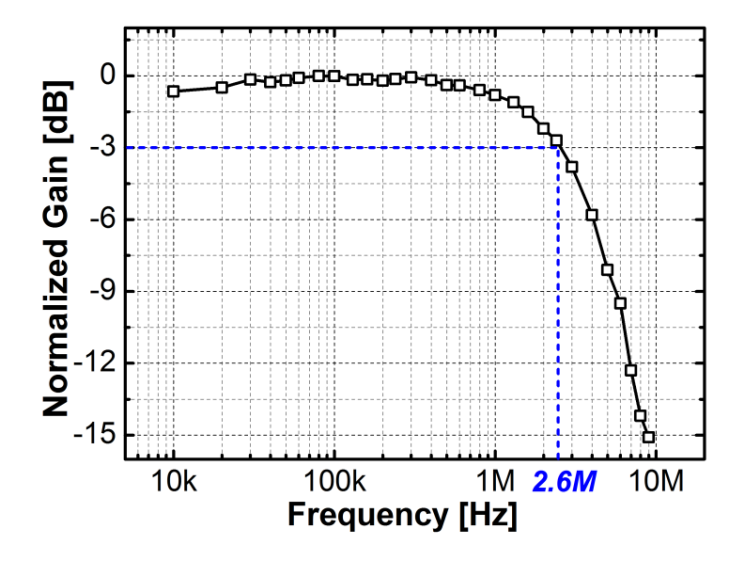


Fig. 3.8 Measured optical frequency response of the micro-display module, including the AMLED driver SoC and the μLED array.

By sweeping the VLC modulation frequency and receiving the signal by a photo-receiver (New Focus 1801-FC) with 125-MHz bandwidth (BW), the optical frequency response of the microdisplay module (including the AMLED driver SoC and the μ LED array) was obtained. Fig. 3.8 shows that the -3dB BW of the module is 2.6 MHz, which is sufficient to support OOK VLC modulation at 5 Mb/s.

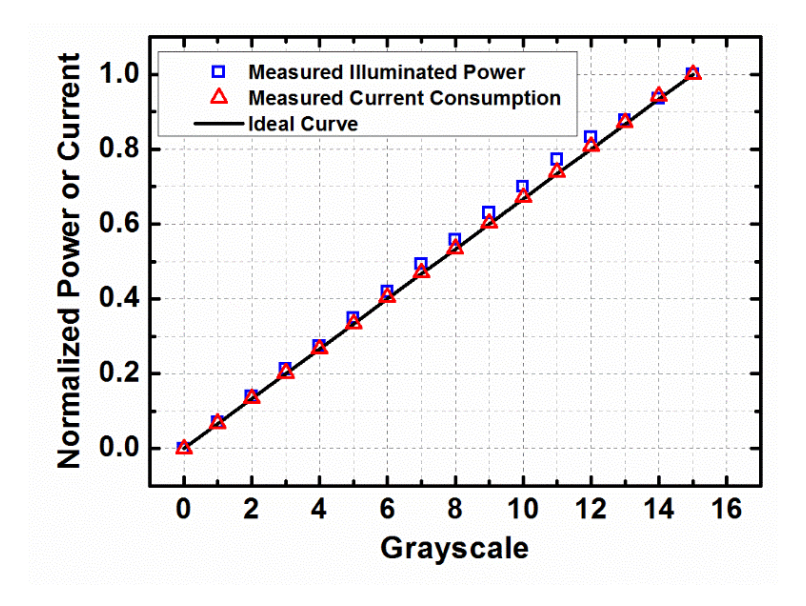


Fig. 3.9 Measured illuminated power and current consumption of the µLED array under 16 different grayscale settings with all pixels active.

The normalized illuminated power of the µLED array as a function of grayscale settings was measured by a photo-detector (PD) (Newport 818) with an active area of 1-cm². Besides this, the corresponding current consumption was also recorded. As depicted in Fig. 3.9, under 5-Mb/s VLC modulation, the maximum differential non-linearity (DNL) and the maximum integral non-linearity (INL) of the illuminated power are 0.36 and 0.63 LSB, respectively; while from current consumption measurements at the same modulation speed, the DNL and INL are both 0.12 LSB, which implies about 1% of non-linearity. The difference between these two sets of obtained non-linearity values is mainly because the illuminated power is measured indirectly and optically, whereas the current consumption is based on direct electrical measurement. Thus, the latter one is more accurate.

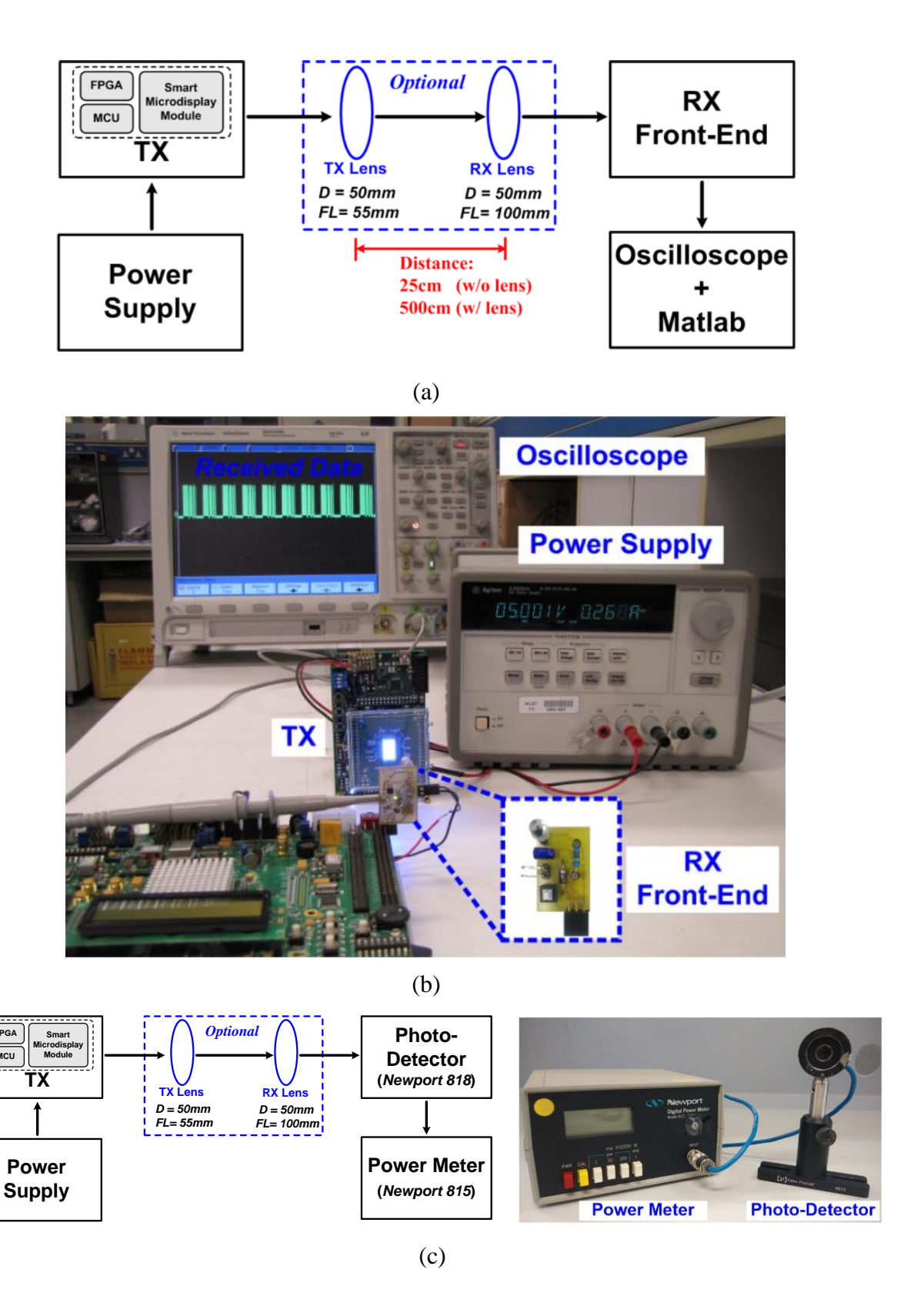
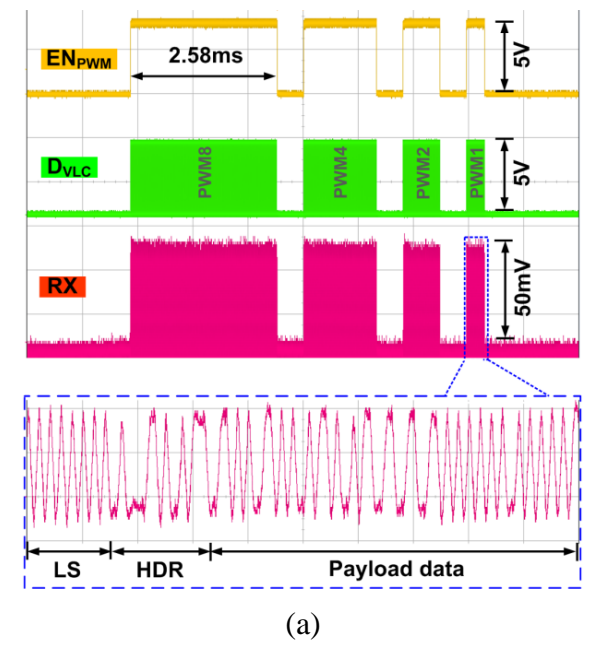


Fig. 3.10 (a) Diagram of the VLC experimental setup for the micro-display module, (b) the VLC link measurement setup without a lens, and (c) diagram of the illuminated power measurement setup with a photo showing the employed photo-detector and power meter.

To characterize the VLC performance of the micro-display module, an experimental setup was built, as shown in Fig. 3.10 (a), including a power supply (Agilent E3632A), a micro-display module as the transmitter (TX), and a receiver (RX) frond-end with $100\text{-dB}\Omega$ trans-impedance gain and 4.6-MHz BW. An oscilloscope (Agilent MSO7034B) is employed to sample the received VLC signal for Matlab to implement demodulation and decoding. VLC measurements are performed both with and without optical lenses. The TX lens used is 50 mm in diameter (D), with a focal length (FL) of 55 mm. While for the RX lens, D and FL are 50 mm and 100 mm, respectively. Fig. 3.10 (b) shows a photograph of the VLC link measurement setup without a lens. The illuminated power of the micro-display module is measured with a setup illustrated in Fig. 3.10 (c), where a photo-detector and a power meter are employed on the receiver side instead.

Fig. 3.11 presents the measured VLC waveforms under 5-Mb/s VLC modulation at different communication distances with 50% of the μ LED pixels turned on. In Fig. 3.11 (a), when VLC enabling signal EN_{PWM} is asserted, a high-frequency VLC signal D_{VLC} appears to modulate the μ LED array on the transmitter side; on the receiver side, the output of the RX front-end exactly follows the predefined format of the VLC data packet. Fig. 3.11 (b) is the received eye diagram at 20-cm distance without a lens, of which the height is 38 mV. With the use of TX and RX lenses (Fig. 3.10 (a)), the received eye diagram at 500-cm distance is even better than that at 20-cm distance without a lens, as shown in Fig. 3.11 (c). All the eye diagrams in Fig. 3.11 were plotted on Matlab based on the data collected from the oscilloscope (Fig. 3.10).



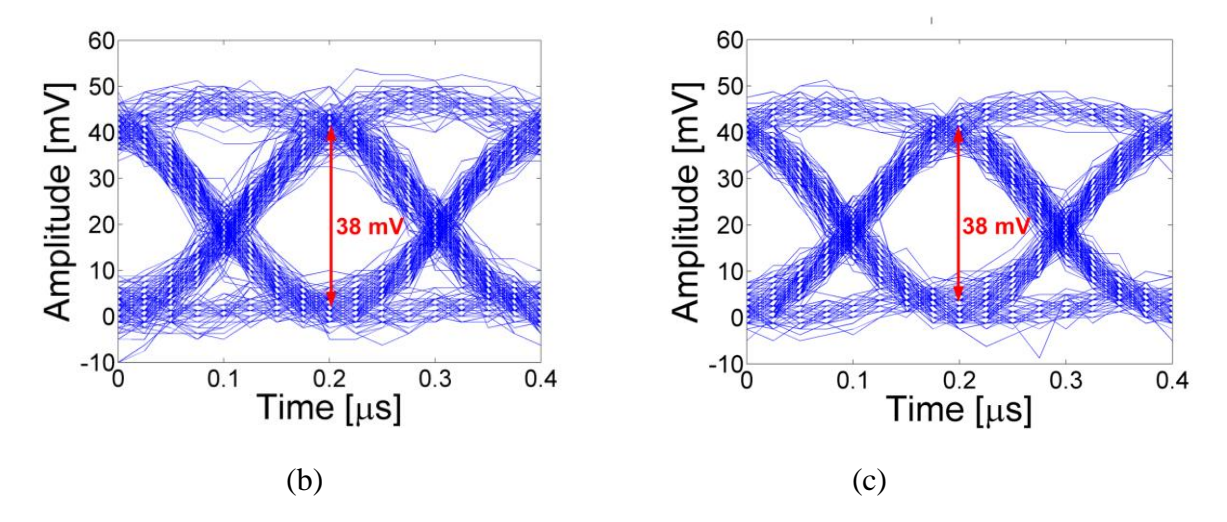


Fig. 3.11 (a) Measured waveforms of the VLC enabling signal (EN_{PWM}), the VLC modulation signal (D_{VLC}), and the received VLC signal from the RX front-end at 20-cm distance without a lens, (b) eye diagram of the received VLC signal at 20-cm distance without a lens, and (c) eye diagram of the received VLC signal at 500-cm distance with TX and RX lenses.

Fig. 3.12 depicts the measured bit error rate (BER) and the received optical power for two different images at different distances. The original images are also provided to verify the display function. With a 5-Mb/s modulated VLC signal, the maximum effective data rate is 1.25 Mb/s since only half of the 4-bit PWM frame, i.e., PWM8/4/2/1, is available for VLC, and Manchester encoding is employed. For a BER <10⁻⁵ without a lens, the VLC distance is up to 25 cm and the corresponding received power is ~2 μ W.

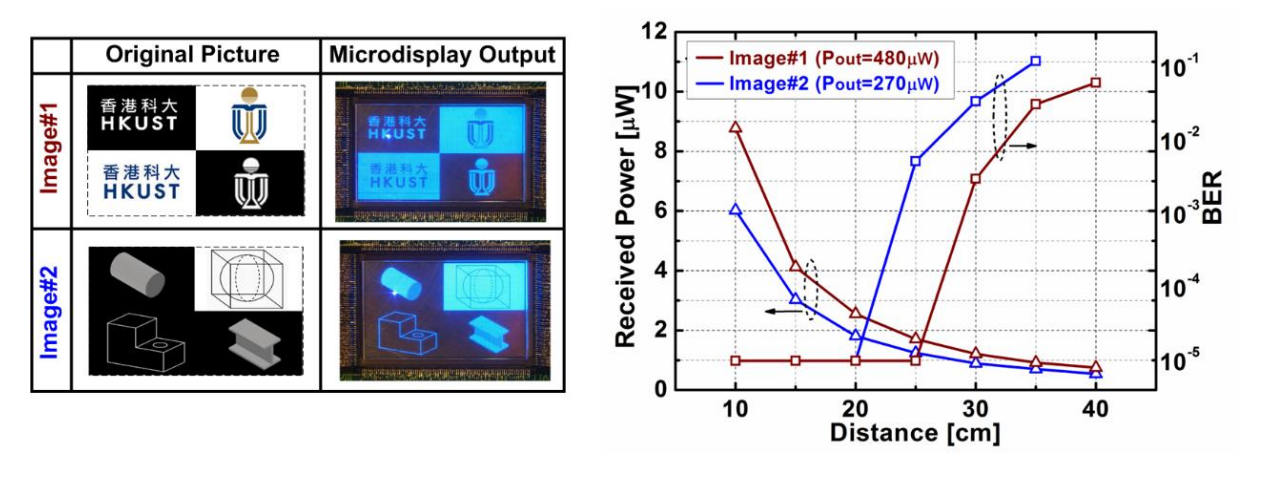


Fig. 3.12 Measured received power and BER with an effective data rate of 1.25 Mb/s versus distance for image#1 and image#2, respectively.

It can be observed that different display images with different transmitted optical power may affect the communication performance. In general, for any communication system such as WiFi, communication will be ceased when the received power is too weak to maintain a certain BER. Similarly, when the output optical power of a display image is too small, the communication performance of the micro-display system will be significantly deteriorated. Therefore, a potential solution is that the controller on the transmitter side needs to estimate the optical power of the display image using grayscale information. When it is found that the optical power will be too weak to support communication, then no VLC data will be transmitted.

Table 3.1 summarizes the performance of the microdisplay module.

Table 3.1 Performance Summary and Comparison

| - | | | | |
|---------|-------------------------------|------------------|--------------------|---------------------------|
| | | [40] | [36] | This Work |
| | Resolution | 16×16 | 1×1 | 400×240 |
| | Pixel Pitch [µm²] | 100×100 | 50×50 | 30×30 |
| Display | Active Area [mm²] | 1.6×1.6 | 0.05×0.05 | 12.0×7.2 |
| | Peak Emission Wavelength [nm] | 550-600 | ~450 | ~465 |
| | Grayscale | 1-bit | 1-bit | 4-bit |
| | Frame Rate [HZ] | N/A | N/A | 100 |
| | Pixel DC Current [A] | 0.1m-80m | 40m | 1.3 µ a |
| | Max. Pout [mW] | N/A | 4.5 | 0.9 b |
| VLC | Modulation | OOK | OFDM | ООК |
| | Bandwidth [MHz] | 100 | 60 | 2.6 ° |
| | Data Rate [b/s] | 250M | 3.0G | 1.25M ^d |
| | Distance w/o lens [cm] | N/A | N/A | 25 |
| | Distance w/ lens [cm] | N/A | 5 | >500 |
| | RX Sensitivity [mW] | N/A | 4.5 w/ lens | ~0.002 w/o lens |
| System | Functionality | Display | VLC Only | Display |
| | | or VLC | | and VLC |

^a Average current at a grayscale of 15 corresponding on-current is ~5.2 μA.

^b Measured with 1-cm² PD, and limited by the PD area.

^c Limited by the CMOS driver.

^d Modulated VLC bit rate is 5 Mb/s.

CHAPTER 4 VLC Receiver

4.1 Design Considerations

The targeted receiver for a low-cost VLC system requires sufficient bandwidth with high-frequency gain boosting, wide dynamic range and the ability to reject interference due to ambient light. A detailed discussion is given below.

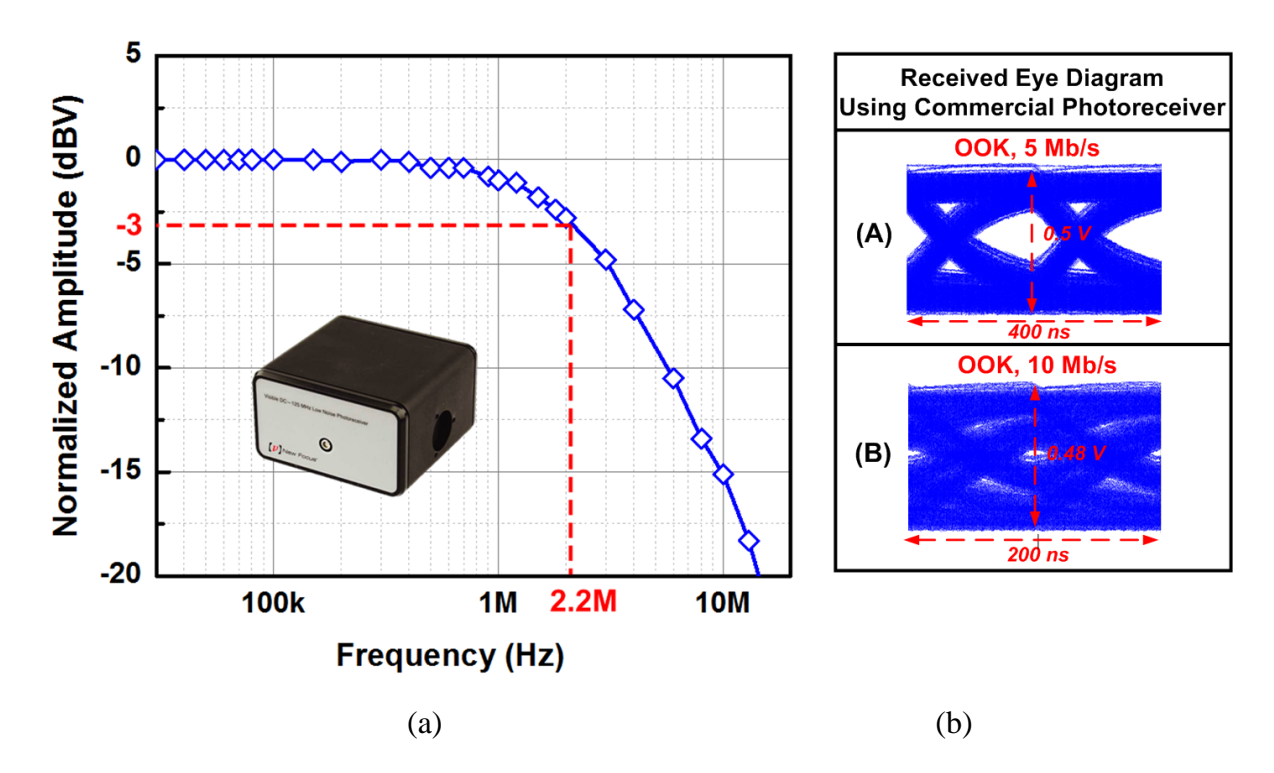


Fig. 4.1 (a) Normalized frequency response of a commercial phosphorescent white LED [87], which is measured using a commercial photoreceiver shown in the inset, and (b) received eye diagrams from the white LED using the commercial photoreceiver with PRBS-11 inputs.

(1) VLC provides free-space optical communication as an add-in function to general illumination systems. As one of the most important light sources, white LEDs are built mainly in two ways. The first way is using separate red (R), green (G) and blue (B) LED chips to generate white light. Although the modulation bandwidth of the involved single-color LEDs can reach beyond 10MHz [88], [89], it is costly to extensively deploy these RGB LED systems for general illumination. The other way is to employ blue or UV LEDs to activate specific phosphors and generate white light. This approach can reduce the cost and complexity of illumination systems, but results in a poor LED modulation bandwidth of only several MHz attributed to the slow response of phosphors, and thus VLC signals with frequencies higher

than that will decay and experience undesired intersymbol interference (ISI).

Fig. 4.1 (a) depicts the measured frequency response of a commercial phosphorescent white LED (Cree CLA1BWKW), showing a -3-dB bandwidth of about 2.2 MHz [87]. The inset is the wideband photoreceiver (New Focus 1801-FC) involved in the measurement, of which the bandwidth is beyond 100 MHz. Fig. 4.1 (b) is the received eye diagrams using the commercial photoreceiver with PRBS-11 inputs, where an eye with an opening of 0.25 V is observed at 5 Mb/s, but is totally closed at 10 Mb/s, confirming that the modulation bandwidth of the phosphorescent white LED is well below 5 MHz.

Blue filtering can be introduced to deal with this issue at the price of reduced received power (as explained in the next section) and extra optical components [89], [90], which is not suitable for low-cost applications. Alternatively, post-equalization techniques can be employed on the receiver side to improve the overall bandwidth of the system (including the transmitter and the receiver) to beyond the bandwidth limitation of white LEDs. Therefore, a VLC receiver with sufficient bandwidth and gain boosting at high frequencies is required to support high-speed communication.

- (2) Similar to conventional RF wireless systems, a wide dynamic range is required to accommodate different input signal amplitudes and communication distances. For example, when the input signal is too large, the gain of the receiver should be reduced to avoid saturation. In low-speed applications, the receiver gain can be increased to extend communication distance with a trade-off of smaller bandwidth.
- (3) As the VLC receiver needs to operate in various situations, including those with strong ambient light, the ability to reject these interferences is essential to avoid the circuit to be saturated [91]. In general, sunlight and un-modulated light sources induce DC photocurrents in a PD, while incandescent lamps and fluorescent lamps produce AC interferences at certain frequencies [32]. For example, under a normal office lighting condition with illumination of 500 lx [92], a common commercial PD can generate an ambient photocurrent as high as $42 \mu A$ [93]. Table 4.1 summarizes the recommended illumination levels for various venues.

Table 4.1 RECOMMENDED ILLUMINATION LEVELS FOR VARIOUS VENUES [92]

| Venue | Illumination (lux, lumen/m²) | |
|--|-------------------------------------|--|
| Warehouses, Homes, Theaters | 150 | |
| Normal Office, Study Library, Laboratories | 500 | |
| Supermarkets, Mechanical Workshops | 750 | |

4.2 Blue filtering

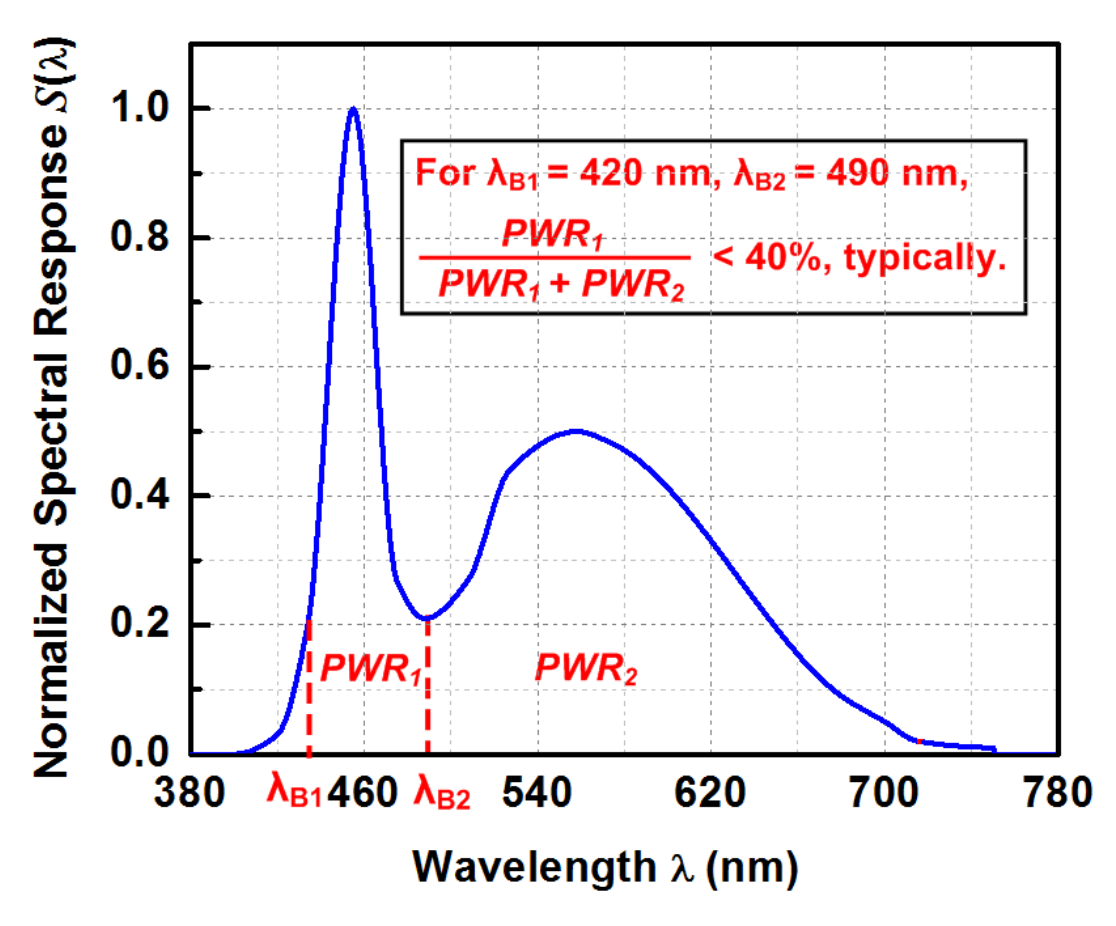


Fig. 4.2 Normalized spectral response of a typical phosphorescent white LED (which is cool white) from the LED data sheet.

As mentioned above, the spectrum of a typical phosphorescent white LED mainly consists of two components, including blue and yellow. The proportion of blue and yellow also determines the correlated color temperature (CCT). A higher CCT indicates a lower proportion of the blue part. Although blue filtering has been employed in many prior works to improve VLC data rates [94] [95], the received optical power is significantly reduced since the yellow spectrum that contributes a large portion of the optical power in the emitted optical signal is filtered out.

Assuming PWR_1 and PWR_2 in Fig. 4.2 denote the total emitted optical power of a phosphorescent white LED for the blue spectrum with a wavelength between λ_{B1} and λ_{B2} , and for the yellow spectrum with a wavelength beyond λ_{B2} , respectively, then they can be expressed as

$$PWR_1 = \int_{\lambda_{R_1}}^{\lambda_{R_2}} cS(\lambda) d\lambda \tag{4.1}$$

$$PWR_2 = \int_{\lambda_{R_2}}^{780} cS(\lambda) d\lambda \tag{4.2}$$

where $S(\lambda)$ is the normalized spectral response of the phosphorescent white LED and c is a scaling factor. By assuming $\lambda_{B1} = \lambda_{peak} - 35nm = 420 \, nm$ and $\lambda_{B2} = \lambda_{peak} + 35nm = 490 \, nm$ (where $\lambda_{peak} = 455 \, nm$ is the peak emission wavelength of the blue spectrum in this case), the proportion of the powe of the blue spectrum with respect to the total emitted optical power of the LED, can be obtained as follows.

$$R_{blue} = \frac{PWR_1}{PWR_1 + PWR_2} < 40\% \tag{4.3}$$

In the above relationship, the optical power of the spectrum with a wavelength below λ_{B1} is ignored as it is very small when compared to $(PWR_1 + PWR_2)$. In general, (4.3) is true for commercial phosphorescent white LEDs available on the market, such as those from Cree, OSRAM and Philips. For a warm white LED with lower CCT, the ratio is even lower. The relationship in (4.3) indicates that more than 60% of the optical power is lost on the receiver side when employing a blue filter, resulting in reduced signal-to-noise ratio and shorter communication distance. Moreover, the received optical power P_R is further limited when taking into consideration the transmittivity of the blue filter $T_{blue}(\lambda)$, which is typically not larger than 90%, and can be expressed as

$$P_R = \int_{\lambda_{R_1}}^{\lambda_{B_2}} cS(\lambda) T_{blue}(\lambda) d\lambda < 90\% * PWR_1$$
 (4.4)

In conclusion, although blue filtering can be utilized in phosphorescent white LED based VLC systems to boost the data rates, the received power on the receiver side is significantly reduced, resulting in a trade-off between data rates and communication distance, which means that the

employment of blue filtering is dependent on the application scenarios.

4.3 Typical Receiver Architecture

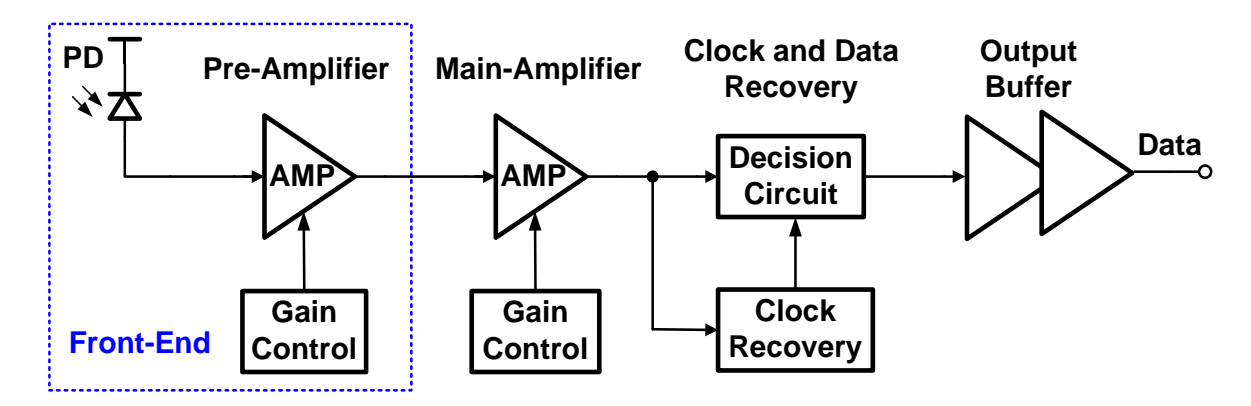


Fig. 4.3 Block diagram of a typical VLC receiver.

A VLC receiver based on a typical optical receiver structure is shown in Fig. 4.3. It usually consists of a PD and a pre-amplifier as the front end to convert light into electrical signal, a series of high-gain main-amplifiers to further amplify and process the signal from the frontend, and a clock and data recovery module to extract clock and retime data from the received signal. Gain control is necessary in the receiver to accommodate variable link distances and input light intensity. One important distinction of a VLC receiver compared to other existing optical receivers is that the employed PD should maintain a high responsivity over the visible light spectrum to attain high receiver sensitivity while eliminating the noise from the other optical spectrums.

4.4 Post-Equalization Techniques

To overcome the limited bandwidth of phosphorescent white LEDs for high-speed VLC applications, different approaches have been proposed, including pre-equation on the transmitter side [95, 96] and post-equalization on the receiver side [88, 89, 94, 95]. In general, the advantage of post-equalization over pre-equalization is that there is no need to apply post-equalization to every LED, thus saving a lot of the hardware budget once the number of LEDs is large. However, most of the post-equalization solutions nowadays are implemented with discrete components instead of custom integration [89, 94, 95], suffering large form size and low energy efficiency for portable applications.

In the receiver presented in [89], the received signal is amplified using a trans-impedance amplifier and equalized using a first-order passive equalizer, which is sketched in Fig. 4.4. The passive equalizer is a parallel combination of a capacitor and a resistor, and can extend the bandwidth of a phosphorescent white LED to 50 MHz by employing an additional blue filter. The achieved data rate is 100 Mb/s with a BER below 10^{-9} .

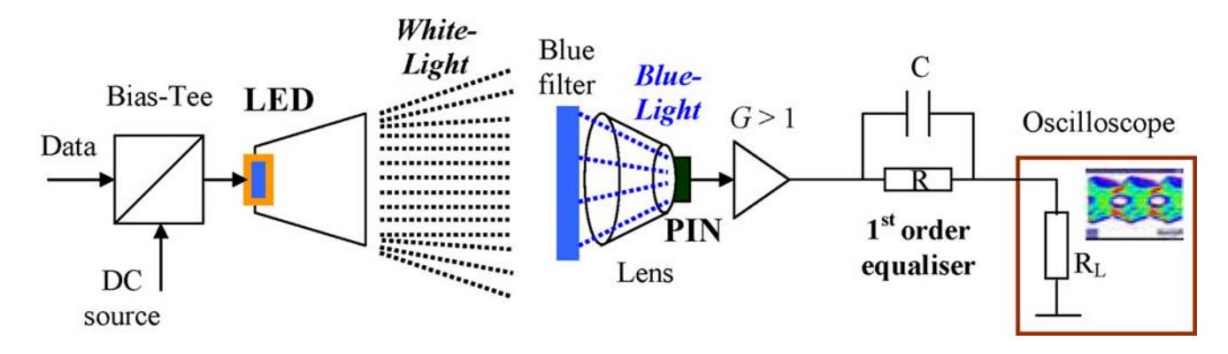


Fig. 4.4 VLC system with 1st order passive equalizer [89].

In [94], a post-equalization circuit comprising two passive equalizers (PEQ1 and PEQ2) and one active equalizer (AEQ) was proposed. The detailed implementation is shown in Fig. 4.5. Experimental results verify its ability to extend the bandwidth of a white LED from 12 MHz (blue-filtered) to 151MHz, and achieve a data rate up to 340 Mb/s with a BER below 2×10^{-3} . Employment of an active equalizer based on a similar principle was also reported in [95].

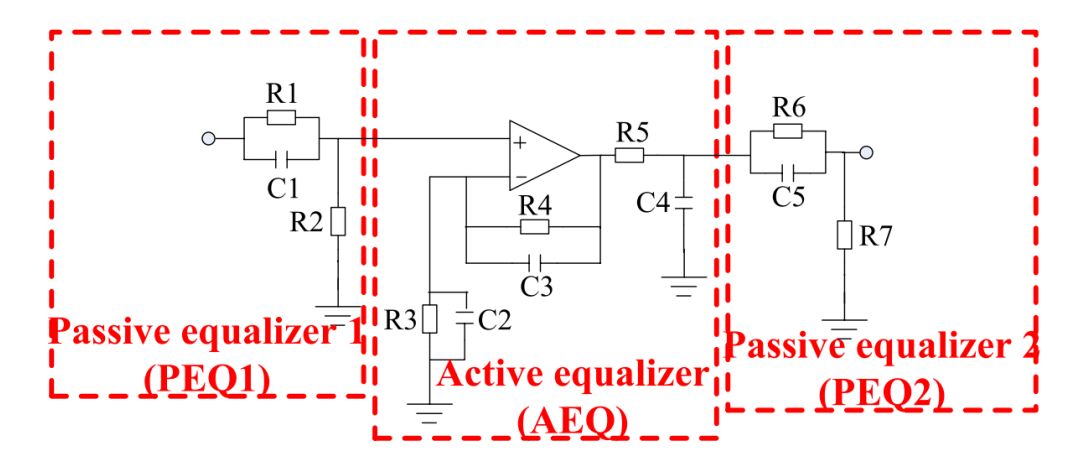


Fig. 4.5 Hybrid passive and active equalizers employed in a VLC receiver [94].

In addition to the aforementioned analog equalization schemes, digital post-equalization was also proposed in [88] for a VLC receiver. The main idea is to treat the commercial white LED

as a low pass filter and then design a complementary filter to make the joint frequency response of the LED and the filter flat within a certain frequency range using FPGA or DSP. The advantage is that it can be easily changed to adapt to different LEDs, but it requires expensive electronic devices. As mentioned before, equalization can also be implemented with advanced modulation schemes, such as OFDM.

CHAPTER 5 VLC Receiver with Ambient Light Rejection and Equalization

5.1 Proposed System Architecture

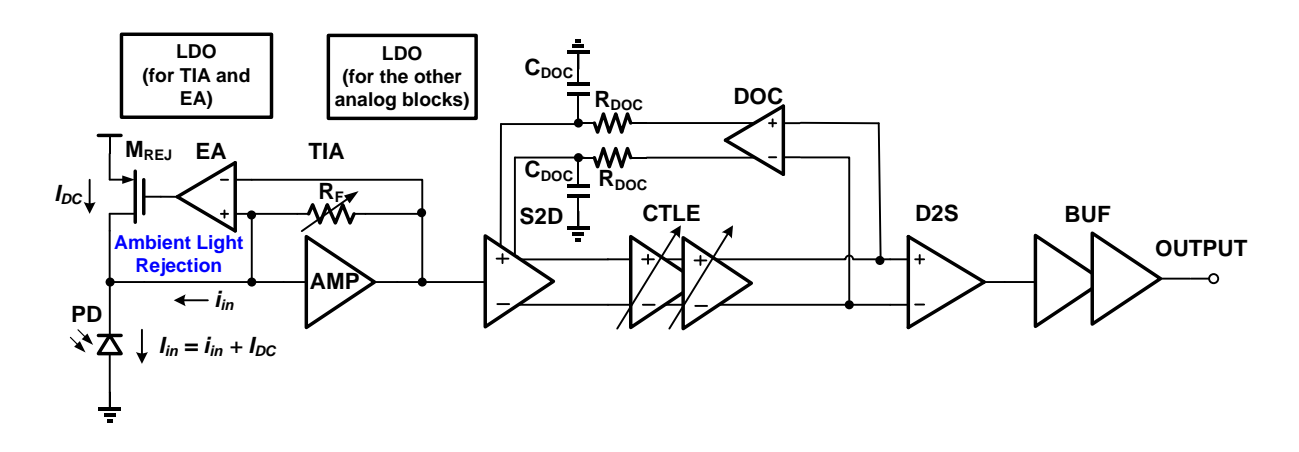


Fig. 5.1 Proposed VLC receiver with ambient light rejection and equalization.

Based on the discussion in the previous chapter, a VLC receiver with ambient light rejection and equalization capability is proposed, as illustrated in Fig. 5.1. It consists of an error amplifier (EA) with a low pass filter (LPF) and a PMOS transistor M_{REJ} as the ambient light rejection module, a trans-impedance amplifier (TIA), a single-to-differential (S2D) converter, a cascade of two continuous time linear equalizers (CTLEs), a DC offset cancellation (DOC) amplifier, a differential-to-single (D2S) amplifier and a series of inverters as the output buffer (BUF). Two LDOs are integrated on chip for better power supply rejection. The operation principle of the proposed receiver SoC is described below.

- 1. The odulated VLC signal and the other ambient light is detected by the PD and converted into photocurrent I_{in} .
- 2. I_{in} flows into the TIA and generates a corresponding voltage at its output. At the same time, the voltage drop across the TIA feedback resistor R_F is amplified and low-pass filtered by the EA, which is then used as a control signal for transistor M_{REJ} to implement ambient light rejection. A higher current induced by the ambient light generates a lower gate voltage for the M_{REJ} .
- 3. The signal at the TIA output is converted into a differential signal by S2D for further

processing of the CTLE, which will boost the gain at high frequencies in order to compensate for the gain loss caused by low-speed phosphorescent white LEDs. In addition, the DOC module suppresses the potential DC offset due to process variations.

4. The output of the CTLE is further amplified and converted into a single-ended signal by the D2S amplifier and output through a buffer (BUF).

The details of the main building blocks are elaborated in the following parts.

5.2 Typical TIA Architecture

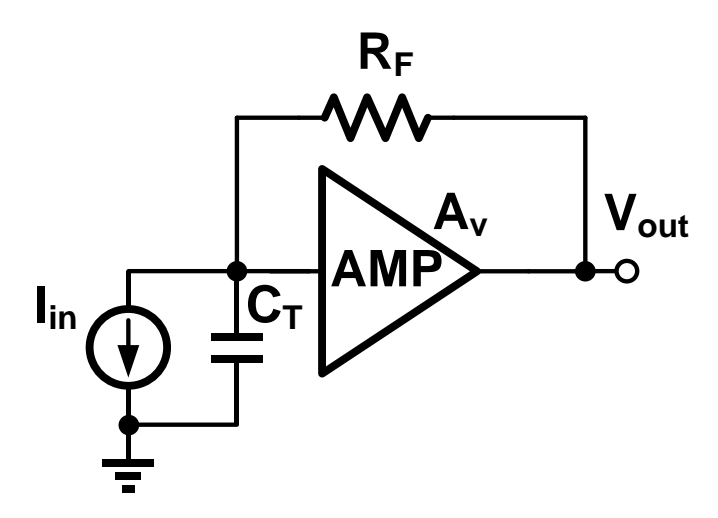


Fig. 5.2 General configuration of a TIA.

A TIA is a device to provide current-to-voltage conversion, and is widely used in photoreceivers. Fig. 5.2 shows a general TIA configuration consisting of a core amplifier with a DC gain of A_v , output resistance of R_o , and a feedback resistor R_F . A shunt-shunt feedback network is employed to provide low input and output impedance to extend the operation bandwidth. Some critical TIA parameters are given by

$$R_{IN_TIA} = \frac{R_F + R_O}{A_v} \approx \frac{R_F}{A_v} \tag{5.1}$$

$$R_{OUT_TIA} = \frac{R_O}{A_n} \tag{5.2}$$

$$A_R = \frac{V_{out}}{I_{in}} = R_F \tag{5.3}$$

$$BW = \frac{A_v}{2\pi R_F C_T} \tag{5.4}$$

where R_{IN_TIA} , R_{OUT_TIA} , A_R and BW are the input and output resistance, trans-impedance gain and -3dB bandwidth of the TIA, respectively, and C_T is the total input capacitance of the TIA, which mainly comes from the PD capacitance.

To be stable, the TIA in Fig. 5.2 usually has a dominant pole at the input, which is $R_F C_T$. Assuming there is also a non-dominant pole ω_{nd} attributed by the core amplifier (AMP). By breaking the feedback at the input of the core amplifier, the open-loop gain LG of the TIA is given by

$$LG = \frac{A_{v}}{(1 + SR_{F}C_{T})(1 + \frac{S}{\omega_{nd}})}$$
 (5.5)

And the unit-gain bandwidth of LG is

$$\omega_t = \frac{A_v}{R_E C_T} \tag{5.6}$$

Based on (5.6), if the gain of TIA, which is R_F , is variable, then the core amplifier gain A_v should also be changed accordingly to maintain a fixed ω_t as well as the phase margin. Otherwise, ω_t moves towards ω_{nd} when R_F is reduced, resulting in a smaller phase margin and reduced stability. The simultaneous change of R_F and A_v is also the requirement for a constant TIA bandwidth such that the receiver sensitivity will not be deteriorated by extra out-of-band noise.

A typical two-stage TIA structure with the cascade of a common source stage (CS) and a source follower (SF) as the core amplifier is sketched in Fig. 5.3, where CS and SF are used for signal amplification and isolation from the loading effect of both R_F and the capacitance of the

following stage, respectively [97]. This structure works well for fixed-gain TIAs, but is not suitable for variable-gain applications since the change of R_A also affects the DC bias conditions of the circuit. In addition, the tracking of R_F and R_A is difficult [91].

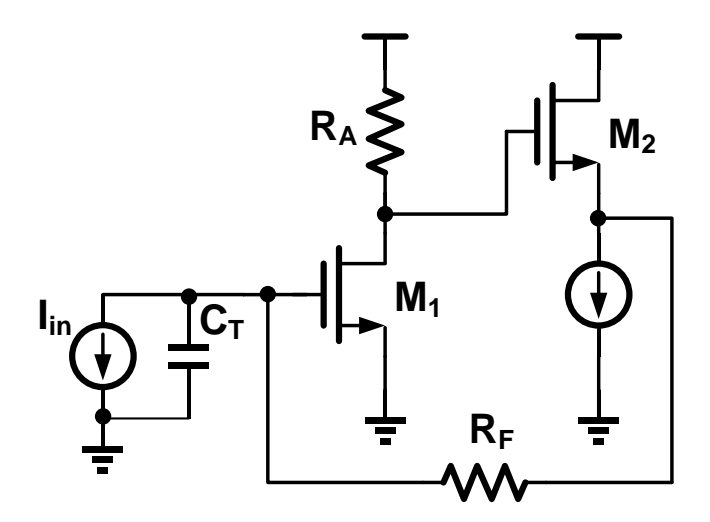


Fig. 5.3 Typical implementation of a two-stage TIA.

5.3 Proposed TIA with Ambient Light Rejection

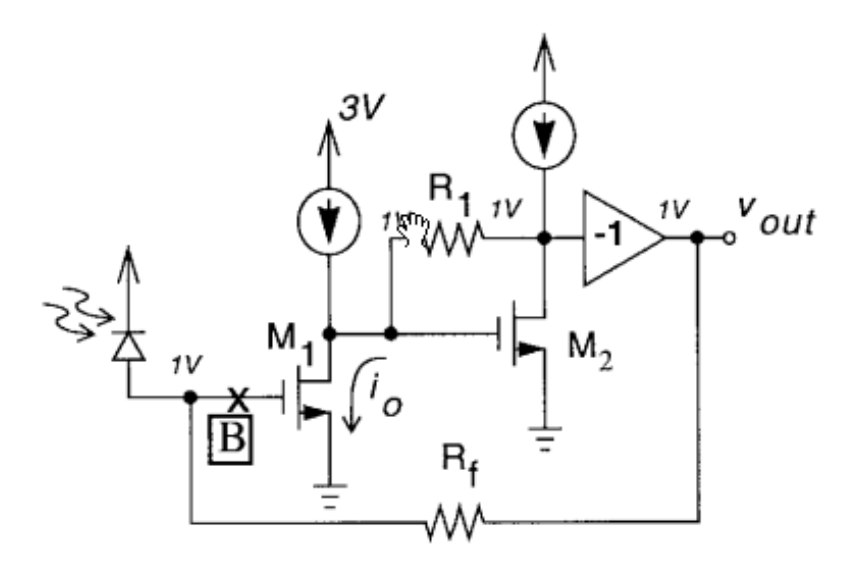


Fig. 5.4 A TIA structure introduced in [91].

In [91], a TIA structure was introduced to overcome the above issues existing in conventional designs, as illustrated in Fig. 5.4. The main idea is to employ a trans-impedance amplifier as the core amplifier, such that gain control can be applied to both the TIA and the core amplifier

without affecting the DC operation points, and thus the TIA bandwidth and stability can be maintained.

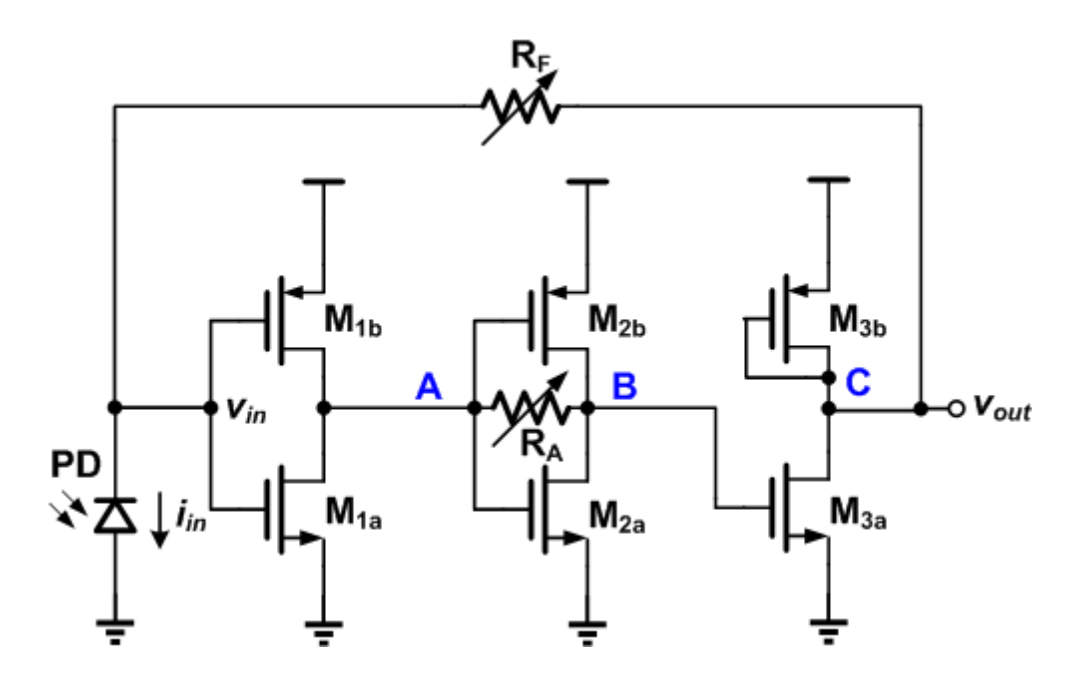


Fig. 5.5 Proposed inverter-based TIA with variable gain.

Based on the structure in Fig. 5.4, an inverter-based TIA is proposed in this thesis, as shown in Fig. 5.5. Specifically, the core amplifier consists of a trans-conductance pair as the input stage, a trans-impedance module as the intermediate stage and an inverting buffer as the output stage. The advantage of this structure is that a current-reuse configuration can provide extra transconductance for the input pair and the intermediate stage, and thus saves power consumption. In addition, no separate bias circuit is required in this structure. As an inverter-based circuit, it is also convenient to be implemented in a CMOS process.

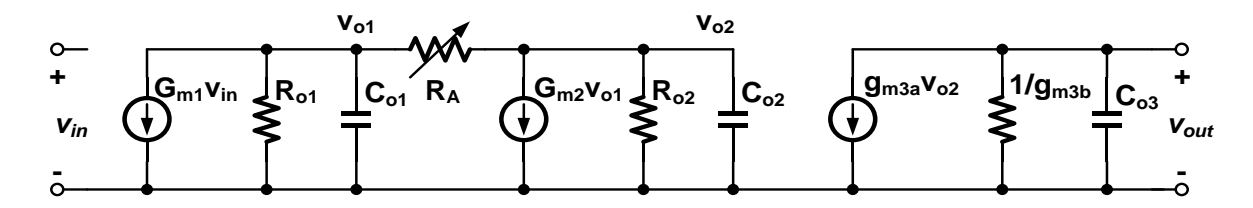


Fig. 5.6 The small-signal model of the core amplifier.

The small-signal model of the core amplifier is shown in Fig. 5.6. By assuming that $G_{m1}R_{o1} \gg 1$, $G_{m2}R_{o2} \gg 1$, and ignoring the gate-drain overlap capacitance of all transistors, the transfer function of the core amplifier is given as follows.

$$A_c(S) = \frac{v_{out}}{v_{in}}$$

$$= \frac{-\frac{G_{m1}}{C_{o1}C_{o2}}(G_{m2} - \frac{1}{R_A})}{S^2 + \frac{S}{C_{o1}C_{o2}}\left[C_{o1}\left(\frac{1}{R_A} + \frac{1}{R_{o2}}\right) + C_{o2}\left(\frac{1}{R_A} + \frac{1}{R_{o1}}\right)\right] + \frac{G_{m2}}{R_AC_{o1}C_{o2}}} \times \frac{\frac{g_{m3a}}{g_{m3b}}}{1 + \frac{SC_{o3}}{g_{m3b}}}$$
(5.7a)

With

$$G_{m1} = g_{m1a} + g_{m1b}$$

 $G_{m2} = g_{m2a} + g_{m2b}$
 $R_{o1} = r_{o1a} // r_{o1b}$
 $R_{o2} = r_{o2a} // r_{o2b}$

where g_{mi} and r_{oi} are the trans-conductance and the drain-source resistance, respectively, of transistor M_i , and C_{o1} , C_{o2} and C_{o3} are the parasitic capacitance at node A, B, and C, respectively. If it is valid that $R_{o1} \gg R_A$, $R_{o2} \gg R_A$, then (5.7a) can be further simplified as

$$A_c(S) \approx \frac{-\frac{G_{m1}}{C_{o1}C_{o2}}(G_{m2} - \frac{1}{R_A})}{S^2 + \frac{S(C_{o1} + C_{o2})}{R_A C_{o1}C_{o2}} + \frac{G_{m2}}{R_A C_{o1}C_{o2}} \times \frac{\frac{g_{m3a}}{g_{m3b}}}{1 + \frac{SC_{o3}}{g_{m3b}}}$$
(5.7b)

When $4G_{m2}R_A - 2 > \frac{C_{o1}}{C_{o2}} \gg 1$, a pair of complex poles is generated in the second-order factor of the denominator in (5.7b). The output pole of the core amplifier, which is related to the first-order factor of the denominator in (5.7b), is usually much higher than the dominant pole of the TIA. When further considering the shunt-shunt feedback effect of the TIA, this output pole can be ignored. If the gate-drain overlap capacitance of transistor M_{2a} and M_{2b} is taken into consideration, then (5.7b) can be modified as follows by replacing $\frac{1}{R_A}$ with $(\frac{1}{R_A} + SC_{gd})$.

$$A_{c}(S) \approx \frac{-\frac{G_{m1}}{C_{o1}C_{o2}} \left(G_{m2} - \frac{1}{R_{A}} - SC_{gd}\right)}{S^{2} + \frac{S(C_{o1} + C_{o2})}{C_{o1}C_{o2}} \left(\frac{1}{R_{A}} + SC_{gd}\right) + \frac{G_{m2}}{C_{o1}C_{o2}} \left(\frac{1}{R_{A}} + SC_{gd}\right)} \times \frac{\frac{g_{m3a}}{g_{m3b}}}{1 + \frac{SC_{o3}}{g_{m3b}}}$$
(5.7c)

where C_{gd} is the total gate-drain overlap capacitance of transistor M_{2a} and M_{2b} . Assuming that $C_{o1} \gg C_{gd}$, $C_{o2} \gg C_{gd}$, and $\frac{C_{o1} + C_{o2}}{C_{gd}} \gg G_{m2}R_A$, then (5.7c) can be further simplified as

$$A_c(S) \approx \frac{-\frac{G_{m1}}{C_{o1}C_{o2}}(G_{m2} - \frac{1}{R_A} - SC_{gd})}{S^2 + \frac{S(C_{o1} + C_{o2})}{R_AC_{o1}C_{o2}} + \frac{G_{m2}}{R_AC_{o1}C_{o2}}} \times \frac{\frac{g_{m3a}}{g_{m3b}}}{1 + \frac{SC_{o3}}{g_{m3b}}}$$
(5.7d)

Compared to (5.7b), (5.7d) has an extra zero located at $\frac{G_{m2} - \frac{1}{R_A}}{2\pi C_{gd}}$, which can be ignored when the bandwidth of the circuit is well below it.

If $G_{m2}R_A \gg 1$ and $\frac{g_{m3a}}{g_{m3b}} \approx 1$, then the pass-band gain of (5.7a) can be expressed as

$$A_c = -G_{m1} \left(R_A - \frac{1}{G_{m2}} \right) \times \frac{g_{m3a}}{g_{m3b}} \approx -G_{m1} R_A \tag{5.7e}$$

Therefore, the trans-impedance gain of the TIA in Fig. 5.5 can be attained as (5.8a) by assuming that the output resistance of the core amplifier is much smaller than the feedback resistor R_F .

$$A_R(S) \approx \frac{R_F}{1 + \frac{SR_FC_T}{-A_c(S)}}$$
 (5.8a)

where C_T is the total capacitance at the TIA input.

By replacing $A_c(S)$ in (5.8a) with A_c , then the TIA trans-impedance gain is

$$A_R \approx \frac{R_F}{1 + \frac{SR_FC_T}{G_{m1}R_A}} \tag{5.8b}$$

Based on (5.8b), the -3dB bandwidth of the TIA is estimated as follows.

$$BW = \frac{G_{m1}R_A}{2\pi R_F C_T} \tag{5.9}$$

According to the noise analysis in [98, 99], a single-stage TIA illustrated in Fig. 5.7 has an

equivalent input referred noise current density as follows by ignoring the gate-drain overlap capacitance of all transistors.

$$I_n^2(\omega) = \frac{4kT}{R_F} + 4kT\gamma G_m \frac{1 + (\omega R_F C_{IN})^2}{G_m^2 R_F^2}$$
 (5.10)

With

$$G_{m1} = g_{ma} + g_{mb}$$

where g_{ma} and g_{mb} are the trans-conductance of transistor M_a and M_b , respectively, while T is the absolute temperature, k is Boltzmann's constant, γ is the transistor excess noise factor, and C_{IN} is the total capacitance at the input of the TIA.

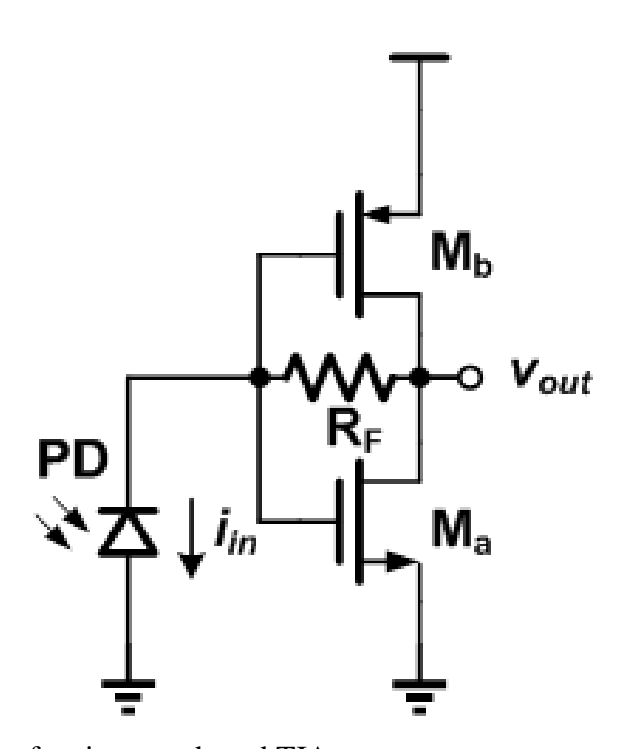


Fig. 5.7 The schematic of an inverter-based TIA.

Therefore, the noise modeling of the proposed TIA is separated into two steps. First, the input referred noise of the core trans-impedance amplifier consisting of M_{2a} , M_{2b} and the feedback resistor R_A is calculated with (5.10) assuming that $C_{o1} \gg C_{o2}$ (and thus ignoring C_{o2} for simplicity), which is then combined with the noise contribution from the input transconductance pair M_{1a} , M_{1b} and the feedback resistor R_F to get the targeted expression by using (5.10) again. The resulting input referred noise current density of the proposed TIA is expressed

as (5.11). In particular, the noise from the last buffer stage of the core amplifier is ignored since it has a minor effect on the TIA input referred noise compared to the leading two stages.

$$I_n^2(\omega) = \frac{4kT}{R_F} + \frac{1 + (\omega R_F C_T)^2}{G_{m_1}^2 R_F^2} \left[4kT\gamma G_{m_1} + \frac{4kT}{R_A} + 4kT\gamma \frac{1 + (\omega R_A C_{o_1})^2}{G_{m_2} R_A^2} \right]$$
(5.11)

where C_T is the total capacitance at the TIA input, and is usually dominated by the parasitic capacitance of the employed PD. The first term refers to the noise from the feedback resistor R_F , which is the main noise source at low frequencies. The second term refers to the noise from the core amplifier, and becomes dominant at high frequencies. To reduce the noise of the TIA and improve the receiver sensitivity, R_F , R_A , G_{m1} and G_{m2} can be increased with trade-off on bandwidth and power consumption.

Ambient light rejection is essential in free-space optical communication to avoid saturating the receiver under strong ambient light interferences [32, 91]. In a typical solution for ambient light rejection as shown in Fig. 5.8 [91], the ambient light is detected as a voltage difference between the two terminals of V_{out} by the error amplifier, and then a voltage is generated to control M_{ctl} for ambient photocurrent rejection. One potential issue of this structure is that the mismatch between the two terminals of V_{out} is also treated as a voltage difference caused by the ambient light, resulting in undesired rejection on the received VLC signal. To address this problem, we propose an alternative solution, as illustrated in Fig. 5.9. The advantage of this solution is that the TIA feedback resistor R_F is also used as the sensing component for ambient light rejection purpose. The DC offset at the input of the error amplifier originating from the TIA core amplifier in Fig. 5.8 is eliminated in Fig. 5.9. A PMOS M_{REJ} is employed instead of an NMOS to avoid high flicker noise.

It is obvious that un-modulated light does not affect the operation of the VLC receiver employing ambient light rejection function. The reason is that un-modulated light only generates a DC photocurrent, which is bypassed (and suppressed) by the ambient light rejection circuit.

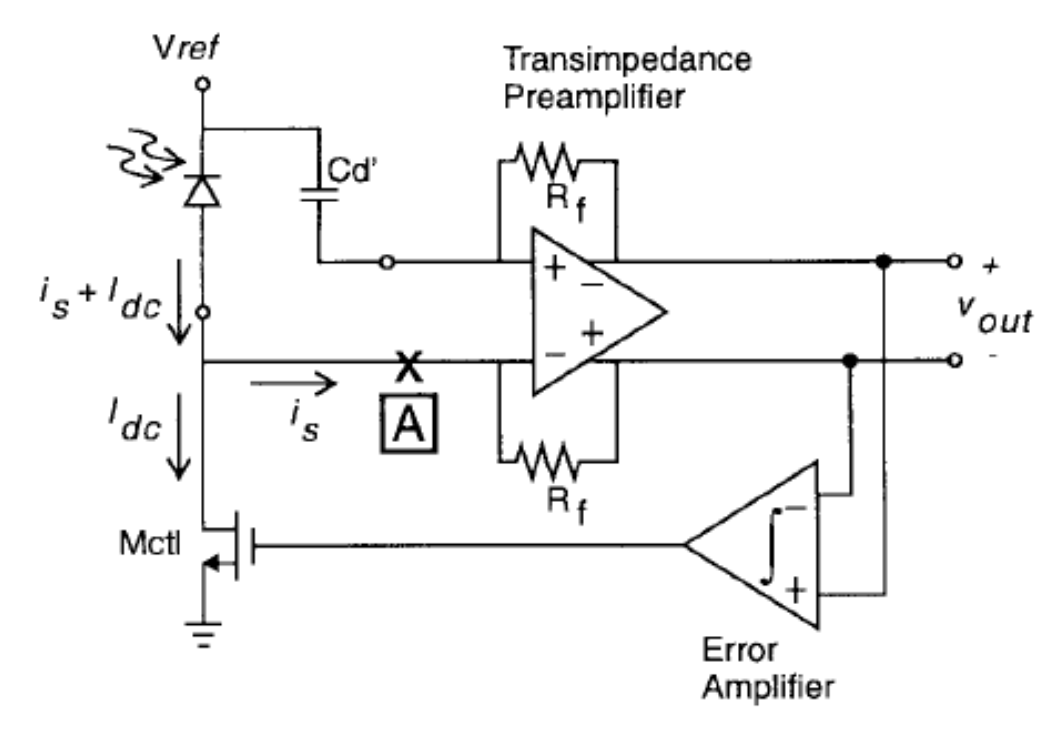
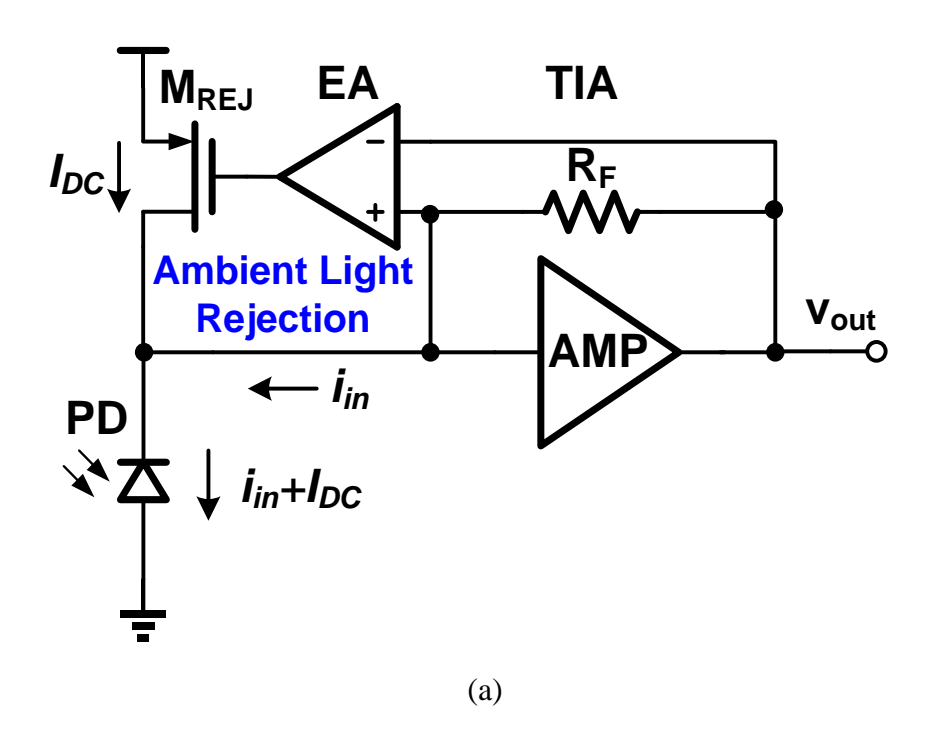


Fig. 5.8 A typical optical preamplifier with ambient light rejection [91].



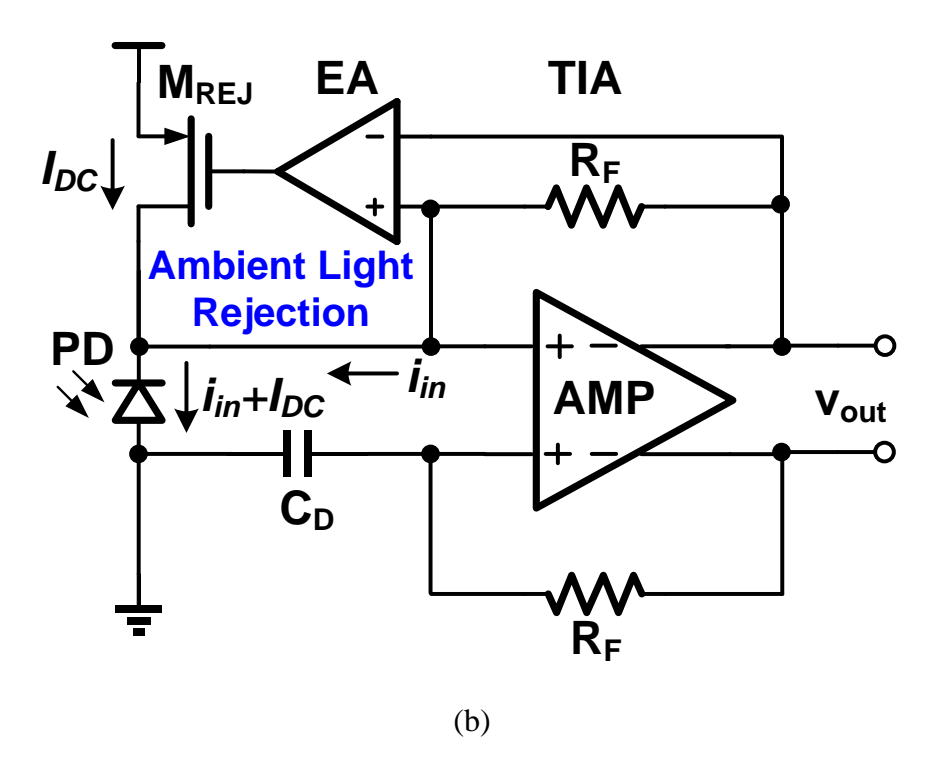


Fig. 5.9 Proposed solution for ambient light rejection with (a) single-ended TIA, and (b) differential TIA.

Based on Fig. 5.9 (a), the closed-loop gain of the TIA with ambient light rejection function is given as follows [91].

$$\frac{v_{out}}{i_{in}} = \frac{A_R}{1 + A_R \times \frac{A_{EA}}{1 + \frac{S}{\omega_{pEA}}}} \approx A_R \times \frac{S + \omega_{pEA}}{S + A_R A_{EA} g_{mREJ} \omega_{pEA}}$$
(5.12)

where A_R is the passband trans-impedance gain of the TIA, g_{mREJ} is the trans-conductance of transistor M_{REJ} , and A_{EA} and ω_{pEA} are the DC voltage gain and the dominant pole of the EA, respectively. Since the zero at ω_{pEA} is much lower than the pole at $A_R A_{EA} g_{mREJ} \omega_{pEA}$, the closed-loop TIA has a high-pass response with a corner frequency at $\omega_{HP} = A_R A_{EA} g_{mREJ} \omega_{pEA}$. It can be observed that the both the DC gain of the closed-loop TIA (which is $\frac{1}{A_{EA} g_{mREJ}}$) and ω_{HP} are proportional to g_{mREJ} , and thus are proportional to the square root of I_{DC} (which is the DC photocurrent generated by ambient light) in Fig. 5.9 (a). Fig. 5.10 illustrates the simulated TIA gain with different DC photocurrents generated by ambient light, demonstrating that the DC gain of the closed-loop TIA reduces and the high-pass corner

frequency ω_{HP} increases with stronger ambient light.

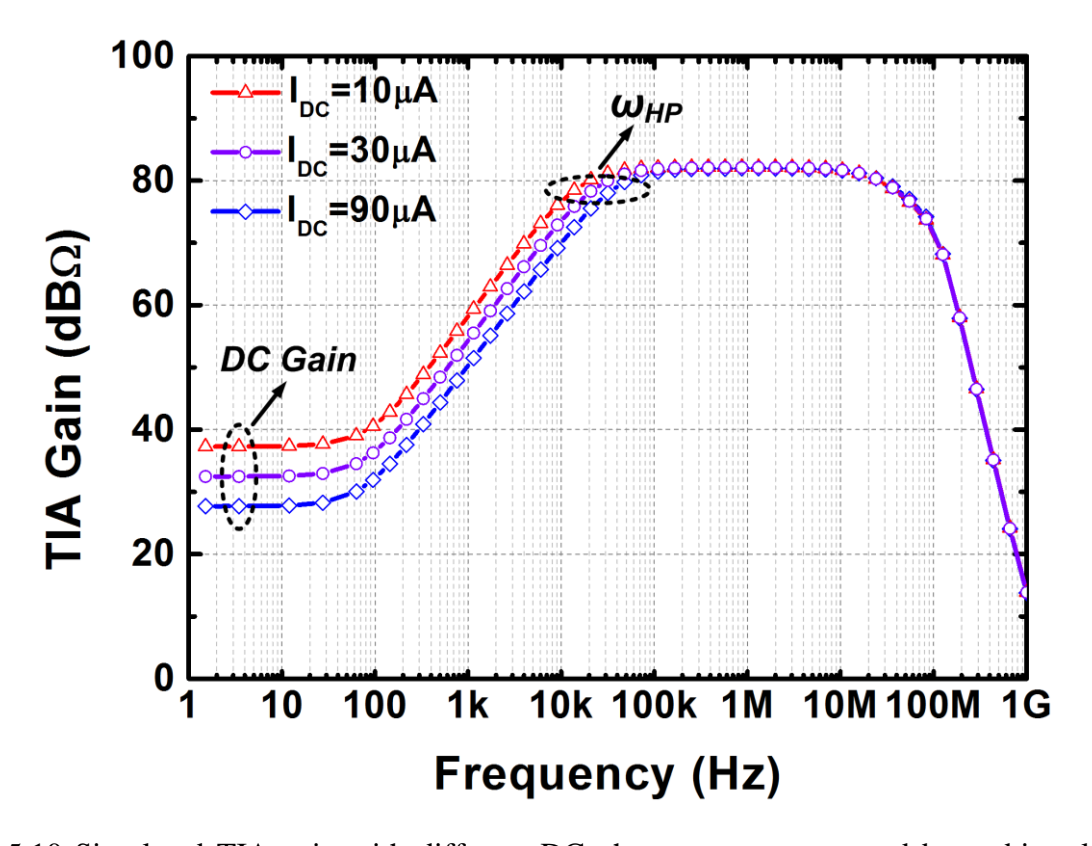


Fig. 5.10 Simulated TIA gain with different DC photocurrents generated by ambient light, where I_{DC} ranges from 10 μA to 90 μA .

5.4 Equalizer

To compensate for the channel loss due to insufficient LED bandwidth, equalizers are employed. By boosting the gain of the VLC receiver at high frequencies using equalizers, distorted high-speed VLC signals can be recovered.

To provide sufficient equalization for VLC signals, a cascade of two CTLEs is employed. The basic structure of each CTLE is depicted in Fig. 5.11. This is a conventional equalizer employing a 3-bit digitally tunable capacitor C_{EQ} , while C_L is a 2-bit capacitor to provide extra controllability [100].

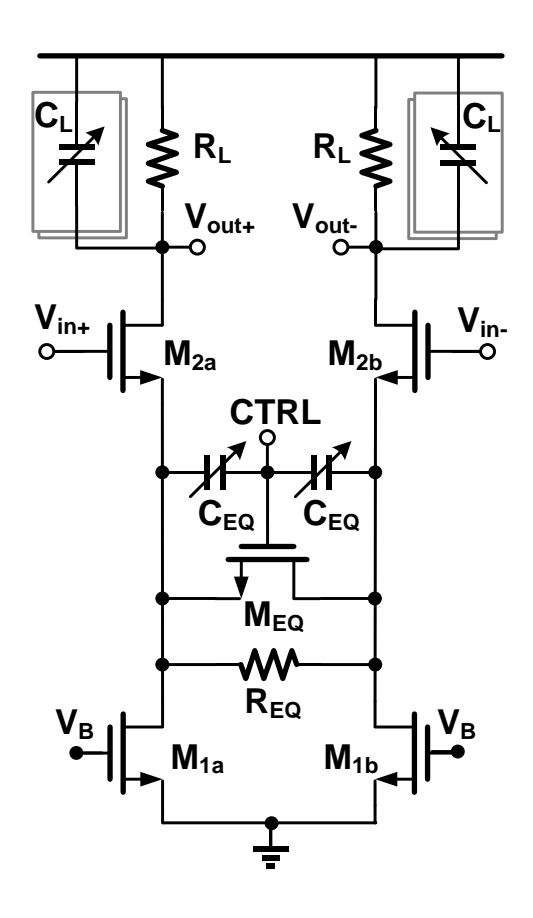


Fig. 5.11 CTLE with a 3-bit digitally tunable capacitor C_{EQ} .

The transfer function of the CTLE is shown as follows.

$$\frac{v_{out+} - v_{out-}}{v_{in+} - v_{in-}} = -\frac{g_m R_L}{1 + \frac{g_m R_{EQ}}{2}} \times \frac{1 + \frac{S}{\omega_z}}{\left(1 + \frac{S}{\omega_{p1}}\right)\left(1 + \frac{S}{\omega_{p2}}\right)}$$
(5.13)

With

$$\omega_{z} = \frac{2}{R_{EQ}C_{EQ}}$$

$$\omega_{p1} = \left(1 + \frac{g_{m}R_{EQ}}{2}\right) \frac{2}{R_{EQ}C_{EQ}}$$

$$\omega_{p2} = \frac{1}{R_{L}C_{L}}$$

where g_m is the trans-conductance of transistor M_{2a} and M_{2b} . It is obvious that the zero ω_z is located away from the pole ω_{p1} by a factor of $\left(1 + \frac{g_m R_{EQ}}{2}\right)$, which is the same as the denominator of the DC gain in (5.13), indicating a tradeoff between the maximum achievable

equalization and the DC gain.

5.5 Differential-to-Single Amplifier

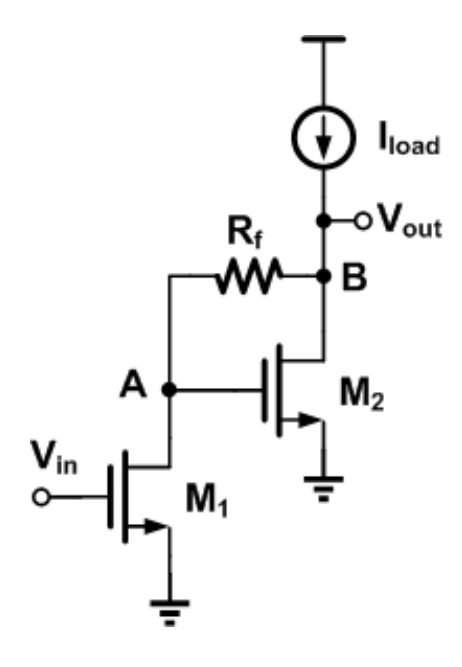


Fig. 5.12 Configuration of a conventional single-ended Cherry-Hooper amplifier [101].

Fig. 5.12 is the configuration of a conventional single-ended Cherry-Hooper amplifier, where a local feedback between the gate and the drain of transistor M_2 using resistor R_f is employed to increase the operation speed of the circuit [101]. Specifically, the feedback resistor R_f detects the output signal and returns the current to transistor M_1 . The advantage of this configuration is that low equivalent resistance at nodes A and B can be achieved, which is typically determined by the trans-conductance of transistor M_2 instead of R_f . Assuming an ideal current source as the loading of this amplifier, and the equivalent resistance at nodes A and B are denoted as R_A and R_B , respectively, then the following equations can be attained.

$$R_A = \frac{R_f + r_{od2}}{1 + g_{m2}r_{od2}} / / r_{od1} \approx \frac{1}{g_{m2}}$$
 (5.14)

$$R_B = \frac{R_f + r_{od1}}{1 + g_{m2}r_{od1}} / / r_{od2} \approx \frac{1}{g_{m2}}$$
 (5.15)

where r_{od1} and r_{od2} are the output resistance of M_1 and M_2 , respectively, while gm_2 is the transconductance of M_2 . By neglecting r_{od1} and r_{od2} , the low-frequency small-signal gain of the

amplifier can be expressed as follows.

$$\frac{V_{out}}{V_{in}} = g_{m1}R_f - \frac{g_{m1}}{g_{m2}} \approx g_{m1}R_f, \quad if \ g_{m2}R_f \gg 1.$$
 (5.16)

In summary, this Cherry-Hooper amplifier consists of two parts, including the input transconductance stage and the trans-impedance stage with local feedback. Compared to a typical single-stage common-source amplifier with the same voltage gain, its advantage is the low impedance at the internal and output nodes, resulting in high operation bandwidth [101], while the drawback is the extra DC current required to bias transistor M₂.

Based on the Cherry-Hooper structure, a D2S amplifier that is suitable for high-speed applications is proposed. Fig. 5.13 presents the schematic of the D2S amplifier employing an inverter-based buffer stage. In particular, transistor M_{2a} and M_{2b} act as the input transconductance pair, while a buffer stage comprising transistors M_{4a} , M_{4b} , and resistor R_{TIMP} serves as the trans-impedance stage. The equivalent input and output resistance of the buffer stage (denoted as R_{IN} and R_{OUT} , respectively) can be expressed as follows.

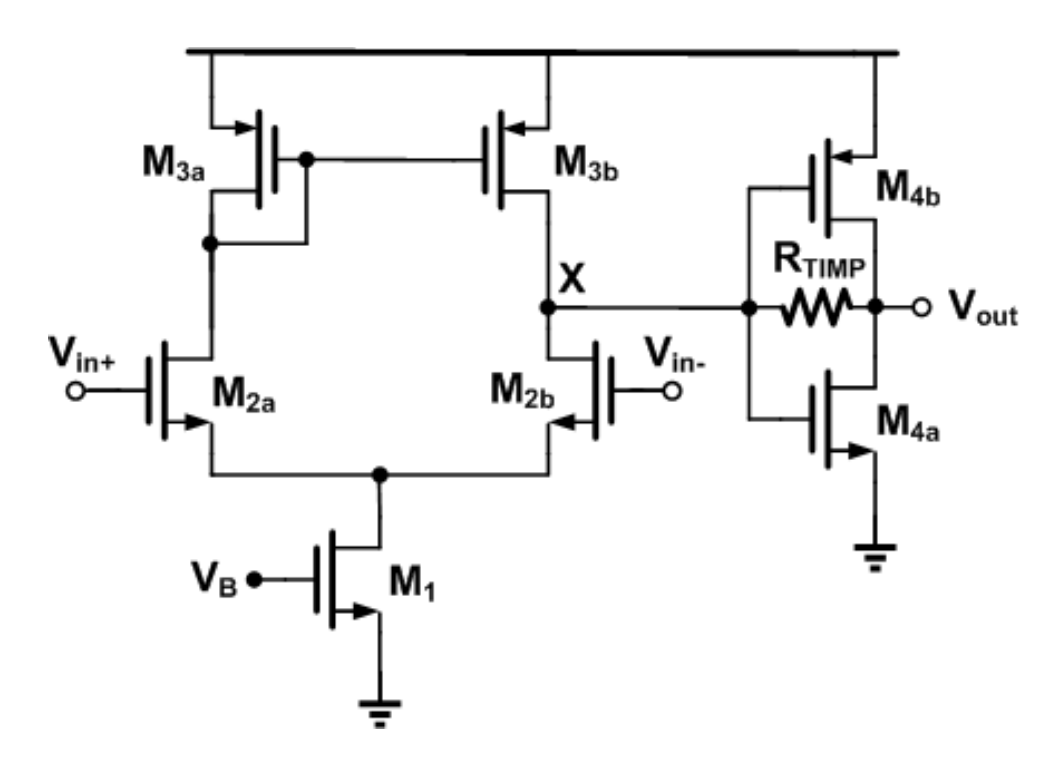


Fig. 5.13 Schematic of the differential-to-single (D2S) amplifier based on the Cherry-Hooper amplifier structure.

$$R_{IN} = \frac{R_{TIMP} + (r_{od4a}//r_{od4b})}{1 + (g_{m4a} + g_{m4b})(r_{od4a}//r_{od4b})}$$

$$\approx \frac{1}{g_{m4a} + g_{m4b}}, if (r_{od4a}//r_{od4b}) \gg R_{TIMP}.$$
 (5.17)

$$R_{OUT} = \frac{R_{TIMP} + R_{OUT1}}{1 + (g_{m4a} + g_{m4b})R_{OUT1}} / (r_{od4a} / r_{od4b})$$

$$\approx \frac{1}{g_{m4a} + g_{m4b}}, if \ R_{OUT1} \gg R_{TIMP} \ and \ \frac{1}{g_{m4a} + g_{m4b}}. \tag{5.18}$$

where g_{m4a} and g_{m4b} are the trans-conductance of transistor M_{4a} and M_{4b} , respectively, while r_{od4a} and r_{od4b} are the corresponding output resistance, and R_{OUT1} is the equivalent output resistance of the first stage seen at node X, which is typically much larger than R_{TIMP} .

By neglecting the output resistance of all the transistors, the low-frequency small-signal gain of the D2S amplifier can be expressed as follows.

$$\frac{V_{out}}{V_{in+} - V_{in-}} \approx g_{m2} R_{TIMP}, if (g_{m4a} + g_{m4b}) R_{TIMP} \gg 1.$$
 (5.19)

The advantage of the proposed D2S amplifier is the high operation bandwidth and large output voltage headroom, which are desired at the output stage of the receiver.

5.6 Other Blocks

Fig. 5.14 is the schematic of the error amplifier. It is a symmetrical CMOS operational transconductance amplifier (OTA) with a large external capacitor to provide a low-pass filtered control voltage for ambient light rejection. Specifically, transistor M_{2a} and M_{2b} is the input trans-conductance pair used to sense the voltage difference across the TIA feedback resistor and convert it into current. Then the current is mirrored through transistor $M_{3a/b}$, $M_{4a/b}$, and $M_{5a/b}$, and finally low-pass filtered at the output of the error amplifier with a corner frequency of $\frac{1}{(r_{od4b}//r_{od5b})C_{LPF}}$, where r_{od4b} and r_{od5b} are the output resistance of transistor M_{4b} , and M_{5b} , respectively. Since the voltage swing at the TIA input is much smaller than that at the TIA output (as shown in (5.20)), the TIA input can act as the reference terminal for ambient light

rejection control.

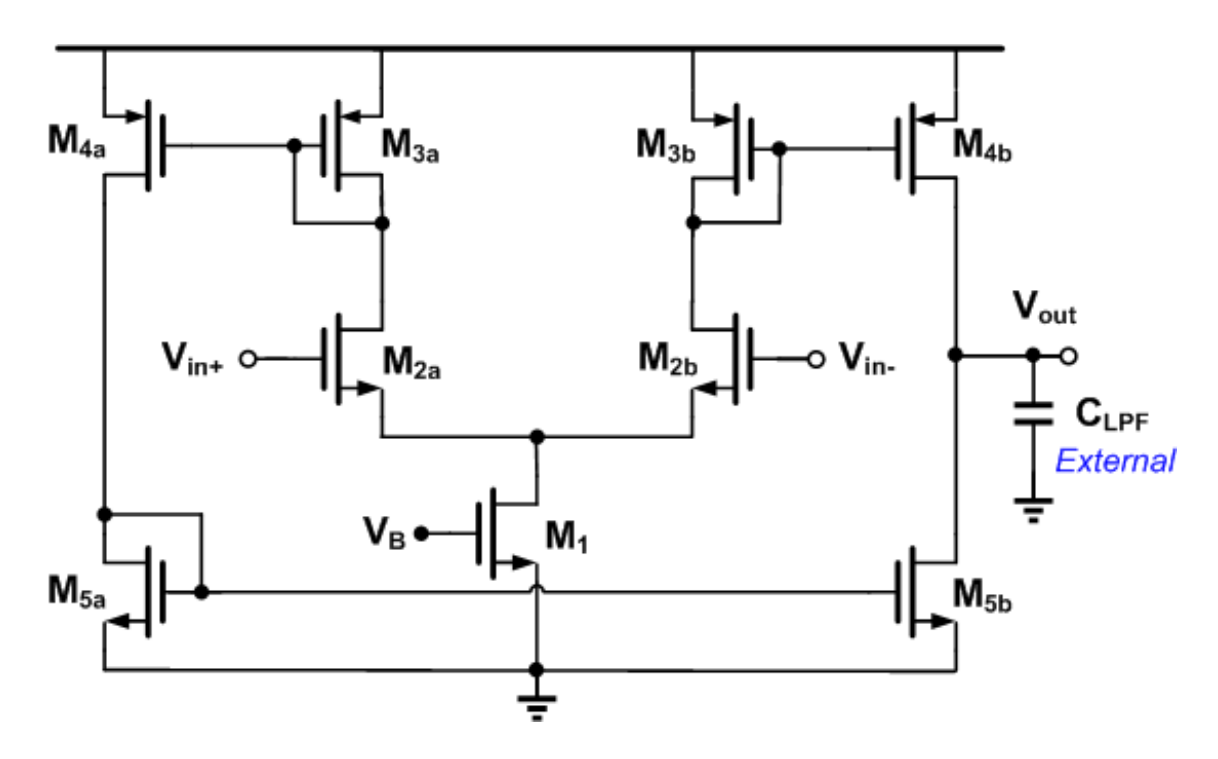


Fig. 5.14 Schematic of the error amplifier (EA).

$$v_{TIA_{IN}} = \frac{v_{TIA_{OUT}}}{A_{core}} \ll v_{TIA_{OUT}} \tag{5.20}$$

where v_{TIA_IN} and v_{TIA_OUT} denote the voltage swing at the input and output of the TIA, respectively, and A_{core} is the voltage gain of the TIA core amplifier, which is usually much larger than 1. The voltage gain $A_{EA}(s)$ of the EA can be expressed as (5.21).

$$A_{EA}(s) = \frac{g_{m2}(r_{od4b}//r_{od5b})}{1 + s(r_{od4b}//r_{od5b})C_{LPF}}$$
(5.21)

where g_{m2} is the trans-conductance of transistor $M_{2a/b}$.

The schematic of the S2D amplifier is depicted in Fig. 5.15, where transistor M_{2a} and M_{2b} act as the input pair for the single-ended TIA output. A low pass filter consisting of R_B and C_B is adopted to filter out the AC part of the input signal while providing proper DC bias for the input transistors to implement single-to-differential conversion. Transistors M_{3a} and M_{3b} are employed as part of the DC offset cancellation network to eliminate DC offset in conjunction with the DOC module. The loading of the S2D block consists of a cross-coupling pair M_{4a}/M_{4b}

and a diode-connected pair M_{5a}/M_{5b} using a current cancellation technique [97], as illustrated in Fig. 5.16, where (a) is a cross-coupling pair, (b) is a diode-connected pair, while (c) shows the combination of the cross-coupling pair and the diode-connected pair. Z_{in4} , Z_{in5} and Z_{in} are the corresponding equivalent resistance of each structure, respectively, which can be expressed as follows.

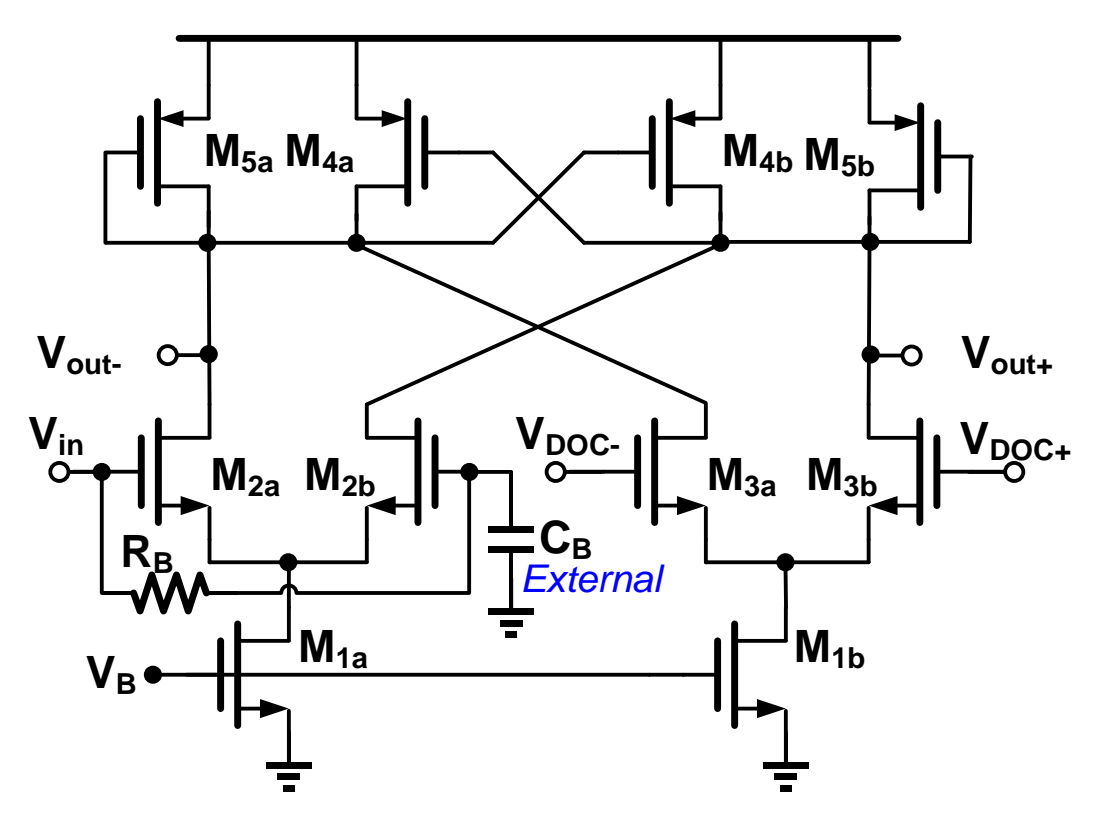


Fig. 5.15 Schematic of the single-to-differential (S2D) amplifier.

$$Z_{in4} = -\frac{2}{g_{m4}} \tag{5.22}$$

$$Z_{in5} = \frac{2}{g_{m5}} \tag{5.23}$$

$$Z_{in} = Z_{in4} / / Z_{in5} = \frac{2}{g_{m5} - g_{m4}}$$
 (5.24)

where g_{m4} and g_{m5} are the trans-conductance of transistor $M_{4a/b}$ and $M_{5a/b}$, respectively. The desired loading can be attained by changing the difference between g_{m4} and g_{m5} .

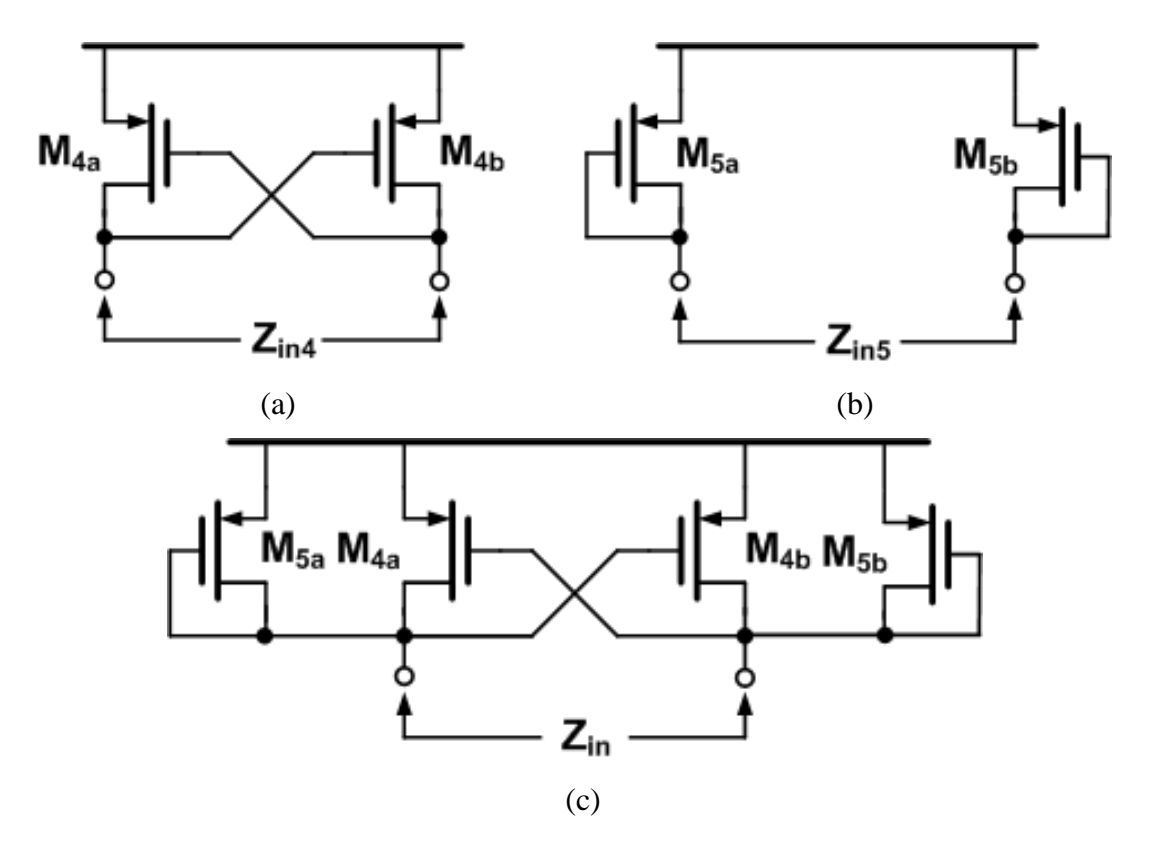
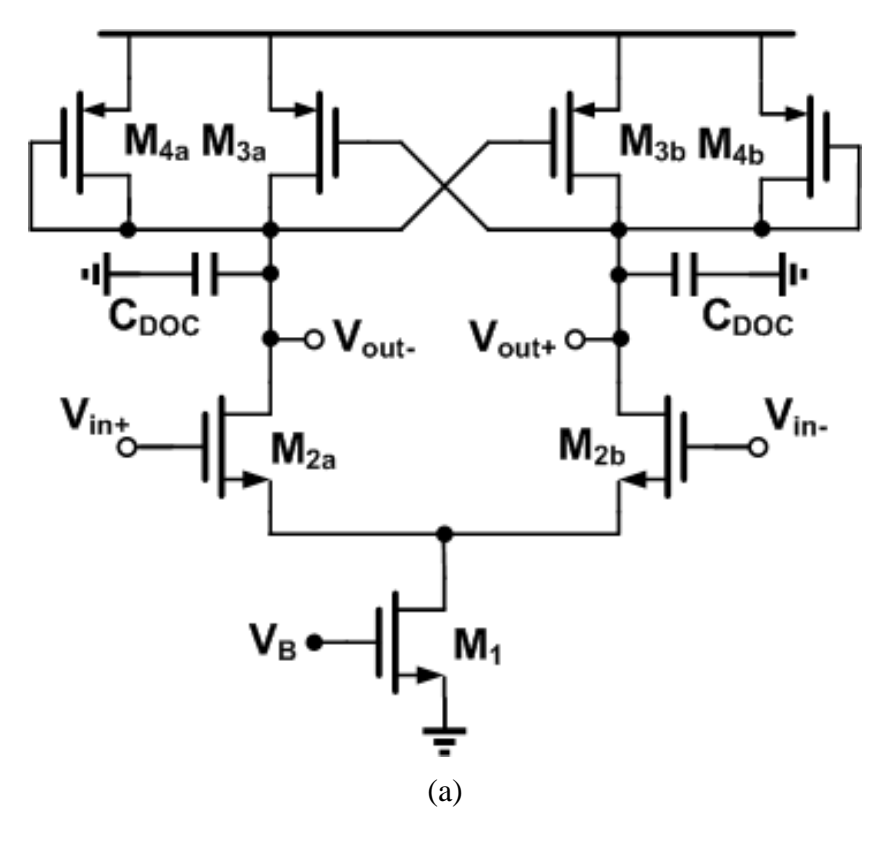


Fig. 5.16 Illustration of a current cancellation technique: (a) cross-coupling pair, (b) diodeconnected pair, and (c) combination of the cross-coupling pair and the diode-connected pair.



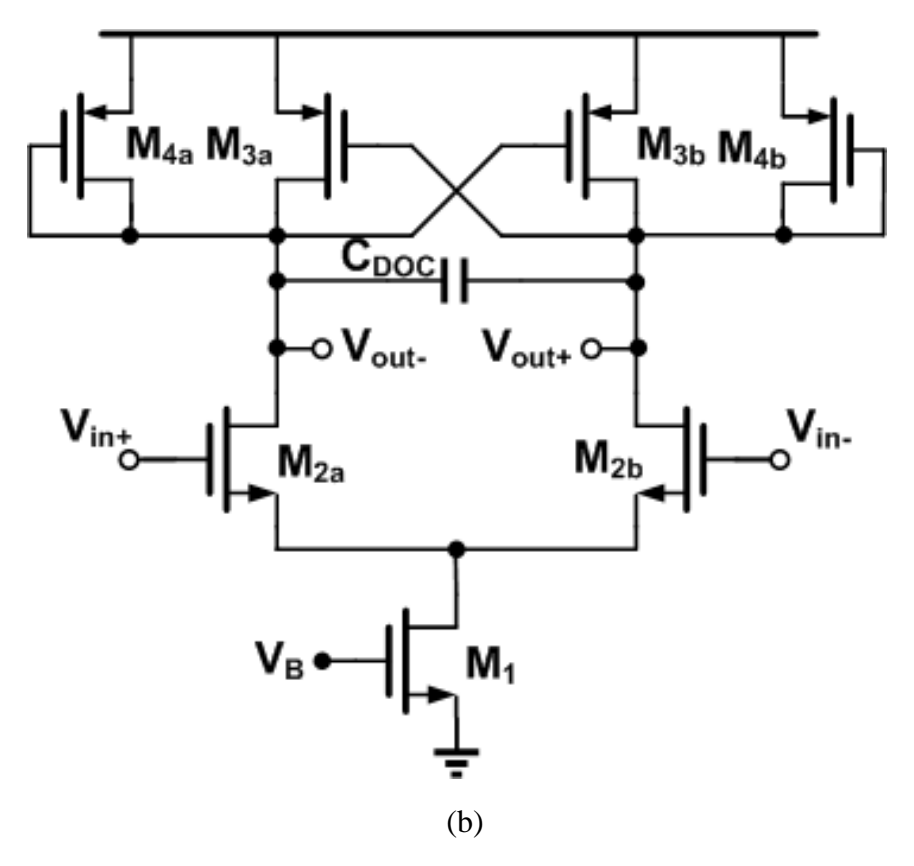


Fig. 5.17 Schematic of the DC offset cancellation (DOC) amplifier (a) using two capacitors, and (b) using only one capacitor.

Since a typical optical receiver only has a single-ended input, which is the case in our design, DC offset is unavoidable. In particular, the offset in the leading stages (such as that at the output of the S2D block) will be amplified by the subsequent stages and eventually prevent the circuits from working at the desired DC operation points. To avoid this potential problem, a DC offset cancellation feedback loop is built on chip by using a DOC amplifier, as shown in Fig. 5.17. Similar to the S2D block, current cancellation is employed through transistors $M_{3a/b}$ and $M_{4a/b}$ to create high loading resistance and achieve high voltage gain [97]. Since this amplifier serves as part of the low-speed feedback loop for DC offset cancellation, the sizes of the four loading transistors are designed to be the same with good matching. In theory, the equivalent loading resistance can be as high as $\frac{r_{od}}{2}$ at each output terminal, where r_{od} is the output resistance of each loading transistor. The corner frequency of the DOC amplifier is determined by taking into consideration the trade-off between the input referred noise and the offset cancellation capability. More offset cancellation requires higher DOC corner frequency, resulting in higher input referred noise at the receiver input due to more trans-impedance gain suppression at low

frequencies. In Fig. 5.17 (a), two capacitors are employed in conjunction with the loading resistance to determine the DOC corner frequency, which can be further combined into one capacitor to reduce hardware budget, as shown in Fig. 5.17 (b). The DOC corner frequencies in Fig. 5.17 are expressed as follows.

In Fig. 5.17 (a),

$$\omega_{DOC} = \frac{1}{\frac{r_{od}}{2} \times C_{DOC}} = \frac{2}{r_{od} \times C_{DOC}}$$
 (5.25)

In Fig. 5.17 (b),

$$\omega_{DOC} = \frac{1}{\frac{r_{od}}{2} \times 2C_{DOC}} = \frac{1}{r_{od} \times C_{DOC}}$$
 (5.26)

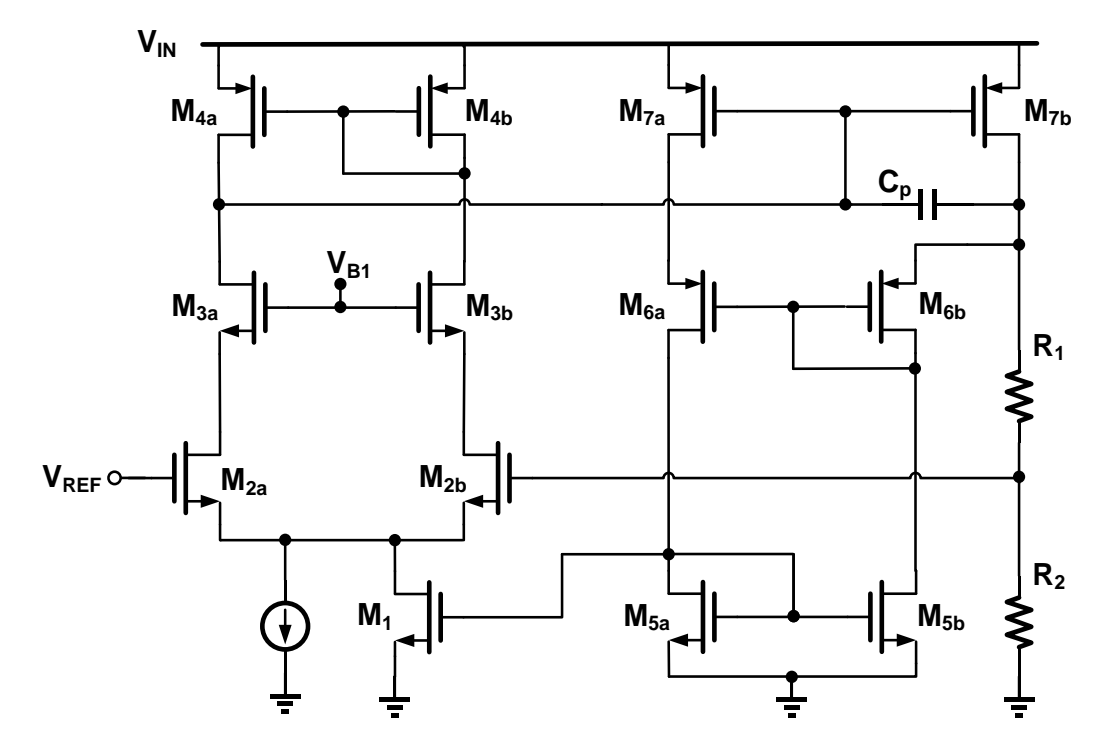


Fig. 5.18 Schematic of the LDO.

To provide better power supply rejection, two LDOs are integrated on chip. As depicted in Fig. 5.18, the output of the LDO is detected by a voltage divider consisting of R_1 and R_2 for comparison with a reference V_{REF} to generate the desired output voltage, which is 1.8 V in this application. Capacitor C_p is connected between the gate and the drain of power transistor M_{7b}

for Miller compensation, while transistor M_{7a} is employed as an output current sensing component for M_1 to implement dynamic stability compensation and improve the transient response of the LDO.

5.7 Simulation and Experimental results

It is obvious that process variations will affect the value of the employed capacitors. However, some measures have been taken to avoid the resulting undesired change of the corner frequency for ambient rejection and post-equalization. In terms of ambient light rejection, we used an external capacitor that is large enough to suppress DC ambient photocurrents, and thus the usual capacitance variations would not affect the ambient light rejection performance. In terms of post-equalization, 3-bit digitally tunable on-chip capacitors have been employed to deal with the variations.

The microphotograph of the proposed receiver SoC is shown in Fig. 5.19, which is implemented in a 0.18-µm CMOS process, occupying an area of 0.7×0.4 mm².

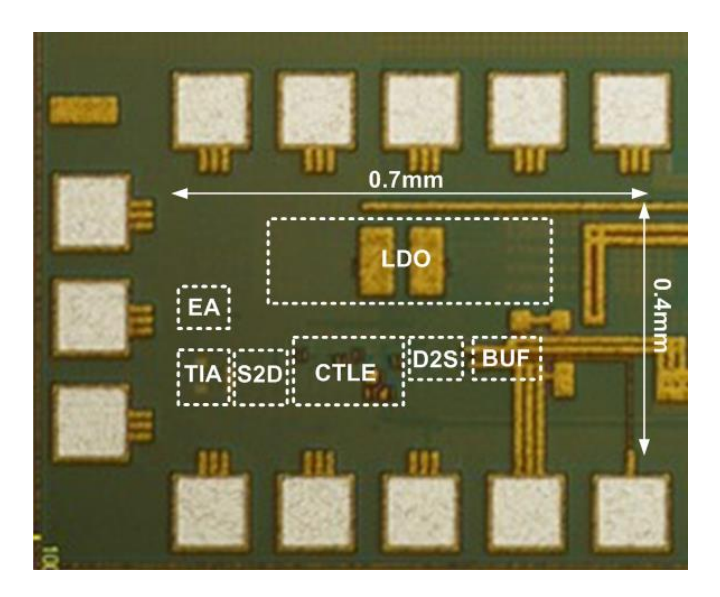
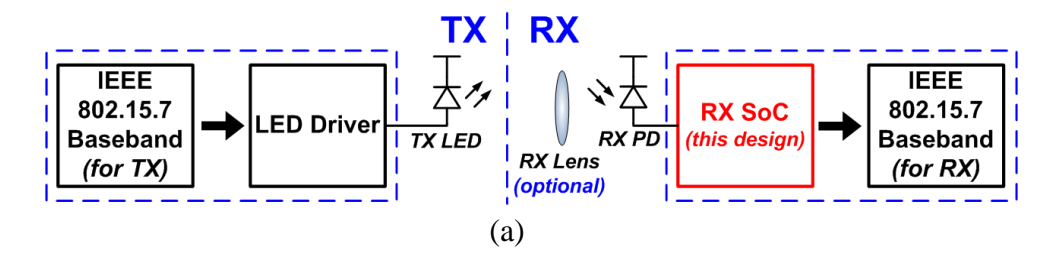
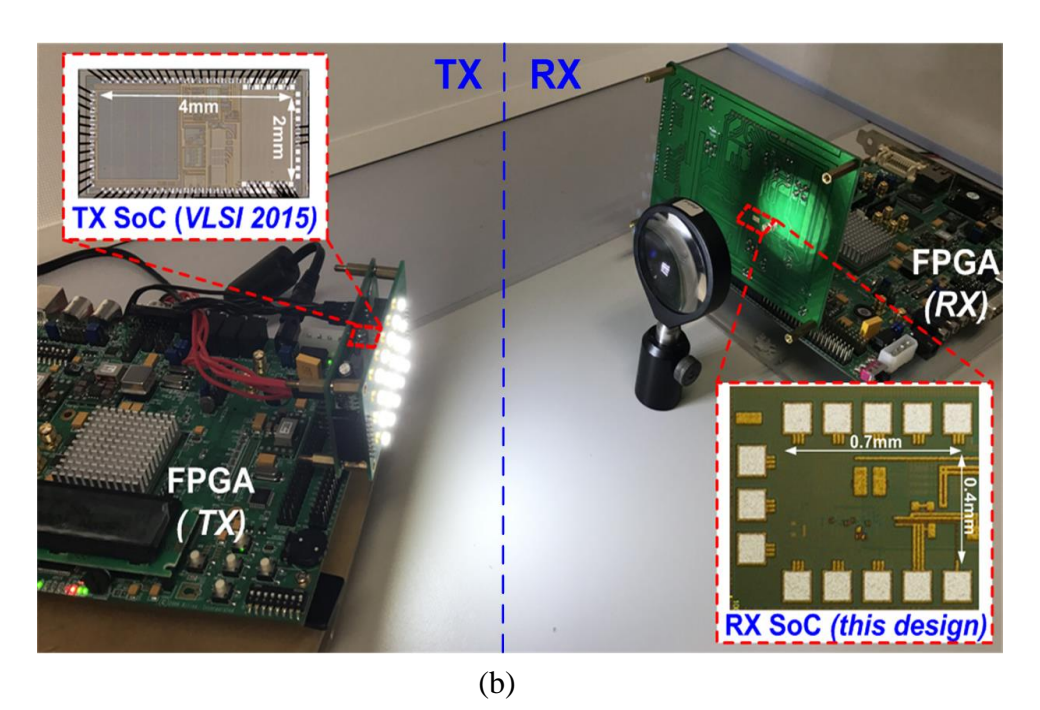


Fig. 5.19 Microphotograph of the proposed receiver SoC.

Fig. 5.20 (a) is an IEEE 802.15.7 PHY-II VLC system that consists of the proposed receiver SoC and a custom transmitter SoC [20] without employing a blue filter. On the transmitter (TX) side, data packets to be transmitted are first processed by a baseband unit according to the IEEE standard, then converted by a high-speed LED driver into modulated light from 1-W

phosphorescent white LEDs. The transmitter SoC is implemented in a 0.35-μm CMOS process occupying an area of 4×2 mm². On the receiver (RX) side, the modulated light is detected by a PD (Vishay BPV10) and converted into current, which is then forwarded to the proposed receiver SoC for further processing. Since the targeted data rate is far beyond the bandwidth limitation of the white LEDs, the received VLC signal from the PD experiences sever intersymbol interference (or baseline wander), which can be eliminated by the post-equalization circuit on the receiver. The digital output of the receiver is then connected to another baseband unit to extract the payload data. A lens can be employed on the receiver side to extend the communication distance by focusing more light onto the PD. Since in a real illumination system, the light source is supposed to have a wide viewing angle, no transmitter lens is utilized in this system. The photograph of the system, including the transmitter SoC and the proposed receiver SoC, is shown in Fig. 5.20 (b), and the specification of the key components is summarized and listed in Fig. 5.20 (c).

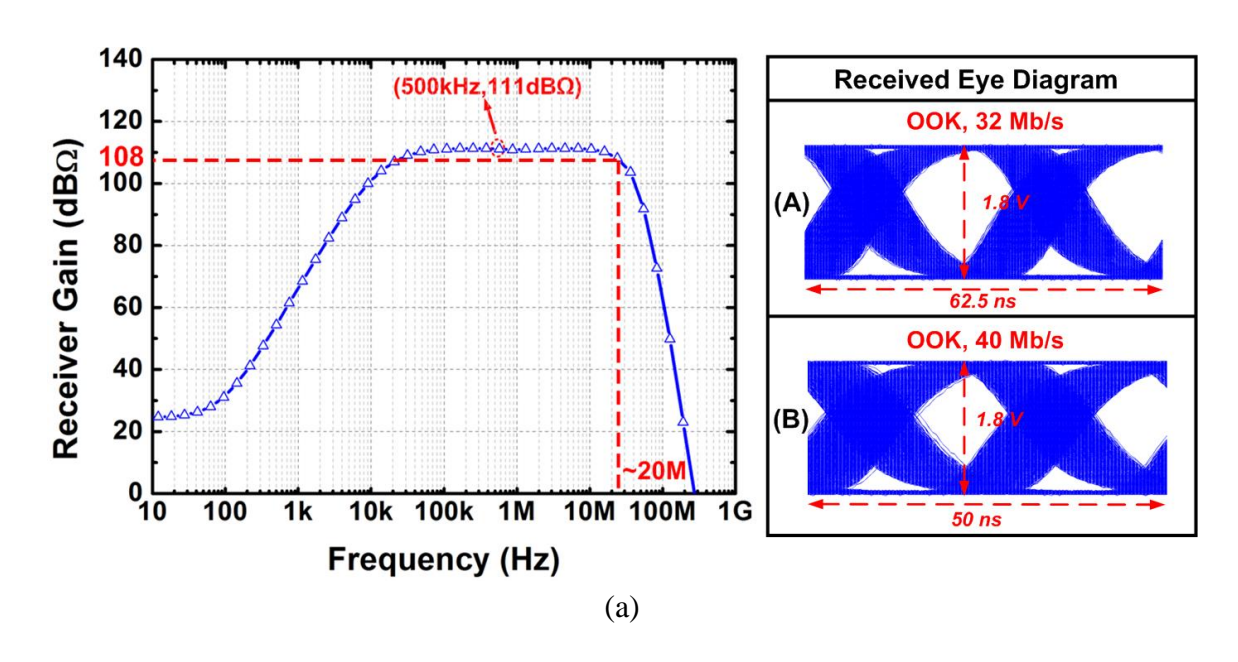




| Component Specification | | | | | |
|-----------------------------|---------------------|---------------------------------|--|--|--|
| | Model | Cree CLA1B-WKW | | | |
| TX LED | Power Consumption | ~1 W | | | |
| | Total Luminous Flux | 107 lm | | | |
| | Color Temperature | ~5000 K | | | |
| | Bandwidth | ~2.2 MHz | | | |
| RX Lens | Diameter | 5 cm | | | |
| | Focal length | 10 cm | | | |
| RX PD | Model | Vishay BPV10 | | | |
| | Detector Type | Silicon PIN | | | |
| | Wavelength Range | 380 - 1100 nm | | | |
| | Detector Area | 0.78 mm ² | | | |
| | Bandwidth | 250 MHz @ V _R = 12 V | | | |
| | Peak Responsivity | 0.55 A/W @ 950 nm | | | |
| | Diode Capacitance | 7 pF @ V _R = 0.9 V | | | |
| | Model | New Focus 1801-FC | | | |
| | Detector Type | Silicon PIN | | | |
| Commercial Photoreceiver | Wavelength Range | 320 - 1000 nm | | | |
| | Detector Diameter | 0.4 mm | | | |
| | Bandwidth | 125 MHz | | | |
| | Peak Responsivity | 0.5 A/W @ 800 nm | | | |
| | Max Conversion Gain | 2.4x10 ⁴ V/W | | | |

(c)

Fig. 5.20 An IEEE 802.15.7 PHY-II VLC system that consists of the proposed receiver SoC and a custom transmitter SoC [20] without employing a blue filter: (a) block diagram of the system, (b) photograph of the system, and (c) component specification.



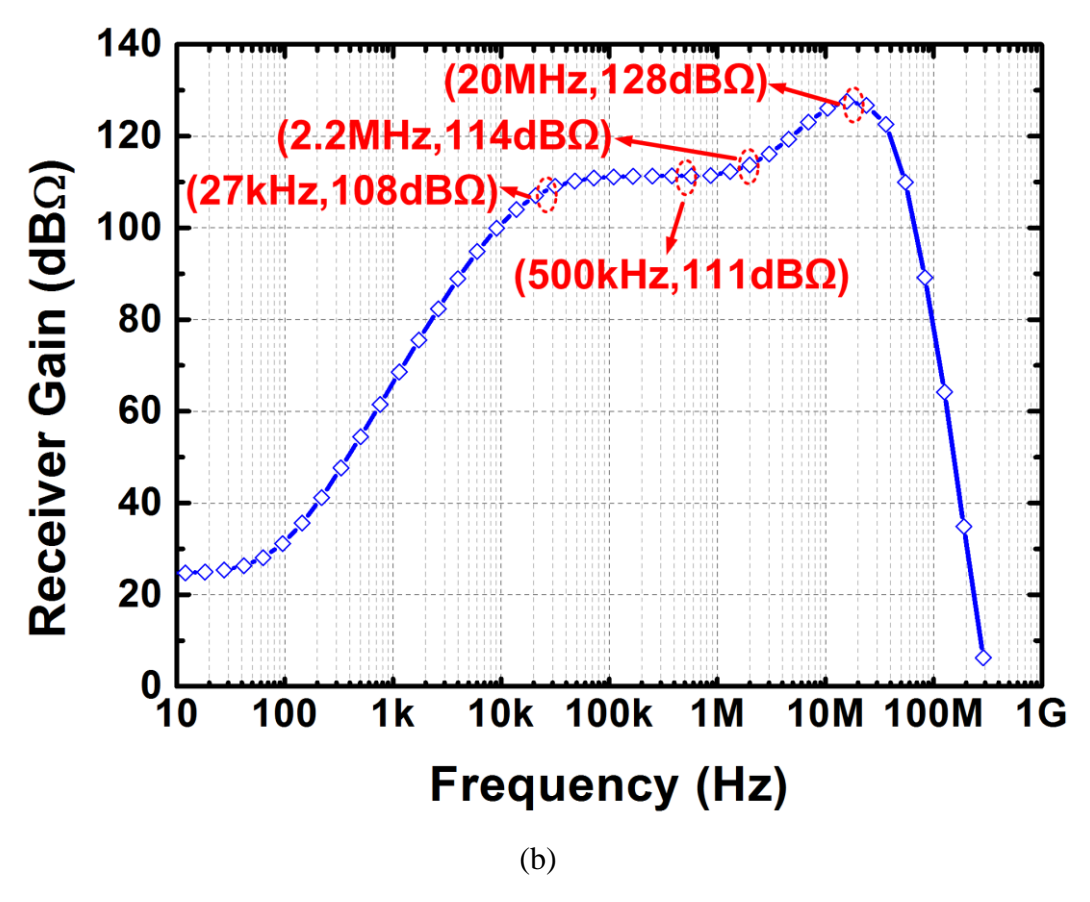


Fig. 5.21 (a) Simulated trans-impedance gain of the proposed receiver SoC when the CTLE is turned off, and the received eye diagrams using a high-speed laser diode as the transmitter front-end to replace the low-speed phosphorescent white LEDs, and (b) simulated transimpedance gain of the proposed receiver SoC when the CTLE is turned on.

The inherent bandwidth of the receiver is defined as the -3-dB bandwidth when the CTLE is turned off, which is about 20 MHz as illustrated in Fig. 5.21 (a). To verify this result, a high-speed laser diode is employed as the transmitter front-end to replace the low-speed phosphorescent white LEDs in Fig. 5.20, and the corresponding received eye diagrams captured by the proposed receiver SoC without enabling CTLE are also shown in Fig. 5.21 (a), indicating that the inherent bandwidth of the proposed receiver is sufficient to support communication data rates not larger than 40 Mb/s. The simulated trans-impedance gain frequency response of the receiver with enabled CTLE is shown in Fig. 5.21 (b). The response exhibits a lower corner frequency of 27 kHz set by the ambient light rejection unit, a zero frequency at 2.2 MHz and a peaking frequency at 20 MHz for the post-equalization purpose. Moreover, the pass-band trans-impedance gain can be adjusted from $104 \text{ dB}\Omega$ to $125 \text{ dB}\Omega$ in order to adapt to different VLC link conditions.

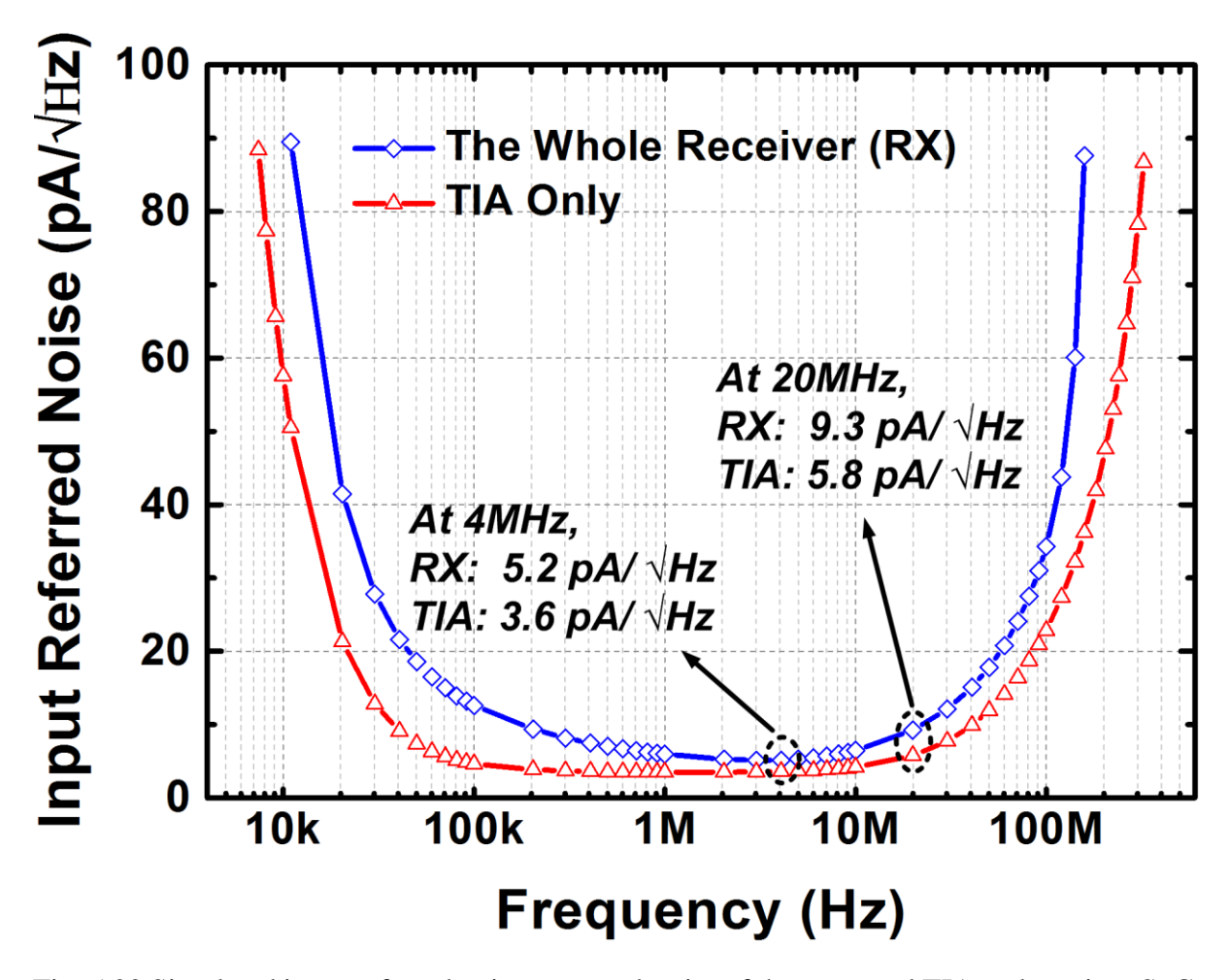


Fig. 5.22 Simulated input referred noise current density of the proposed TIA and receiver SoC.

Noise simulations in Fig. 5.22 show that with a pass-band trans-impedance gain of 111 dB Ω and a peak trans-impedance gain of 128 dB Ω , the input referred noise current density of the receiver is 5.2 pA/ \sqrt{Hz} as the minimum, and reaches 9.3 pA/ \sqrt{Hz} at 20 MHz. The integrated input referred noise current over the 20 MHz bandwidth gives about 26 nA_{rms}, meaning a 0.42 μ A_{pp} input photocurrent with a receiver trans-impedance gain of 128 dB Ω is sufficient to produce a voltage of about 1 V_{pp} at the D2S output, while achieve an SNR of 8. As for the TIA, the simulated input referred noise current density is 3.6 pA/ \sqrt{Hz} as the minimum within the 20 MHz bandwidth for a typical trans-impedance gain of 82 dB Ω , and reaches 5.2 pA/ \sqrt{Hz} at 20 MHz.

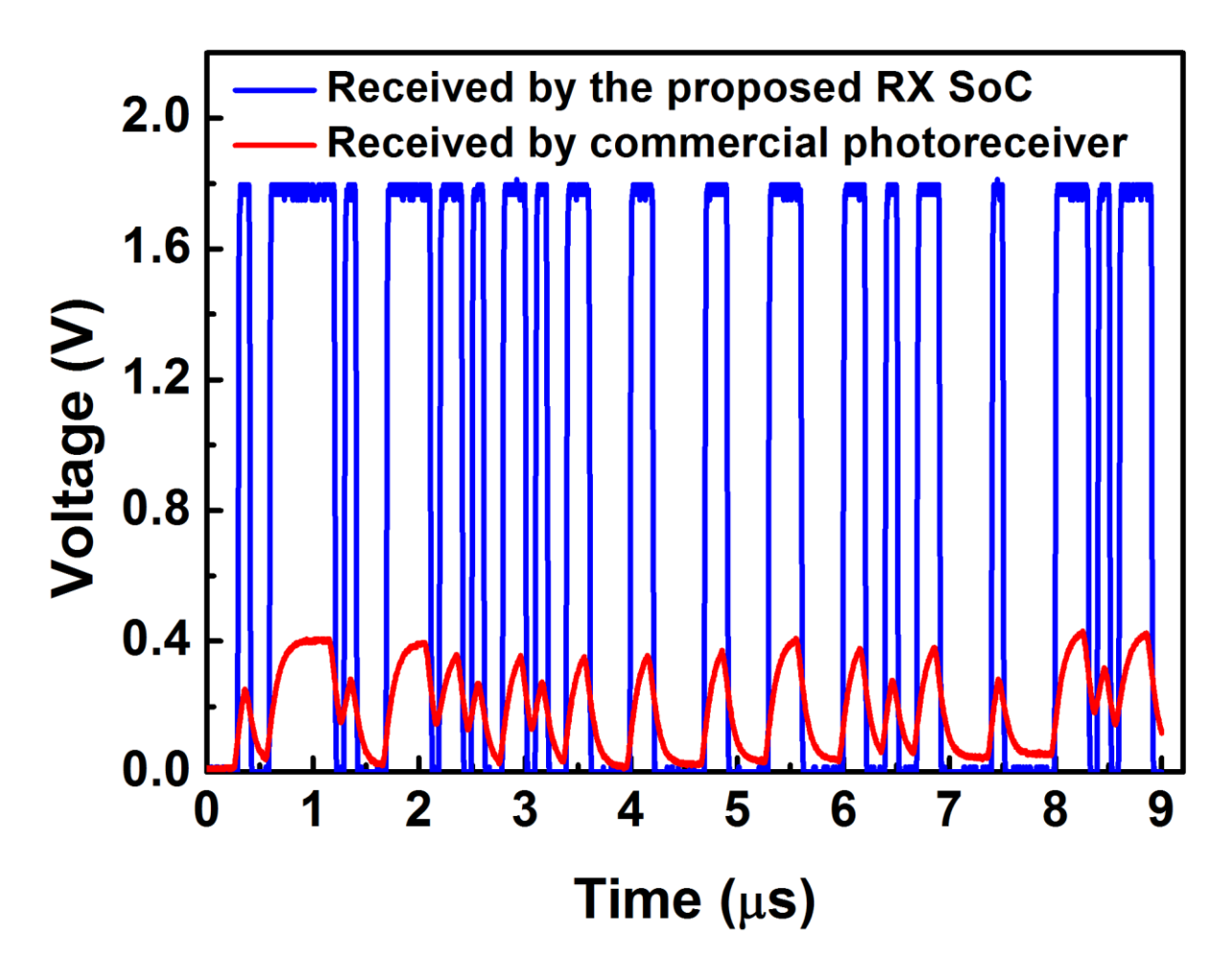


Fig. 5.23 Measured received transient waveforms using the proposed receiver SoC and the commercial photoreceiver (New Focus 1801-FC). The VLC data rate is 10 Mb/s with OOK PRBS-11 optical inputs emitted by the phosphorescent white LEDs.

Fig. 5.23 shows the comparison of measured transient waveforms received by the proposed receiver SoC and the commercial photoreceiver (New Focus 1801-FC) at a data rate of 10 Mb/s with OOK PRBS-11 optical inputs emitted by the phosphorescent white LEDs. In particular, the blue waveform is received by the receiver SoC with the CTLEs and digital output buffer, and demonstrates an output swing of 1.8 V_{pp}, while the red waveform is attained from the commercial photoreceiver (which is actually a TIA) and shows an output swing smaller than 0.5 V_{pp}. It is obvious that due to the limited bandwidth of the employed phosphorescent white LEDs on the transmitter side, the received signal from the commercial photoreceiver suffers severe distortion (or ISI). However, after being processed by the proposed receiver SoC, the distorted signal is well recovered.

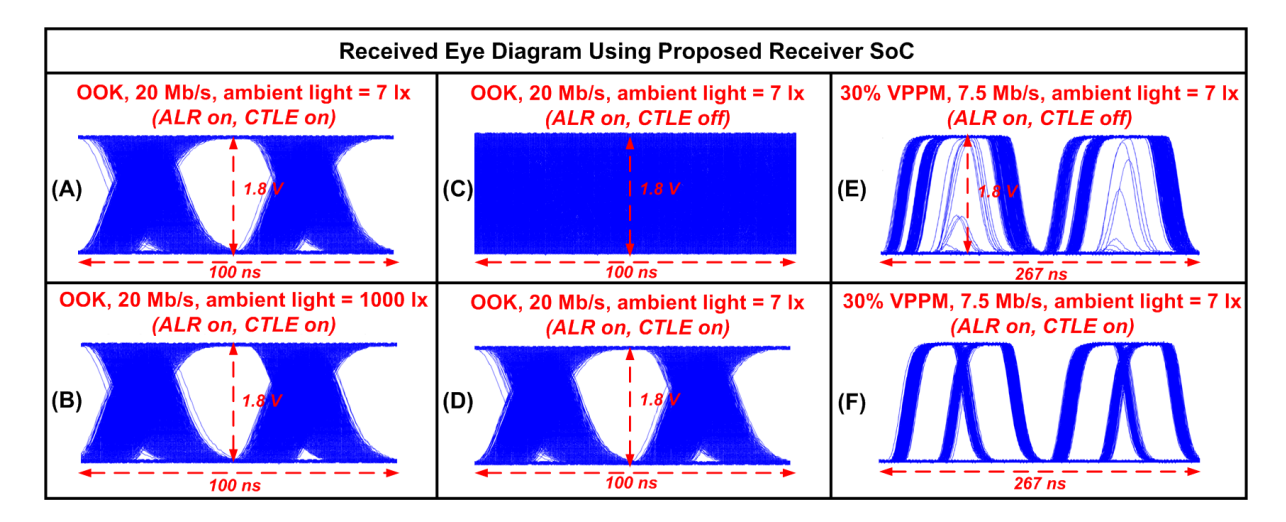


Fig. 5.24 Received eye diagrams under different conditions when using phosphorescent white LEDs as the transmitter front-end, where (A) and (B) are captured under different ambient light, while (C), (D), (E) and (F) are captured under different modulation schemes with different CTLE status. The measurements are performed at a distance of 0.25 m using optical PRBS-11 inputs without any lens.

Fig. 5.24 presents the received eye diagrams of the demonstrated VLC system (Fig. 5.20) under different conditions using phosphorescent white LEDs as the transmitter front-end. Specifically, (A) and (B) are captured under different ambient lighting levels with 20-Mb/s OOK modulation, demonstrating the ambient light rejection capability of the receiver to beyond 1000 lx, which is sufficient for general applications because the normal office lighting level is about 500 lx. The effectiveness of the proposed CTLE is also verified by employing different modulation schemes. In (C), the received eye diagram of OOK data is closed at 20 Mb/s when the CTLE is disabled. In contrast, the received data eye in (D) is significantly improved by enabling the CTLE. Similar results are shown in (E) and (F) for 7.5 Mb/s VPPM with 4B6B run-length limited (RLL) coding (according to IEEE 802.15.7 PHY-II operating mode) at 30% dimming level, where the required speed is actually 7.5 Mb/s÷30% = 22.5 Mb/s, and can only be achieved by employing the post-equalization function. All the measurements are performed at a distance of 0.25 m using optical PRBS-11 inputs without any lens.

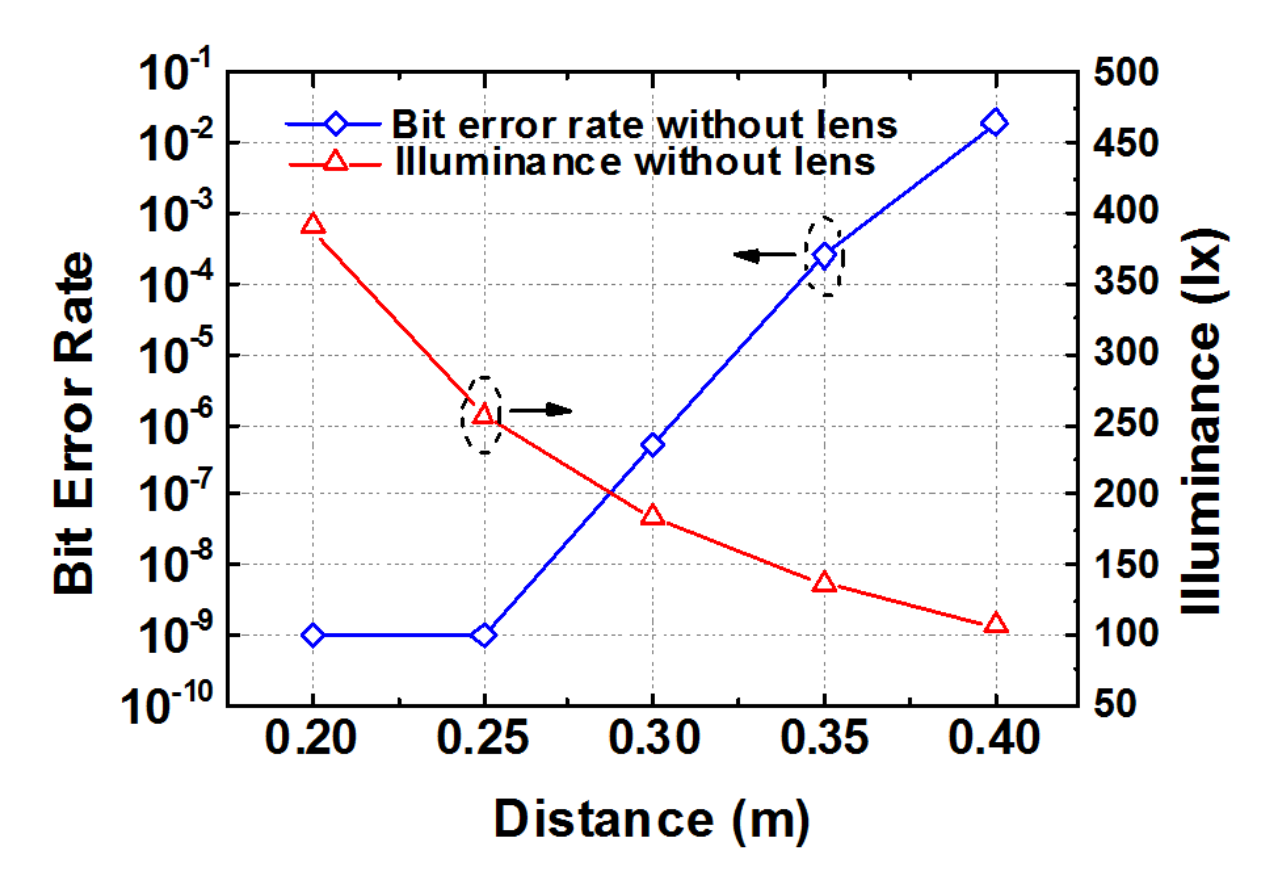


Fig. 5.25 Measured bit error rate and corresponding illumination level at different communication distances for a fixed VLC data rate of 20 Mb/s when employing OOK modulation and optical PRBS-11 inputs without any lens.

Fig. 5.25 depicts the measured bit error rate and corresponding illumination level versus communication distances for a fixed VLC data rate of 20 Mb/s when employing OOK modulation and optical PRBS-11 inputs without any lens. A BER of 10⁻⁹ is achieved at 0.25 m distance and the corresponding illuminance is 250 lx. It can also be observed that the illuminance is inversely proportional to the square of the distance and drops dramatically as the distance increases, indicating the necessity of employing optical lenses for a longer communication distance.

Fig. 5.26 shows the measured bit error rate versus VLC data rates at a distance of 0.25 m without any lens, and at a distance of 1.6 m with an RX lens. The measurements are performed using optical PRBS-11 inputs and OOK modulation. A BER of 1×10^{-9} is achieved for a maximum data rate of 20 Mb/s at a distance of 0.25 m without an optical lens. By employing an RX lens with a 5-cm diameter and 10-cm focal length in front of the receiver PD, the same

BER can be achieved up to 24 Mb/s over a distance of 1.6 m. In real applications, by utilizing a standard 8-W, 1000-lm white LED light bulb and the same RX lens in our measurement setup, the expected communication range can be significantly improved to several meters according to [87].

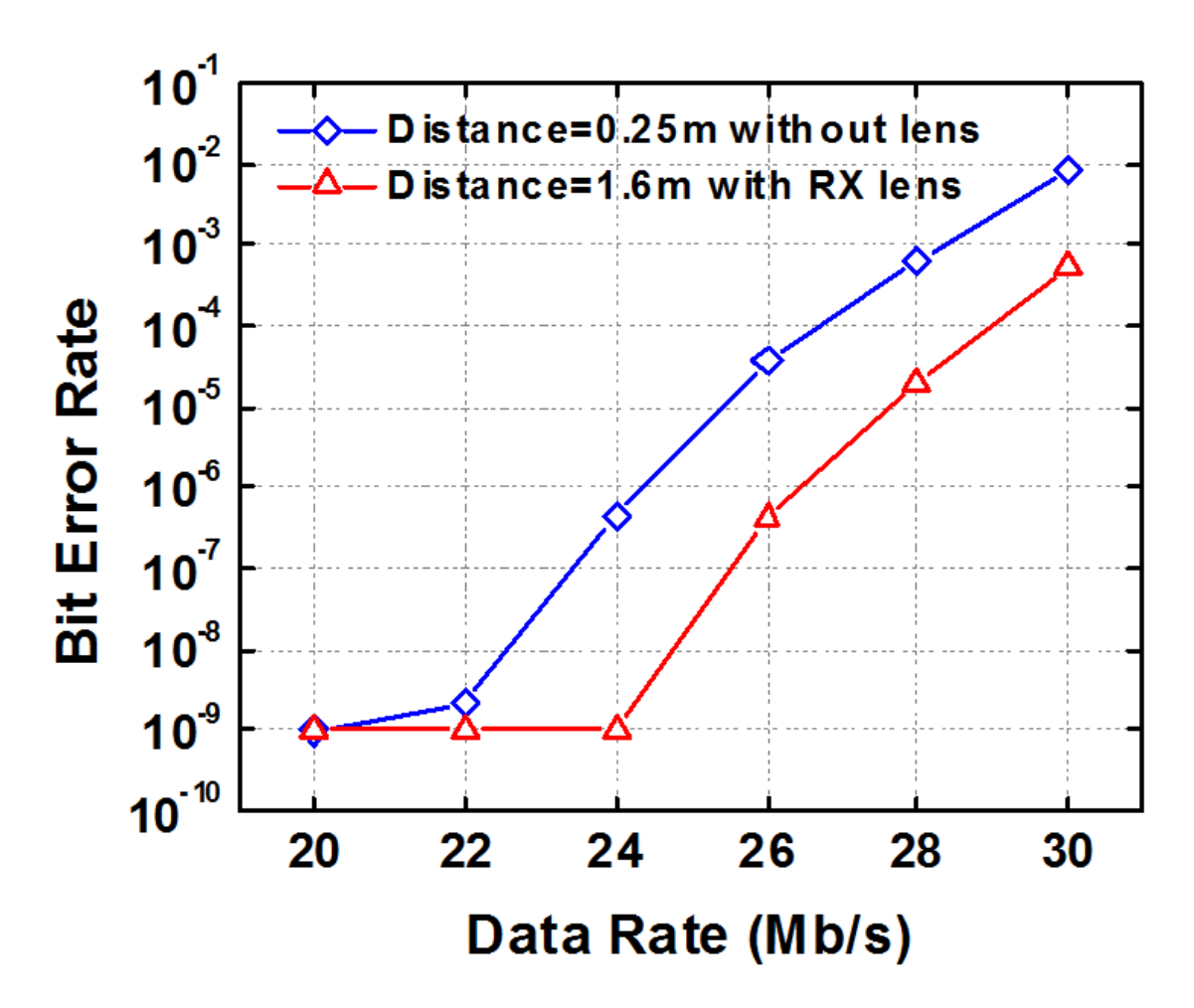


Fig. 5.26 Measured bit error rate versus VLC data rates at a distance of 0.25 m without any lens, and at a distance of 1.6 m with an RX lens. The measurements are performed using optical PRBS-11 inputs and OOK modulation.

Table 5.1 summarizes the performance of the demonstrated VLC system and some prior works. To make a fair comparison, only phosphorescent white LED based VLC systems using low-complexity OOK modulation and silicon PIN PD are involved. As shown in the table, the TX LEDs typically consume about 1 W of power to generate a total luminous flux of more than 100 lm. To improve VLC data rates, blue filtering and pre-/post-equalization techniques are employed in [94] and [28]. In contrast, only an on-chip post-equalization technique is utilized in our work for low-cost applications. On the receiver side, a bit efficiency of 92 pJ/bit is

achieved with the custom receiver SoC, which is at least 6 times better than the prior works. In addition, the receiver circuit size is more than 1000 times smaller using CMOS technology. The demonstrated system can achieve a BER of 1×10^{-9} for data rates up to 24 Mb/s over a distance of 1.6 m using only one RX lens, while the other works need an extra TX lens to maintain a reasonable communication distance, which is adverse for general illumination applications.

Table 5.1 Performance Summary and Comparison

| | | [94] | [28 | 3] | This Work | |
|-------------------------------------|--|-------------------------------------|---------------------------------|----------------------|-------------------------|--|
| BW Extension Technique ^a | | Blue Filtering + | Blue Filt | ering + | P 4 F0 | |
| | | Post-EQ | Pre-EQ + Post-EQ | | Post-EQ | |
| | LED Type | Phosphorescent White LED | | | | |
| TX | LED Power | | | | | |
| | Typical Luminous Flux | 116 lm | | | 107 lm | |
| | Using TX Lens | Yes | | | No | |
| | TX Viewing Angle | 120° | 15° | | 120° | |
| | | (limited by TX Lens) | X Lens) (limited by TX Lens) | | (limited by LED) | |
| | Modulation | OOK | | | | |
| RX | Technology | Disc | Discrete Components + PCB | | 0.18 μm CMOS | |
| | Circuit Area | N/A | 2×5 cm ² (e | stimated) | 0.7×0.4 mm ² | |
| | RX Lens Area (cm²) | 5.07 (estimated diameter = 1.27 cm) | | 20.3 | | |
| | Using Blue Filter | Yes | | No | | |
| | Ambient Light Rejection | No | N/A | | Yes | |
| | Data Rate (Mb/s) | ~320 | 550 | 480 | 24 | |
| | BER | 1×10 ⁻⁹ | 2.6×10 ⁻⁹ | 2.3×10 ⁻⁷ | 1×10 ⁻⁹ | |
| | | 0.43 | 0.60 | 1.60 | 1.60 | |
| | VLC Distance (m) | (with TX and | (with TX and | (with TX and | (with RX lens | |
| | | RX lens) | RX lens) | RX lens) | only) | |
| | Supply Voltage (V) | 10 | 3.3 | | 1.8 | |
| | Power Consumption (mW) | 360 ^b | 324 ^b | | 2.2 | |
| | | (No output stage.) | (Output stage is not included.) | | | |
| | Power Efficiency (pJ/bit) ^c | 1125 | > 589 ^d | > 675 ^d | 92 | |
| | FoM | 5 | 9 | 43 | 231 | |

^a In this item, pre-EQ and post-EQ refer to pre-equalization and post-equalization, respectively.

^b The value is attained from the datasheets of the devices used.

^c Power efficiency is defined as $\frac{RX_Power_Consumption}{Data_Rate}$.

^d This value only accounts for power consumption on the receiver (RX) side, and extra power consumption is needed for pre-equalization (pre-EQ) on the transmitter (TX) side.

A figure of merit (FoM) is proposed in this thesis to accommodate the most important parameters of a VLC system. The FoM is attained assuming the same type of light source (e.g., phosphorescent white LEDs) and modulation scheme (e.g., OOK) are employed in the transmitter, and the receiver employs a similar PD (e.g., silicon PIN PD) and contains a limiting amplifier (or digital output buffer) as the output stage. The reason for including the output stage is that in some systems only TIA is implemented with a hardware circuit while the other functions are perfromed by software, which makes a lot of difference in terms of the receiver power consumption.

In general, a higher FoM is achieved with higher data rates, a lower BER and lower receiver power consumption as they are the preferred system performance. In addition, a receiver with smaller input power to achieve the same data rate and BER demonstrates better sensitivity as well as FoM. In a VLC system, the received optical power is proportional to the total emitted optical power of the transmitter and is inversely proportional to the square of the communication distance according to the link budget analysis [87]. In particular, when a TX lens is employed to focus the emitted light beam, the transmitter viewing angle will be reduced while the received power will be increased. Therefore, for VLC systems operating at the same data rate with the same BER and total transmitter optical power, a smaller transmitter viewing angle represents higher input power required on the receiver side, resulting in lower receiver sensitivity as well as FoM. Moreover, it is undesirable to have a small transmitter viewing angle for simultaneous illumination purpose. For those systems without employing any TX lens, the transmitter viewing angle is determined by the LED itself. On the receiver side, an RX lens with a larger area can also be used to provide more incident optical power onto the PD, indicating lower receiver sensitivity and FoM when the other system performance maintains the same. By taking into consideration VLC data rate (Data_Rate), BER, communication distance, total transmitter optical power (TX Optical Power), transmitter viewing angle (TX_Viewing_Angle), receiver lens area (RX_Lens_Area) and receiver power consumption (RX_Power_Consumption), the proposed FoM can be expressed as follows, where TX and RX represent transmitter and receiver, respectively.

FoM

 $= \frac{Data_Rate[Mb/s] \times |\log(BER)|}{RX_Power_Consumption[W] \times \frac{TX_Optical_Power[lm] \times \cos(0.5 \times TX_Viewing_Angle)}{Distance^2[m^2]} \times RX_Lens_Area}$

In this FoM expression, a transmitter angle factor, which is $\cos(0.5 \times TX_Viewing_Angle)$, is employed to describe how much a light source deviates from a Lambertian emitter. For an LED that follows the Lambertian radiation pattern, the corresponding angle factor is $\cos(0.5 \times 120^{\circ}) = 0.5$. A smaller viewing angle results in a higher angle factor and poorer FoM.

Based the above equation, the related FoM is calculated for the VLC systems listed in the comparison table, demonstrating that the proposed receiver SoC has a FoM that is at least 5 times higher than the other two works for two reasons. The first reason is that the proposed receiver SoC achieves much higher power efficiency through custom circuits as well as current-reuse structures. Another reason is that the communication distance is significantly extended without using blue filtering. Although [28] can cover the same communication range by employing a TX lens, the application of this system is limited due to the narrow transmitter viewing angle of only 15 °.

CHAPTER 6 Conclusion, Future Work and Publication

6.1 Conclusion

VLC supports simultaneous illumination and communication functions, and has attracted a great deal of research interest to ease the ever-increasing radio spectrum congestion problem faced by the mobile communication industry. Moreover, VLC can be integrated with various sensors and mobile computing capabilities to enable different indoor and outdoor applications, such as smart lighting, smart display, sensing, indoor positioning, vehicle communication and underwater communication. As a futuristic technology for emerging IoT applications, VLC requires a low manufacturing cost and high energy efficiency, which have motivated the employment of advanced fabrication processes for VLC system integration. In this thesis, two VLC SoCs have been proposed and implemented, including a transmitter SoC and a receiver SoC.

- (1) The proposed transmitter SoC is the first AMLED micro-display driver with an embedded VLC transmitter. The driver integrates four identical macro-cells, each containing a pixel driver array, a row driver, a column driver and a FIFO memory, to drive a WQVGA display featuring 400×240 blue μ LED pixels fabricated on a single GaN substrate. The size of each μ LED pixel is $30\times30~\mu\text{m}^2$. At the system level, PWM superimposed with OOK modulation is proposed to accomplish grayscale control for display and simultaneously transmit VLC signals by modulating the μ LED array. At the circuit level, a pixel driver cell composed of three transistors and one capacitor (3T1C) with a novel VLC function is employed to implement the control scheme. Flip-Chip bonding is adopted to establish connections between the WQVGA micro-display and the AMLED driver SoC. Implemented in a 0.5- μ m CMOS process, the transmitter SoC enables a high-resolution micro-display module to achieve 4-bit grayscale at a 100-Hz frame rate, while supporting 1.25 Mb/s VLC for a BER <10-5 up to a distance of 25 cm without a lens. When using optical lenses, the VLC distance is extended to >500 cm.
- (2) The proposed receiver SoC is an energy-efficient VLC receiver that employs ambient light rejection and post-equalization techniques for emerging LiFi applications based on ordinary phosphorescent white LEDs. The SoC integrates a variable-gain TIA, an ambient light rejection unit, a two-stage CTLE and a DC offset cancellation amplifier. On-chip LDOs are utilized to

suppress supply noise effects on the sensitive input stages. Implemented in a standard commercial 0.18-µm CMOS process, the SoC can deliver a bit efficiency of 92 pJ/bit at a peak data rate of 24 Mb/s, which is over 6 times better than prior works. A complete IEEE 802.15.7 PHY-II standard-complaint LiFi link is demonstrated using the proposed receiver SoC and a custom transmitter SoC over a distance of 1.6 m with a BER of 1×10⁻⁹.

6.2 Future Work

Integration is significantly important for VLC to have better portability, lower cost and higher energy efficiency, and make it suitable for massive deployment and applications. Critical technologies include energy-efficient LED drivers/VLC modulators, high-sensitivity on-chip PDs for the visible light spectrum, and low-power receiver structures. In addition, to overcome the problem of insufficient LED bandwidth and achieve higher data rates, advanced modulation schemes with low complexity to support parallel data transmission are also indispensable. In particular, MIMO-VLC is promising for real high-speed applications once the interference between adjacent channels is well addressed. To enable novel applications such as simultaneous video display and VLC, not only the MIMO technique but also the advanced receiver algorithm to accommodate large dynamic input range is required. Finally, although presenting a lot of challenges, it is crucial to develop low-cost but high-speed white LEDs, which can make a huge difference to VLC as well as our life.

6.3 Published Works

- [1] **Xianbo Li**, Liang Wu, Zhaojun Liu, Babar Hussain, Wing Cheung Chong, Kei May Lau, and C. Patrick Yue, "Design and Characterization of Active Matrix LED Micro-displays with Embedded Visible Light Communication Transmitter," *IEEE/OSA Journal of Lightwave Technology*, vol. 34, no. 14, pp. 3349–3457, Jul. 2016.
- [2] Fengyu Che, Liang Wu, Babar Hussain, **Xianbo Li**, and C. Patrick Yue, "A Fully Integrated IEEE 802.15.7 Visible Light Communication Transmitter with On-Chip 8-W 85% Efficiency Boost LED Driver," *IEEE/OSA Journal of Lightwave Technology*, vol. 34, no. 10, pp. 2419–2430, May 2016.

- [3] Babar Hussain, **Xianbo Li**, Fengyu Che, C. Patrick Yue, and Liang Wu, "Visible Light Communication System Design and Link Budget Analysis," *IEEE/OSA Journal of Lightwave Technology*, vol. 33, no. 24, pp. 5201–5209, Dec. 2015.
- [4] C. Patrick Yue, Liang Wu, **Xianbo Li**, Fengyu Che, Babar Hussain, "Recent Advancements in Visible Light Communication Modulator SoCs," in *2015 IEEE Summer Topicals Meeting Series (SUM)*, pp. 49–50, Jul. 2015.
- [5] Liang Wu, **Xianbo Li**, Wing Cheung Chong, Zhaojun Liu, Fengyu Che, Babar Hussain, Kei May Lau, C Patrick Yue, "An AMLED Micro-Display Driver SoC with Built-In 1.25Mb/s VLC Transmitter," in *IEEE Symposium on VLSI Circuits*, pp. C328–C329, Jun. 2015. (*Presenter*)

6.4 Works Accepted, Submitted or Under Preparation

- [6] **Xianbo Li,** Babar Hussain, Li Wang, Junmin Jiang, and C. Patrick Yue, "A 2.2-mW 24-Mb/s CMOS LiFi Receiver System-on-a-Chip with Ambient Light Rejection and Post-Equalization," in 2017 IEEE Photonics Conference, accepted.
- [7] Liusheng Sun, **Xianbo Li**, Babar Hussain, and C. Patrick Yue, "An Adaptive Threshold Decoding Algorithm for Visible Light Communication Data Recovery from LED-Based Display Systems," in 2017 IEEE Photonics Conference, accepted.
- [8] Li Wang, Babar Hussain, **Xianbo Li**, and C. Patrick Yue, "Modulation Optimization for Visible Laser Light Communication Systems," in 2017 IEEE Photonics Conference, accepted.
- [9] Junmin Jiang, Liusheng Sun, Xu Zhang, Shing Hin Yuen, **Xianbo Li**, Wing-Hung Ki, C. Patrick Yue and Kei May Lau, "Fully-Integrated AMLED Micro Display System with a Hybrid Voltage Regulator," *2017 IEEE Asian Solid-State Circuits Conference*, submitted.
- [10] **Xianbo Li,** Babar Hussain, Li Wang, and C. Patrick Yue, "Design of a 2.2-mW 24-Mb/s CMOS VLC Receiver System-on-a-Chip with Ambient Light Rejection and Post-Equalization for LiFi Applications," *IEEE/OSA Journal of Lightwave Technology*, under preparation.

REFERENCES

- [1] IEEE Standard for Local and Metropolitan Area Networks—Part 15.7: Short-Range Wireless Optical Communication Using Visible Light, IEEE Std 802.15.7-2011, Sep. 2011.
- [2] H. Haas et al., "What is LiFi?" IEEE J. Lightw. Technol., vol. 34, no. 6, pp. 1533–1544, Mar. 2016.
- [3] A. G. Bell, W. G. Adams, Tyndall, and W. H. Preece, "Discussion on the photophone and the conversion of radiant energy into sound," *J. Soc.Telegraph Eng.*, vol. 9, no. 34, pp. 375–383, 1880.
- [4] G. Pang, T. Kwan, C.-H. Chan, and H. Liu, "LED traffic light as a communications device," in *Proc. IEEE/IEEJ/JSAI Int. Conf. Intell. Transp. Syst.*, Tokyo, Japan, 1999, pp. 788–793.
- [5] Y. Tanaka, S. Haruyama, and M. Nakagawa, "Wireless optical transmissions with white colored LED for wireless home links," in *Proc. 11th IEEE Int. Symp. PIMRC*, London, U.K., 2000, vol. 2, pp. 1325–1329.
- [6] Le Minh H, O'Brien D, Faulkner G, et al., "100-Mb/s NRZ visible light communications using a postequalized white LED," *IEEE Photonics Technology Letters*, vol. 21, no. 15, pp. 1063-1065, 2009.
- [7] Azhar A H, Tran T A, O'brien D., "A gigabit/s indoor wireless transmission using MIMO-OFDM visible-light communications," *IEEE Photonics Technol Lett*, vol. 25, no. 2, pp. 171-174, 2013.
- [8] Wang Y, Huang X, Zhang J, *et al.*, "Enhanced performance of visible light communication employing 512 QAM N-SC-FDE and DD-LMS," *Opt Express*, vol. 22, no. 13, pp. 15328-15334, 2014.
- [9] Cossu G, Khalid A M, Choudhury P, *et al.*, "3.4 Gbit/s visible optical wireless transmission based on RGB LED," *Opt Express*, , vol. 20, no. 26, pp. B501-B506, 2012.
- [10] Wu F M, Lin C T, Wei C C, et al., "3.22-Gb/s WDM visible light communication of a single RGB LED employing carrier-less amplitude and phase modulation," Conference on

- Optical Fiber Communication, collocated National Fiber Optic Engineers Conference (OFC/NFOEC), pp. 1-3, 2013.
- [11] http://www.physlink.com/education/askexperts/ae175.cfm
- [12] Mohamed Kashef, *et al.*, "Energy efficient resource allocation for mixed RF/VLC heterogeneous wireless networks," *IEEE Journal on Selected Areas in Communications*, vol. 34, no. 4, pp. 883-893, Apr. 2016.
- [13] Dushyantha A. Basnayaka, Harald Haas, "Design and analysis of a hybrid radio frequency and visible light communication system," *IEEE Transactions on Communications*, no. 99, pp. 1-1, 2017.
- [14] Xuan Li *et al.*, "Cooperative load balancing in hybrid visible light communications and WiFi," *IEEE Transactions on Communications*, vol. 63, no. 4, pp. 1319-1329, Apr. 2015.
- [15] Yunlu Wang, Harald Haas, "Dynamic load balancing with handover in hybrid Li-Fi and Wi-Fi networks," *IEEE Journal of Lightwave Technology*, vol. 33, no. 22, pp. 4671-4682, Nov. 2015.
- [16] Kevin Warmerdam, et al., "Connectivity in IoT indoor lighting systems with visible light communications," 2015 IEEE Online Conference on Green Communications (Online Green Comm), pp. 47-52, 2015.
- [17] Krishna Kadam, Manisha R. Dhage, "Visible light communication for IoT," 2016 2nd International Conference on Applied and Theoretical Computing and Communication Technology (iCATccT), pp. 275-278, 2016.
- [18] Jinyoung An, Wan-Young Chung, "A novel indoor healthcare with time hopping-based visible light communication," 2016 IEEE 3rd World Forum on Internet of Things (WF-IoT), pp. 19-23, 2016.
- [19] Sihua Shao, *et al.*, "Pixelated VLC-backscattering for self-charging indoor IoT devices," *IEEE Photonics Technology Letters*, vol. 29, no. 2, pp. 177-180, Jan. 2017.
- [20] Fengyu Che, Liang Wu, Babar Hussain, Xianbo Li, and C. Patrick Yue, "A Fully Integrated

- IEEE 802.15.7 Visible Light Communication Transmitter With On-Chip 8- W 85% Efficiency Boost LED Driver," *IEEE/OSA Journal of Lightwave Technology*, vol. 34, no. 10, pp. 2419–2430, May 2016.
- [21] S. D. Dissanayake *et al.*, "Comparison of ACO-OFDM, DCO-OFDM and ADO-OFDM in IM/DD Systems," *IEEE J. Lightw. Technol*, vol. 31, no. 7, pp. 1063–1072, Feb. 2013.
- [22] J. M. Kahn and J. R. Barry, "Wireless infrared communications," *Proc. IEEE*, vol. 85, p. 1997, 265–298.
- [23] J.Armstrongand, A. J. Lowery, "Power efficient optical OFDM," *Electron. Lett.*, vol. 42, pp. 370–372, 2006.
- [24] S. Dissanayake, K. Panta, and J. Armstrong, "A novel technique to imultaneously transmit ACO-OFDM and DCO-OFDM in IM/DD systems," in *Proc. IEEE GLOBECOM Workshops*, Houston, TX, USA, Dec. 5–9, 2011, pp. 782–786.
- [25] S. C. J. Lee, S. Randel, F. Breyer, and A. M. J. Koonen, "PAM-DMT for intensity-modulated and direct-detection optical communication systems," *IEEE Photon. Technol. Lett.*, vol. 21, no. 23, pp. 1749–1751, Dec. 2009.
- [26] Le-Minh H, O'Brien D C, Faulkner G, et al. "80 Mbit/s visible light communications using pre-equalized white LED," European Conference on Optical Communication (ECOC), pp. 1–2, 2008.
- [27] H. Li, X. Chen, B. Huang, D. Tang, and H. Chen, "High bandwidth visible light communications based on a post-equalization circuit," *IEEE Photon. Technol. Lett.*, vol. 26, no. 2, pp. 119–122, Jan. 2014.
- [28] Li Honglei, *et al.*, "A 550 Mbit/s real-time visible light communication system based on phosphorescent white light LED for practical high-speed low complexity application," *Opt Express*, vol. 22, no. 22, pp. 27203-27213, 2014.
- [29] J. Vucic, L. Fernandez, C. Kottke, K. Habel, and K.-D. Langer. "Implementation of a Real-Time DMT-Based 100 Mbit/s Visible-Light Link", in 36th European. *Conference and Exhibition on Optical Communication*, pp. 1–5, September 2010.

- [30] A. M. Khalid, G. Cossu *et al.*, "1-Gb/s Transmission Over a Phosphorescent White LED by Using Rate-Adaptive Discrete Multitone Modulation," *IEEE Photonics Journal*, vol. 4, no. 5, pp. 1465–1473, Oct. 2012.
- [31] Cossu G, et al., "5.6 Gbit/s downlink and 1.5 Gbit/s uplink optical wireless transmission at indoor distances (≥1.5 m)," European Conference on Optical Communication (ECOC), 2014.
- [32] Z. Dong, "Integrated Transceiver Design for Visible Light Communication System," Ph.D. dissertation, Elect. Eng., Univ. of California, Riverside, USA, 2014.
- [33] A. Jalajakumari, K. Cameron, R. Henderson, D. Tsonev, and H. Haas, "An energy efficient high-speed digital LED driver for visible light communications," in *Proc. IEEE Int. Conf. Commun.*, pp. 5054–5059, Jun. 2015.
- [34] S. Rajbhandari, Hyunchae Chun *et al.*, "High-Speed integrated visible light communication system: device constraints and design considerations," in *IEEE J. on Selected Areas in Communications*, vol.33, no.9, pp.1750-1757, Sept. 2015.
- [35] W. C. Chong, K. M. Lau, "Performance enhancements of flip-chip light-emitting diodes with high-density n-type point-contacts", *IEEE Electron Device Letters*, vol. 35, no. 10, pp. 1049-1051, Oct. 2014.
- [36] D. Tsonev, H. Chun, et al., "A 3-Gb/s single-LED OFDM-based wireless VLC link using a gallium nitride µLED," *IEEE Photonics Technology Lett.*, vol. 26, no. 7, pp. 637–640, Jan. 2014.
- [37] A. Neumann, J.J. Wierer, Jr., W. Davis, Y. Ohno, S.R.J. Brueck, and J.Y. Tsao, "Four-color laser white illuminant demonstrating high colour-rendering quality," *Opt. Express* vol. 19, no. S4, pp. A982–A990, 2011.
- [38] H. Chun *et al.*, "Visible Light Communication Using a Blue GaN µLED and Fluorescent Polymer Color Converter," *IEEE Photonics Technology Letters*, vol. 26, no. 20, pp. 2035-2038, Aug. 2014.
- [39] X. Li et al., "Wireless Visible Light Communications Employing Feed-Forward Pre-

- Equalization and PAM-4 Modulation," *IEEE Journal of Lightwave Technology*, vol. 34, no. 8, pp. 2049-2055, Jan. 2016.
- [40] S. Zhang, J. J.D. McKendry, *et al.*, "Directly color-tunable smart display based on a CMOS-controlled micro-LED array," *IEEE Photonics Conference*, pp. 435–436, Sep. 2012.
- [41] C. Lee *et al.*, "4 Gbps direct modulation of 450 nm GaN laser for high-speed visible light communication," *Opt. Express*, vol. 23, no. 12, pp. 16232–16237, Jun. 2015.
- [42] D. Tsonev, S. Videv, and H. Haas, "Towards a 100 Gb/s visible light wireless access network," *Opt. Express*, vol. 23, no. 2, pp. 1627–1637, 2015.
- [43] Y.-C. Chi et al., "450-nm GaN laser diode enables high-speed visible light communication with 9-Gbps QAM-OFDM," *Opt. Express*, vol. 23, no. 10, pp. 13051–13059, May 2015.
- [44] B. Fahs *et al.*, "A 12-m 2.5-Gb/s lighting compatible integrated receiver for OOK visible light communication links," *IEEE Journal of Lightwave Technology*, vol. 34, no. 16, pp. 3768-3775, Jul. 2016.
- [45] Dilukshan Karunatilaka, *etc.*, "LED based indoor visible light communications: state of the art," *IEEE Communications Surveys & Tutorials*, vol. 17, no. 3, pp. 1649–1678, Mar. 2015.
- [46] Kevin Warmerdam, *etc.*, "Visible light communications for sensing and lighting control," *IEEE Sensors Journal*, vol. 16, no. 17, pp. 6718–6726, Sep. 2016.
- [47] S. D. Perli, N. Ahmed, and D. Katabi, "PixNet: Interference-free wireless links using LCD-camera pairs," in *Proc. 16th Annu. Int. Conf. MobiCom*, pp. 137–148, 2010.
- [48] Tianxing Li, etc., "Real-time screen-camera communication behind any scene," in Proc. Proceedings of the 13th Annual International Conference on Mobile Systems, Applications, and Services (MobiSys '15), pp. 197–211, 2015.
- [49] Aleksandar Jovicic, Junyi Li, and Tom Richardson, "Visible light communication: opportunities, challenges and the path to market," in *IEEE Communications Magazine*, pp. 26–32, Dec. 2013

- [50] https://www.youtube.com/watch?v=VbG4VNA7RZs
- [51] C. Zhang, J. Tabor, J. Zhang, and X. Zhang, "Extending mobile interaction through near-field visible light sensing," in *Proc. 21st Ann. Int. Conf. MobiCom*, pp. 345–357, 2015.
- [52] T. Li, C. An, Z. Tian, A. T. Campbell, and X. Zhou, "Human sensing using visible light communication," in *Proc. 21st Annu. Int. Conf. MobiCom*, New York, USA, pp. 331–344, 2015.
- [53] Dhouha Krichen *etc.*, "The design of an optical wireless network based landing and take-off assistance system," 2016 Advances in Wireless and Optical Communications (RTUWO), pp. 59–65, 2016.
- [54] Noha Anous, etc., "A VLC-based system for optical SPR sensing facility," 2016 IEEE Wireless Communications and Networking Conference, pp. 1–6, 2016.
- [55] A. Jovicic, J. Li, and T. Richardson, "Visible light communication: opportunities, challenges and the path to market," *IEEE Commun. Mag.*, vol. 51, no. 12, pp. 26–32, Dec. 2013.
- [56] Y.-S. Kuo, P. Pannuto, K.-J. Hsiao, and P. Dutta, "Luxapose: Indoor positioning with mobile phones and visible light," in *Proc. 20th Annu. Int. Conf. MobiCom*, pp. 447–458, 2014.
- [57] Kejie Qiu, Fangyi Zhang, Ming Liu, "Let the light guide us: VLC-based localization," in *IEEE Robotics & Automation Magazine*, vol. 23, no. 4,pp. 174–183, Dec. 2016.
- [58] Yong Up Lee, Mohsen Kavehrad, "Two hybrid positioning system design techniques with lighting LEDs and ad-hoc wireless network," in *IEEE Transactions on Consumer Electronics*, vol. 58, no. 4, pp. 1176–1184, Nov. 2012.
- [59] T. Yamazato, *et al.*, "Image-sensor-based visible light communication for automotive applications," *IEEE Commun. Mag.*, vol. 52, no. 7, pp. 88–97, Jul. 2014.
- [60] I. Takai, *et al.*, "LED and CMOS image sensor based optical wireless communication system for automotive applications," *IEEE Photon. J.*, vol. 5, no. 5, Oct 2013.
- [61] S.-H. Yu, *et al.*, "Smart automotive lighting for vehicle safety," *IEEE Commun. Mag.*, vol. 51, no. 12, pp. 50–59, Dec. 2013.

- [62] Parth H. Pathak, *et al.*, "Visible light communication, networking, and sensing: a survey, potential and challenges," *IEEE Communications Surveys & Tutorials*, vol. 17, no. 4, pp. 2047–2077, Sep. 2015.
- [63] S. Arnon, "Underwater optical wireless communication network," *Opt. Eng.*, vol. 49, no. 1, Jan. 2010.
- [64] H. Kaushal and G. Kaddoum, "Underwater optical wireless communication," *IEEE Access*, vol. 4, pp. 1518–1547, 2016
- [65] N. Farr, A. Bowen, J. Ware, C. Pontbriand, M. Tivey, "An integrated, underwater optical/acoustic communications system," in *Proceedings of IEEE OCEANS*, pp. 1-6, 2010.
- [66] R. Hagem, S. O'Keefe, T. Fickenscher, and D. Thiel, "Self contained adaptable optical wireless communications system for stroke rate during swimming," *IEEE Sensors Journal*, vol. 13, no. 8, pp. 3144–3151, Aug. 2013.
- [67] Zhaojun Liu, Wing Cheung Chong, Ka Ming Wong, Kei May Lau, "GaN-based LED micro-displays for wearable applications," *Microelectronic Engineering*, vol. 148, pp. 98–103, Dec. 2015.
- [68] W. C. Chong, W. Cho, Z. J. Liu, K. M. Lau, "1700 pixels per inch (PPI) Passive-Matrix Micro-LED Display Powered by ASIC," *IEEE Compound Semiconductor IC Symposium* (CSICS), pp. 1-4, Oct. 2014.
- [69] Johannes Herrnsdorf, et al., "Active-matrix GaN micro light-emitting diode display with unprecedented brightness," *IEEE Transactions on Electron Devices*, vol. 62, no. 6, pp. 1918–1925, Jun. 2015.
- [70] Micro-display technologies for smartglasses. [Online]. Available: http://www.idtechex.com/research/articles/Micro-display-technologies-for-smartglasses-00008967.asp
- [71] Google Glass. [Online]. Available: https://en.wikipedia.org/wiki/Google_Glass

- [72] W. C. Chong, "Novel processes and device technologies for next generation light emitting diodes and micro-displays," Ph.D. dissertation, Dept. Electronic and Computer Engineering, the Hong Kong University of Science and Technology, Kowloon, HK, 2015.
- [73] OLED-DISPLAYS. [Online]. Available: https://kompendium.infotip.de/oled-displays.html
- [74] J. Y. Tsao, M. E. Coltrin, et al., "Solid-state lighting: An integrated human factors, technology, and economic perspective," in *Proc. IEEE*, vol. 98, no. 7, pp. 1162–1179, Jul. 2010.
- [75] S. M. Liu, C. F. Chen and K. C. Chou, "The design and implementation of a low-cost 360-degree color LED display system," *IEEE Trans. Consum. Electron.*, vol. 57, no. 2, pp. 289–296, Jul. 2011.
- [76] W. C. Chong, W. K. Cho, Z. J. Liu, C. H. Wang, K. M. Lau, "1700 pixels per inch (PPI) passive-matrix micro-LED display powered by ASIC," in *IEEE Compound Semiconductor Integrated Circuit Symposium*, pp. 1-4, 2014.
- [77] Z. J. Liu, W. C. Chong, et al., "360 PPI flip-chip mounted active matrix addressable light emitting diode on silicon (LEDoS) micro-displays," *J. Display Technol.*, vol. 9, no. 8, pp. 678–682, Aug. 2013.
- [78] Z. J. Liu, C. W. Cheung, et al, "A novel BLU-free full-color LED projector using LED on silicon micro-displays," *IEEE Photonics Technology Lett.*, vol. 25, no. 23, pp. 2267–2270, Dec. 2013.
- [79] N. Grossman et al., "Multi-site optical excitation using ChR2 and micro-LED array," *J. Neural Eng.*, vol. 7, no. 1, p. 016004, 2010.
- [80] A. Zarowna-Dabrowska et al., "Miniaturized optoelectronic tweezers controlled by GaN micro-pixel light emitting diode arrays," *Opt. Exp.*, vol. 19, no. 3, pp. 2720–2728, 2011.
- [81] A. Nathan, G. R. Chaji and S. J. Ashtiani, "Driving schemes for a-Si and LTPS AMOLED display," *J. Display Technol.*, vol. 1, no. 2, pp. 267-277, Dec. 2005.
- [82] C. L. Leng, L. Y. Wang and S. D. Zhang, "Two-transistor current-biased voltage-programmed AM-OLED pixel," *IEEE Electron Device Lett.*, vol. 34, no. 10, pp. 1262–1264,

Oct. 2013.

- [83] S. Ashtiani, J. Shahin, et al., "AMOLED pixel circuit with electronic compensation of luminance degradation," *J. Display Technol.*, vol. 3, no. 1, pp. 36–38, Mar. 2007.
- [84] S. Ono, K. Miwa, et al., "VT compensation circuit for AMOLED displays composed of two TFTs and one capacitor," *IEEE Trans. Electron Devices*, vol. 54, no. 3, pp. 462–467, Mar. 2007.
- [85] Z. Li, J. Waldron, et al., "Monolithic integration of light-emitting diodes and power metal-oxide-semiconductor channel high-electron-mobility transistors for light-emitting power integrated circuits in GaN on sapphire substrate," *Appl. Phys. Lett.*, vol. 102, no. 19, pp. 192107-1–192107-3, May 2013.
- [86] L. Wu, X. Li, et al., "An AMLED micro-display driver SoC with built-in 1.25Mb/s VLC transmitter," in *IEEE Symposium on VLSI Circuits*, pp. C328–C329, Jun. 2015.
- [87] Babar Hussain, Xianbo Li, Fengyu Che, C. Patrick Yue, and Liang Wu, "Visible Light Communication System Design and Link Budget Analysis," *IEEE/OSA Journal of Lightwave Technology*, vol. 33, no. 24, pp. 5201–5209, Dec. 2015.
- [88] K. Cui, et al., "Indoor optical wireless communication by ultraviolet and visible light," *Proc. SPIE*, vol. 7464, pp. 74640D-1–74640D-9, Aug. 2009.
- [89] H. Le-Minh, D. O'Brien, G. Faulkner, L. Zeng, K. Lee, D. Jung, Y. Oh, and E. T. Won, "100 Mbit/s NRZ visible light communications using a postequalized white LED," *IEEE Photon. Technol. Lett.*, vol. 21, no. 15, pp. 1063–1065, Aug. 1, 2009.
- [90] J. Vucic, C. Kottke, S. Nerreter, K. Langer, and J. W. Walewski, "513 Mbit/s visible light communications link based on DMT-modulation of a white LED," *J. Lightw. Technol.*, vol. 28, no. 24, pp. 3512–3518, Dec. 15, 2010.
- [91] K. Phang and D. Johns, "A CMOS optical preamplifier for wireless infrared communications," *IEEE Trans. Circuits Syst. II*, Analog Digit. Signal Process., vol. 46, no. 7, pp. 852–859, Jul. 1999.

- [92] Illuminance Recommended Light Levels [Online]. Available: http://www.engineeringtoolbox.com/light-level-rooms-d_708.html
- [93] Vishay Semiconductors. (2011, Nov. 22). *Silicon PIN Photodiode* [Online]. Available: http://www.vishay.com/docs/81502/bpv10.pdf
- [94] H. Li, X. Chen, B. Huang, D. Tang, and H. Chen, "High bandwidth visible light communications based on a post-equalization circuit," *IEEE Photon. Technol. Lett.*, vol. 26, no. 2, pp. 119–122, Jan. 2014.
- [95] Li Honglei, Zhang Yini, Chen Xiongbin, et al., "682 Mbit/s phosphorescent white LED visible light communications utilizing analog equalized 16QAM-OFDM modulation without blue filter," *Opt. Commun.*, vol. 354, pp. 107–111, Nov. 2015.
- [96] Hao Le Minh; O'Brien, D.; Faulkner, G.; Lubin Zeng; Kyungwoo Lee; Daekwang Jung; Yunje Oh, "High-Speed visible light communications using multiple-resonant equalization," *IEEE Photonics Technology Letters*, vol. 20, no. 14, pp. 1243-1245, Jul. 2008.
- [97] Willy M. C. Sansen, Analog Design Essentials. Netherlands: Springer, 2006.
- [98] T. C. Carusone, D. A. Johns and K. W. Martin, Analog Integrated Circuit Design. New York: Wiley, 2011.
- [99] E. Sackinger, "On the noise optimum of FET broadband transimpedance amplifiers," *IEEE Trans. Circuits Syst. I*, Reg. Papers, vol. 59, no. 12, pp. 2881–2889, Dec. 2012.
- [100] Dongmyung Lee, Jungwon Han, Gunhee Han, and Sung Min Park, "An 8.5-Gb/s fully integrated CMOS optoelectronic receiver using slope-detection adaptive equalizer," in *IEEE Journal of Solid-State Circuits*, vol. 45, no. 12, Dec. 2010.
- [101] B. Razavi, Design of integrated circuits for optical communications, McGraw-Hill, 2003.